Modeling and Simulation of Active Plasma Lenses for High Brightness Electron Beams

PhD School in Accelerator Physics

Dottorato di Ricerca in Fisica degli Acceleratori – XXXI Ciclo

Candidate

Emanuele Brentegani

Thesis Advisors

Prof. Stefano Atzeni

Dr. Enrica Chiadroni

A thesis submitted in partial fulfillment of the requirements
for the degree of Doctor of Philosophy in Accelerator Physics

September 2019

Thesis defended on 13 September 2019

Modeling and Simulation of Active Plasma Lenses for High Brightness Electron Beams
Ph.D. thesis. Sapienza – University of Rome

This thesis has been typeset by LaTeX and the Sapthesis class.

Version: September 4, 2019

Author's email: emanuele.brentegani@gmail.com

Io chiedo a una scalata non solamente le difficoltà ma una bellezza di linee
[Walter Bonatti]

Abstract

In the last few decades, considerable effort has been devoted to the research aimed at the optimization of particle accelerators. Specifically, improving the efficiency and reducing the size of the high brightness electron machines can have a dramatic technological, scientific, and economic impact. Active plasma lenses are capable of fostering this process, given their compactness, high focusing strength (up to kT/m), and symmetry. However, experimental studies have shown that they are affected by aberrations, which may severely compromise the beam quality and enlarge the minimum spot attainable. In this thesis we discuss the working principle of active plasma lenses as well as their aberrations. We built a 2-D, axially symmetric numerical model that allows to study the hydrogen-filled capillary discharges typically used for focusing electron beams. We solved the model equations with a modified version of the open source, fluid dynamics code PLUTO. Specifically, we implemented an alternating direction implicit method to evolve the parabolic part of the problem with a semi-implicit approach. We compared the results of our simulations with measurements of the electron density inside the discharge plasma. We reproduced experimental results related to active plasma lensing of a high brightness electron beam. The results of the simulations were consistent with the measurements in both cases. We also explored the effect of capillary diameter variation on the lens aberrations, the results are discussed within the thesis.

Ringraziamenti

Contents

Introduction

Nowadays, particle accelerators serve a great variety of purposes. Perhaps the use most commonly known is the fundamental research in physics, performed by the great, km-scale, colliders. However most of the accelerators in operation in the world are not devoted to basic research but rather to industrial and medical applications. Electron, proton and ion beams are routinely used in the field of material processing, cultural heritage conservation, biology and medicine (e.g. cancer treatment). Furthermore, the electromagnetic radiation obtained by bending or undulating charged particle beams (synchrotron light, usually from electrons) is an attractive tool with applications in, but not limited to, the study of structure of materials, direct irradiation and medical imaging. Special cases of synchrotron radiation facilities are the Free Electron Lasers (FELs), where electrons dynamics and radiation emission meet a resonant condition thereby providing a coherent and widely tunable source of electromagnetic radiation. With all their applications, accelerators boost the technological and scientific advances and also provide social, environmental and economical benefits.

A great limitation to the usability of these machines is their cost and size, variables that are both linked to the energy and beam quality required. Smaller and cheaper accelerators could more easily be allocated inside hospitals and industrial environments, whereas light sources could be more widespread and reach wider user communities. In addition, the high energy machines (from hundreds of GeV to TeV scale) required for the advance of fundamental particle physics have huge sizes and hardly affordable costs. For instance, the proposed International Linear Collider is between $30\,\mathrm{km}$ and $50\,\mathrm{km}$ long, and the Future Circular Collider is foreseen to be of the order of $100\,\mathrm{km}$ long.

In the last years, a considerable effort has been devoted to the research on efficiency optimization and size reduction of particle accelerators. The available accelerating gradient, that is the electric field capable of accelerating a beam, establishes the minimum length necessary for reaching the desired particle energy. The state of the art technology relies on radio frequency ($1\,\mathrm{GHz}$-$3\,\mathrm{GHz}$) cavity resonators, with traveling or standing wave design, usually made of normal conducting copper [98] or of super conducting metals (for instance niobium) [4]. In these structures, the maximum gradient achievable is limited to the breakdown limit, to few tens of $\mathrm{MV\,m^{-1}}$.

In order to push further this limit one possibility is to resort to higher frequency devices, hence reducing the geometry and tightening the fabrication tolerances. In this regard, an example is the development of $12\,\mathrm{GHz}$ (X-band) cavities for the Compact Linear Collider, that allow to obtain gradients up to $100\,\mathrm{MV\,m^{-1}}$.

Even miniature-scale copper cavities, resonating at very high frequencies are under study [22]. Another field of study is the use of RF resonating structures made of dielectrics [72], that are able to sustain higher electric fields (of the order of $GV\,m^{-1}$) with respect to what is allowed in purely metallic structures. Lastly, considerable work has been done on the use of plasmas as accelerating media, where the breakdown problem does not apply at all, being it a state of matter where the atoms/molecules are already ionized.

Regarding the usability of a beam (in terms of applications), its energy is of key importance, but its overall quality is described also by other parameters, that are important as well. Ideally, one would require that the beam particles occupy regions of the phase space as compact as possible. This requirement is strictly related to the concept of *high brightness*. Beam brightness is a figure of merit that is directly proportional to the beam current and to the beam emittance (see below). We will formally define the brightness in section 1.1.2. Regarding the transverse dynamics, a good beam should have small transverse size and small angular divergence, in addition its divergence should also grow slowly with the propagation of the beam. These last three conditions may be summarized by saying that it should have small emittance, a concept that we will formally define in section 1.1. In addition, it is desirable that the energies of its particles are close together, i.e. the *energy spread* should be small (the concept of energy spread will be also defined in section 1.1). The longitudinal length of a beam as well as the amount of total charge contained are also important aspects. Finally, the energy efficiency, the repeatability and reliability of the beam delivery process must be taken into account when designing an accelerator.

The topic discussed in this thesis is strictly involved with the problem of efficiency and miniaturization of accelerators, retaining the quality of conventionally produced beams. *Active Plasma Lenses* (APL), are of great interest especially because of the possibility of using them in combination with plasma acceleration techniques, thereby boosting the research towards novel efficient and high quality accelerators. In addition, we anticipate that APLs are compact and high performance beam focusing devices. Thus, they are very desirable in the next generation of accelerators, also independently of the use of plasma as accelerating medium. These concepts will be explained in detail below, especially in section 0.2. For completeness and clarity, before discussing such motivations we briefly outline the principles behind plasma acceleration techniques.

0.1 Basic principles of plasma acceleration

The key mechanism of plasma acceleration is the collective behavior of a plasma that happens in response to a perturbation of its initial neutrality. This perturbation may be produced by injecting one (or more) intense laser pulse(s) or charged particle beam(s) inside a plasma. Depending on the design choices and beam parameters, the plasma may be produced by the beam itself, that ionizes an initially neutral gas during the passage, or, in alternative, the plasma may be preexisting, i.e. produced by means of other strategies, for instance by triggering an electrical discharge or with a dedicated laser beam. The source of perturbation is often referred to as *driver*.
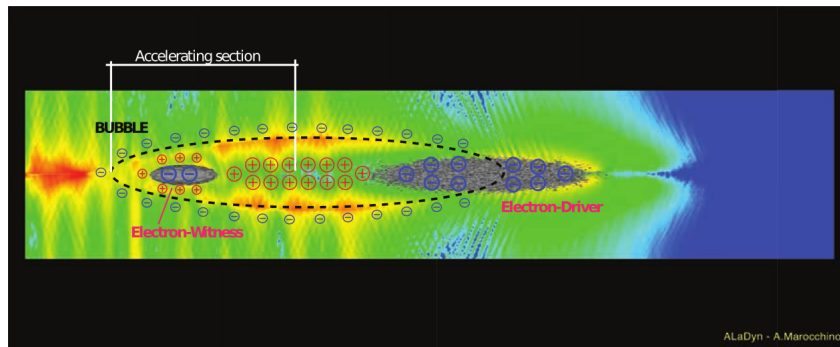
Figure 0.1. Acceleration of an electron beam exploiting the wake driven in a plasma by another electron beam. Image by A. Marocchino, simulation performed with the 3-D PIC code ALaDyn [9].

Inside its wake the plasma electrons oscillate, creating charge distributions that are approximately periodic (as a first approximation, the ions remain at their positions, being their inertia much greater than that of the electrons). Due to the presence of regions with net charge, an electric field arises, which follows the driver and is termed as *wakefield*. This field can be used to accelerate as wells as to focus a particle beam following the driver, which is called *witness*. This process is exemplified in fig. 0.1, which contains a view of a computer simulation of the acceleration of an electron witness by an electron driver inside a plasma.

A rough estimate of the longitudinal electric field sustainable by a plasma wave is given by the so called cold wave breaking limit:

$$E_{\mathrm{WB}} \approx 96\sqrt{\frac{n_0}{\mathrm{cm}^{-3}}}(\mathrm{V\,m}^{-1}), \tag{0.1}$$

which is a rough estimate of the accelerating gradient attainable (for a derivation of this expression see section 1.2.1). It is interesting to note that for realistic plasma densities, this field is much higher than what obtainable in conventional RF structures and hence it justifies the interest around the development of plasma accelerating techniques. For instance, with $n_e = 10^{16}\,\mathrm{cm}^{-3}$, we have $E_{\mathrm{WB}} \approx 10\,\mathrm{GV\,m}^{-1}$, which is orders of magnitude beyond the typical values of tens of $\mathrm{MV\,m}^{-1}$.

Since its first proposal, many schemes for exciting the wakes and providing witness particles in different manners have been proposed. We limit the discussion to outlining schemes that are targeted on electron acceleration, because beams made of other particles are not considered in this thesis.

A major distinction in electron acceleration schemes is given by the nature of the driver. When intense laser pulses are used the scheme belongs to the family of the *laser-driven*, whereas when high energy bunches of particles are employed, the scheme is of *beam-driven* type. The first plasma acceleration scheme was proposed by Tajima and Dawson and employed laser pulses as drivers [125]. In the frame of laser-driven schemes [46], we find the Laser Wake Field Acceleration (LWFA) schemes, that employ a single intense laser pulse to drive a wake, and the Plasma Beat Wave Acceleration schemes (PBWA), where the beating of two laser pulses excites a wave at the plasma frequency (for a definition of plasma frequency, see appendix A). Later,

in order to overcome some experimental difficulties, such as laser pump depletion and diffraction, which limited the possible energy gain in laser-driven schemes, the Plasma Wake Field Acceleration (PWFA) scheme was proposed[33]. In this scheme the driver is a high energy particle beam. Afterwards, a number of variants of PBWA, LWFA and PWFA have been proposed as electron acceleration schemes (see some examples in Ref. [46, 65]). Each one of them has different advantages and limitations, and its design is tailored to different energies and purposes. Another classification is provided by the way in which the witness beam is inserted in the wake of the driver: it may be injected separately into the plasma or it may be generated inside it. This last mechanism, typical of the laser-driven case, is called *internal injection* and consists in the capture and acceleration of some plasma electrons by the wakefield of the driver. The capture may happen spontaneously in highly non-linear regimes (see section 1.2.2 for an explanation of the non linear regime) or by means of more controllable mechanisms [86, 77, 94]. For instance, some internal injection designs involve the exploitation of the partial ionization of the plasma or the tapering of the plasma density channel. Instead, when the witness electrons are injected from outside the plasma, the technique is called *external injection*. External injection of electrons is a usual choice for beam-driven schemes, whereas for the laser-driven case it is considered challenging, due to the experimental difficulties in synchronizing the laser and electron beams.

Plasma acceleration as a whole is conceptually simple and the achievable peak gradients make it very appealing. Nevertheless, it is far from replacing the conventional technology, since the overall quality of the beams obtained is not satisfactory. Even though high gradients have been demonstrated [58, 49, 87], plasma acceleration is not mature enough to meet many of the common requirements that are instead easily satisfied by conventional accelerators. However, despite that, it has become an established research field, possibly capable of creating a new generation of particle accelerators.

0.2 Motivation for studying active plasma lenses

We provide here some motivations for the recently renovated interest in active plasma lensing, that is otherwise an old topic [101]. In order not to clutter this section with lots of definitions and lengthy explanations, many of the concepts here mentioned will be defined later in this thesis, especially in chapters 1 and 2.

The working principle of active plasma lensing can be summarized with the focusing/de-focusing effect provided by the Lorenz force acting on charged particles that are moving in a certain direction and sample magnetic field lines that wrap around that very direction. Such a magnetic field is created by an electrical current that flows in the same direction as the current density corresponding to the charged particles that are being focused. The focusing capabilities of APLs greatly exceed those of conventional systems, usually relying on electromagnet quadrupoles or on solenoids, and are even greater than those obtainable in permanent magnet quadrupoles (see sections 1.1.1 and 2.1 for more details). In addition, APLs are cm-scale devices and hence very compact with respect to the other available technologies.

It is clear that, for the purpose of accelerator miniaturization, APLs are very

promising. If in the next future the accelerating sections will be shrank down to few centimeters or few meters, also the length of the beam transport lines will need to be shortened. It would be unpleasant to have long lines devoted to the manipulation of the beam in order to meet the strict requirements for the injection into (or the extraction from) a short plasma acceleration module. When delivering a beam to a plasma, small transverse spots are required in order to meet the so called *matching* condition. If the size is greater than what required for matching (we will derive this condition in section 1.2.2), the beam envelope will oscillate with consequent emission of synchrotron radiation, in this case called betatron radiation, and possible emittance degradation. Matching the beam to the plasma also provides a minimization of its divergence at the exit from the plasma stage and a reduction of the dependence of the divergence angle on the plasma parameters [68, pp. 130-133, 173-178]. The strong focusing capabilities provided by APLs can be useful to meet these constraints. Furthermore, as we said before, the quality of plasma accelerated beams is usually poor. When a beam exits a plasma stage it is often highly divergent (mrad-scale) and it has non negligible energy spread (percent level). In such conditions the normalized emittance (which is a generalization of the emittance concept and is defined in chapter 1) will grow significantly (as shown in section 1.1.2) if is is not captured shortly afterwards with a suitable focusing system. APLs can be extremely useful in this regard.

All the mentioned properties make APLs also useful for staging of plasma acceleration modules, a possibility that has been already demonstrated [121], but that encounters some potential limitations when applied to very intense beams [81].

Last but not least, we mention the possibility of using APLs as final focus devices [111] and for emittance measurements [91].

0.3   State of the art

The first reported use of an APL is by Panofsky and Baker, in 1950 [101]. Fifteen years later, an APL was used by Forsyth et al., for focusing kaons and pions [56]. Later, in the eighties and nineties, the application of APLs to ion beams were studied, especially for the possibility of using them as final focusing systems for developing a heavy-ion, inertially-confined fusion reactor [36]. As we said before, the recent interest in APLs is mostly related to the development of plasma wakefield acceleration techniques; hence, it is concentrated on the focusing of high brightness electron beams, by means of unpinched discharges in capillaries with length of the order of centimeters and radius in the millimeter/sub-millimeter range [130, 121, 108, 106, 113, 82]. For example, a discharge inside one of the capillaries used at SPARC_LAB is shown in fig. 0.2.

The main issue that one needs to overcome for effective and efficient active plasma lensing of high brightness electron beams is the presence of aberrations. These aberrations can be generated by the transverse profile of the magnetic field that often does not fit the design requirements and also by the presence of undesired plasma wakes excited inside the discharge plasma. In addition, one should also take into account the problem of beam scattering with plasma ions and neutrals, that may arise when heavy gas species are used (for instance argon). However, this aspect
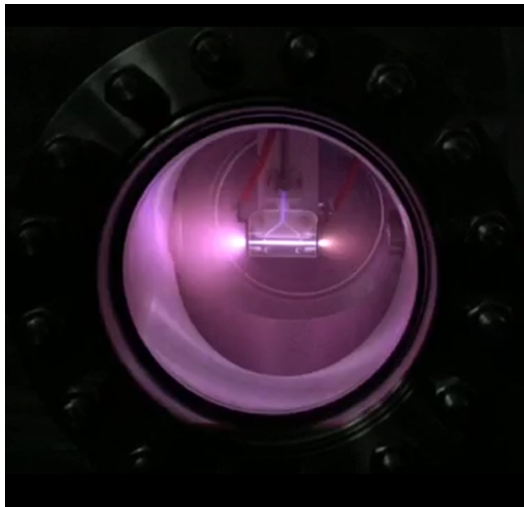
Figure 0.2.   Electrical discharge inside a 3 cm long, hydrogen filled capillary at
         SPARC_LAB. Picture from Ref.[53]

is of minor importance for light elements, such as hydrogen or helium. More details
on APL issues and experimental progresses, are provided in chapter 2.

Regarding the modeling, a number of numerical studies on capillary discharges is
present in literature. Modeling of capillary discharges was fostered by the possibility
of developing and improving laser-related technologies [43, 18]; including, for instance,
the possibility of channeling a laser inside the electron density generated by means of
a discharge, thereby guiding it for distances over the diffraction Rayleight range. Also,
an appealing field of study is the optimization of the plasma generation processes,
to obtain a medium best suitable for LWA and PWA applications. Most part of
the theory and numerical modeling that has been developed models the plasma as
a compressible fluid in a 1-D axially symmetric geometry, where all the quantities
depend on the radial position inside the capillary but not on the longitudinal or on
the azimuthal one [19, 47, 26, 25]. This approximation is justified by considering
the typical length to radius ratio of these capillaries, $L/R \approx 10 \div 100$. In those
works, the reactions occurring in the plasma are either modeled assuming a local
thermodynamic equilibrium (LTE), which is often applied separately for electrons and
ions [19] or by taking a more accurate and computationally more expensive nonLTE
approach [26]. In addition, it can happen in these discharges that a transverse
thermal equilibrium is quickly reached, the skin effect is negligible and the Ampere's
self forces are small with respect to the thermal pressure gradients. This allows for
computing the relevant plasma quantities by means of a semi analytical quasi-static
model[19], where the plasma is in thermal equilibrium and evolves adiabatically with
the time variation of the electrical current. We will describe this model in more
detail in section 2.2.1.

Furthermore, 2-D studies considering the transverse section of (ideally) very
long capillaries have been performed. The effect of the transverse capillary shapes
(squared[1] and circular) has been theoretically investigated, for both laser guiding

---

[1]Squared capillaries allow greater diagnostic accessibility

and electron beam focusing [5]. Oblong rectangular shapes were also theoretically studied and proposed for production of electron beams with flat transverse profile [7].

A 3-D magneto hydrodynamic model was used to study a discharge in a capillary with the aim of providing more accurate theoretical insight on its laser guiding properties in relation to LWA [6]. The effect of the initial mass density distribution was taken into account by simulating also the filling process (with a hydrodynamic model including thermal conduction). The outflow of the hot gas from the open extremities, and hence the spreading of electron density outside the discharge region, was considered in the evaluation of the coupling properties between laser beams and the plasma.

Regarding APLs, a 2-D axially symmetric model is the minimum complexity that is required to accurately study the time development of the focusing magnetic field, taking also into account the outflow of matter from the capillary extremities. The outflow of plasma is important not only because of it is responsible for a modulation of the plasma properties along the capillary, but also because it may generate electron density ramps just outside the capillary. A beam passing through these ramps may excite wakes, sometimes with detrimental effects on its quality [90]. In addition, even though the capillaries employed have a high L/R ratio, their shape is intrinsically 2-D (at least); the same applies to the electrodes employed. The effect of the 2-D geometry on the development of the discharge needs to be carefully studied, with a special care on the magnetic field produced.

To our knowledge, except for Ref. [23], no other numerical study on capillary discharges with focus on their active plasma lensing properties and employing at least a 2-D, axially symmetric geometry is present in literature[2]. With our studies we aim at addressing these needs, in order to provide further insights on the physical system, useful for designing effective and efficient APLs in the next future.

0.4 Organization of this thesis

After the present introductory discussion, this thesis is organized as follows:

- In chapter 1 general concepts of accelerator physics will be defined, together with some fundamental topics in electron beam-plasma interaction that will be useful in the discussions coming afterwards;

- In chapter 2 the working principle of the active plasma lenses will be explained, and their main issues will be discussed. In particular we will present the aberrations coming from the non uniform distribution of the current density inside the plasma channel. We will outline the problem of the scattering between beam electrons and plasma ions and heavy particles. We will also discuss on the aberrations coming from the undesired wakes excited in the plasma. Lastly, the recent experimental results on the focusing of high brightness electron beams will be summarized following the presently available literature;

- In chapter 3 the experimental system for gas discharge available at SPARC_LAB – the location were this thesis work was performed, will be described, together

---

[2]Note that in Ref. [6] no magnetic field profile was plotted, being it of little importance for laser coupling optical properties.

with the measurement systems implemented. Also, the whole SPARC_LAB facility, will be briefly introduced;

- In chapter 4 we will explain how a discharge plasma may be modeled in generic terms, and we will provide an idea of the derivation of the mathematical model used in the present work for simulation of capillary discharges;

- In chapter 5 we will describe the equations used to model the capillary discharges that we studied in this thesis, including some important details on the transport parameters and the ionization model employed. Then the numerical method and the code that we chose to practically solve the system equations will be explained;

- In chapter 6 we will provide the results of the discharge simulations that we performed. We will also discuss the outcomes outlining what we learned from the simulations, in terms of reliability of our model and for the possibility of optimization of APLs for high brightness electron beams.

We will then conclude by summarizing the main results and with some final remarks. In the appendix we add the derivation of the main plasma parameters.

Chapter 1

Accelerators and plasmas

1.1 Transverse beam dynamics fundamentals

Beams of interest in accelerator physics are composed by particles always confined in regions of small transverse size, approximately centered on the longitudinal axis of propagation. In general, particles belonging to a real beam have a spread in their direction and transverse position. Considering that externally driven forces can only affect the average motion of the particles, being practically unfeasible to act on any singular particle independently on the others, it is clearly not possible to focus a beam down to a null size spot.

In this thesis we study beams with the transverse components of momentum that is much smaller than the longitudinal one:

$$p_x, p_y \ll p_z \approx p. \tag{1.1}$$

From now on we indicate the transverse coordinates with x,y (or r when employing cylindrical coordinates with axial symmetry) and the longitudinal one with z, unless otherwise noted. Following the assumption above, it is convenient to refer to the angle of divergence of a particle with respect to the longitudinal axis with the so called *paraxial* or *small angle* approximation:

$$x' = \frac{p_x}{p_z} \approx \frac{p_x}{p}, \qquad y' = \frac{p_y}{p_z} \approx \frac{p_y}{p}, \tag{1.2}$$

where the apex indicates the derivative along the z coordinate.

It is possible to define a statistical quantity, called *root mean square emittance*, that is a figure of merit of the beam and takes into account the degree of disorder of the beam due to non uniformity of particle positions and angles of motion:

$$\epsilon_x \doteq \sqrt{\langle x^2 \rangle \langle x'^2 \rangle - \langle xx' \rangle^2}, \tag{1.3}$$

where the $\langle \alpha \rangle$ notation indicates the arithmetic mean of quantity α over all the particles. Note that, if the beam is on axis ($\langle x \rangle = 0$) the terms appearing in the emittance definition represent the variance of the transverse positions of the particles, $\langle x^2 \rangle$, the variance of the transverse directions, $\langle x'^2 \rangle$, and the covariance of the two, $\langle xx' \rangle$, which takes into account the degree of correlation of particle positions and

directions. Obviously, the definition of emittance for the y coordinate may be obtained by substituting x with y in eq. (1.3). We study now only the physics in the (x, z) plane, but the discussion may be adapted to the (y, z) in a straight forward manner.

In accelerator physics, the quantity $\sigma_x \doteq \sqrt{\langle x^2 \rangle}$ is called beam envelope and represents a possible formalization of the concept of transverse beam size. Computing its second derivative with respect to z and rearranging the terms it is possible to derive a second order non linear differential equation, describing its longitudinal evolution in a convenient way:

$$\sigma_x'' - \frac{\langle xx'' \rangle}{\sigma_x} = \frac{\epsilon_x^2}{\sigma_x^3} \tag{1.4}$$

It is clear that the term on the right hand side, that contains the beam emittance, may be physically interpreted as an outward pressure on the beam envelope. The term $\langle xx'' \rangle$ contains the second derivatives of the particle positions, which are proportional to the forces acting in the transverse direction, and involves the dependence of these forces on x.

For instance, when the beam drifts freely, without the effect of any force on its particles, i.e. $\langle xx'' \rangle = 0$, the emittance is constant and the equation reduces to

$$\sigma'' \sigma_x^3 = \epsilon_x^2, \tag{1.5}$$

with solutions:

$$\sigma_x(z) = \sqrt{[\sigma_x(z_0) + \sigma_x'(z_0)(z - z_0)]^2 + \frac{\epsilon_x}{\sigma_x(z_0)^2}(z - z_0)^2}. \tag{1.6}$$

If we set as z_0 the location where the beam has the minimum envelope (the so called beam waist) and we call σ_0 the value of the minimum, we may rewrite the solution as:

$$\sigma(z) = \sigma_0 \sqrt{1 + \frac{\epsilon^2}{\sigma_0^4}(z - z_0)^2}. \tag{1.7}$$

We see that the rate of growth the beam envelope from the waist depends on the emittance (it grows of a factor $\sqrt{2}$ after a characteristic length of σ_0^2/ϵ.

It is clear that having small emittance beams is important in order to keep the beam divergence and size under control. This is one of the main reasons why it is most often preferred to have an emittance that is as small as possible.

1.1.1   Conventional beam focusing

If a transverse force acts on the beam and is such that:

$$x'' + kx = 0, \tag{1.8}$$

with k being a real constant, than the particles oscillate around the $x = 0$ position. The parameter k is termed as *focusing strength*. It is easy to verify that in this case the emittance is constant by computing its derivative from the definition 1.3 and substituting x'' with $-kx$. Conditions eq. (1.8) is very desirable in accelerator

physics, since it allows to focus the beam, or confine it inside a channel, without spoiling the emittance. In reality, condition1.8 is never met, not only because of the dependence of k on x,y and z, but also because k may variate from particle to particle, depending, for instance, on their energy.

The product of the focusing strength with the longitudinal extension, L, of the region where eq. (1.8) is valid is usually indicated with K (capital letter).

If the transverse positions of the particles do not change significantly during the passage through the lens, we are in the so called *thin lens* approximation; a necessary condition for this is that L be much shorter than $1/\sqrt{k}$. In this case the lens provides the particles with a transverse kick $\Delta x' = -Kx$ and focuses an incoming bunch of particles, each with zero divergence, down to a point that is downstream the lens location by a distance $f = 1/(kL)$. The parameter f is called focal length.

In the remaining part of this section we discuss on two examples of beam optical systems: the magnetic quadrupoles and the solenoids. These are of great importance in high brightness linacs, but are not the only focusing systems used in accelerator physics. For instance, other common devices are the electrostatic lenses, that exploit static electric fields for low energy particle focusing, and the radio frequency quadrupoles that exploit a RF electromagnetic field to accelerate and focus at the same time (usually employed for low energy ion beams). For further information see Ref. [70].

Focusing with quadrupoles

We take as example the use of magnetic quadrupoles for beam focusing. These devices are made by four equidistant and alternated magnetic poles appropriately placed around the beam axis. The generated magnetic field is such that, watched on the (x, y) plane, it is null at the position $x = 0$, it grows linearly with x and is orientated as $\pm y$. Depending on its sign it contributes to focus or defocus the beam, thanks to Lorentz force. For an ultra-relativistic beam ($\beta \approx 1$), in the paraxial approximation, we have that in a quadrupole:

$$k = \frac{qg}{m_0 c\gamma},\tag{1.9}$$

being m_0 the rest mass of the particles, q their charge, c the speed of light, γ the relativistic γ factor and g the gradient along x of the magnetic field component in y direction, $g = B_y/x$. We note that, since $k \propto 1/\gamma$, the more energetic the beam is, the weaker the quadrupole k. Moreover, if the particles have different energies, i.e. different γ, they experience different restoring forces, thereby breaking the uniformity of the focusing strength.

It is important to mention that such a quadrupole field is only focusing in one direction, and necessarily de-focusing in the other one. In order to have a resulting global focusing of the beam in both transverse planes, one has to arrange some quadrupoles (at least two, but to attain some satisfying degree of flexibility three are very often required), with alternated orientations and accordingly tuned field gradients.

Quadrupole fields may be produced by means of electromagnets or by permanent magnets. The first ones are more easily tunable than the second ones, since the

gradient g may be variated by changing their feeding current, whereas the second ones require nontrivial movements of the poles. Instead, when dimensions are a constraint, permanent magnets are explorable solutions for obtaining high field gradients (up to $600\,\mathrm{T\,m^{-1}}$ [79, 107]) in small spaces.

Focusing with solenoids

Another solution for beam focusing is the use of the magnetic field generated by means of current loops wrapped around the beam axis. These loops form a solenoid, with a radially symmetric magnetic field that is mainly oriented in longitudinal direction. Outside the device the magnetic field has an important component in transverse direction, r. The associated focusing strength is:

$$k = \left(\frac{qB_0}{2\gamma m_0 c} \right)^2, \tag{1.10}$$

where B_0 is the magnetic field inside the solenoid. The working principle of a solenoid is that the beam particles, while entering the device, sample the fringing field, whose radial component is responsible for a Lorentz force generating a rotational motion of the particles in the transverse plane. Then, inside the solenoid, due to their the just acquired velocity component, the interaction with the longitudinal magnetic field creates a force pointing towards the longitudinal axis. When exiting, they experience another fringing field which, that generates a velocity component that compensates the one acquired initially. Note that solenoids are focusing regardless of the sign of the current flowing in the loops. Furthermore, they focus in both planes at the same time. A drawback of these devices is that their focusing strength scales like $1/\gamma^2$, and are therefore usually preferred at low energies, reserving focusing of high energy particles to quadrupoles.

1.1.2 Emittance variations and non linearities

Normalized emittance

When particles are accelerated, their longitudinal momentum increases. This means that the emittance decreases, since the ratios of the x and y components of the momentum (which do not variate due to pure acceleration) to the longitudinal one decrease. For this reason, it is convenient to define a so called *normalized emittance*, which does not variate under uniform acceleration of the beam:

$$\epsilon_{\mathrm{N}x} \doteq \frac{1}{m_0 c} \sqrt{\langle x^2 \rangle \langle p_x^2 \rangle - \langle x p_x \rangle^2} = \sqrt{\langle x^2 \rangle \langle (\beta\gamma x')^2 \rangle - \langle x\beta\gamma x' \rangle^2} \tag{1.11}$$

In this definition, p_x takes the role formerly played by x'. When the beam has negligible relative energy spread, that is defined as

$$\sigma_\gamma \doteq \sqrt{\frac{\langle \beta^2\gamma^2 \rangle - \langle \beta\gamma \rangle^2}{\langle \beta\gamma \rangle^2}}, \tag{1.12}$$

the rms normalized and non normalized emittances are connected by the simple relation $\epsilon_{\mathrm{n}x} = \langle \beta\gamma \rangle \epsilon_x$. A parameter related to the normalized emittance is the beam

brightness, a figure of merit of great importance for many applications, including the production of FEL radiation (the higher the brightness, the more valuable the beam). Its definition is:

$$B = \frac{2I}{\epsilon_{\mathrm{N},x}\epsilon_{\mathrm{N},y}}, \tag{1.13}$$

where I is the beam current. Note that the brightness is inversely proportional to the beam (normalized) emittance. This is one of the main reasons why low emittance beams are highly desirable.

Sources of emittance growth

We note however, that a non uniform acceleration of the beam is capable of producing emittance growth, besides generating energy spread as obvious. Intuitively this may be explained by noting that energy non uniformity represents a kind of disorder in the beam, and therefore a source of emittance. It is easy to verify this fact for a beam with no correlation between transverse positions and energy and in ultra-relativistic conditions. In fact, after a bit of algebra the following relation can be obtained [68, p.165]:

$$\epsilon_{\mathrm{n},x} = \left\langle \gamma^2 \right\rangle (\sigma_\gamma^2 \sigma_x^2 \left\langle x' \right\rangle^2 + \epsilon_x^2). \tag{1.14}$$

In addition, the relation shows that for large energy spread beams, even an increase of the spot size or beam divergence generates emittance growth.

As anticipated before, when a beam with large energy spread passes through magnetic beam optics (such as quadrupoles or solenoids, but also APLs) it may undergo emittance growth due to the different focusing forces experienced by particles, depending on their γ. Moreover, also the non uniformity of the magnetic field gradient inside a quadrupole can be a source of emittance degradation.

Another example is the space charge forces due to the repulsive Coulomb interaction of beam particles, that have a linear and a non linear component. Nevertheless, when a beam reaches high energies, depending on its current and size, it arrives to a condition where the space charge forces are negligible. This happens because the Lorentz force acting on the beam particles depends also on the magnetic field generated by the beam itself. The magnetic component of the Lorentz force is attractive and, for high γ, tends to compensate the repulsive electric component. In fact, in cylindrical symmetry we have:

$$F_r = e(E_r - \beta c B_\theta) = e(1 - \beta^2)E_r = e\frac{E_r}{\gamma^2}, \tag{1.15}$$

where F_r is the Lorenz force acting on a beam electron, B_θ is the azimuthal component of the magnetic field, E_r is the radial component of the electric field. Note that we also used the relation $B_\theta = \frac{\beta}{c}E_r$, that gives the magnetic field of a distribution of charge that translates rigidly (with velocity βc) in longitudinal direction. It is clear that the space charge defocussing effect drops like $1/\gamma^2$. With respect to the beam parameters, it happens that the space charge may be neglected approximately when the beam γ exceeds the threshold:

$$\gamma_{\mathrm{tr}} = \frac{I\sigma^2}{2I_{\mathrm{A}}\epsilon_n^2}, \tag{1.16}$$

where $I_A = 4\pi\epsilon_0 m_0 c^3/e$ is called Alfvén current and is approximately $17\,\text{kA}$ for electrons. Further explanation may be found in Ref. [68, pp 168-170]

Aberrations

An optical system is said to have *aberration* when it is not capable of focusing a zero emittance beam down to a single point focus. The term *spherical aberration* is also often used for the analogy with the problems encountered when lenses for optical light are made out pieces of spherical surfaces. An aberrated lens offers a focusing strength that is not uniform, either in the transverse direction (*transverse aberrations*), or in the longitudinal direction (*longitudinal aberrations*). The aberration is said to be *chromatic* when particle with different energies experience different forces.

In order to minimize the attainable spot and the emittance growth, it is often preferable to have aberration free optics. In general, however, there are situations where some degree of aberration is desired, as its effect on the beam quality depends on the degree of correlation between particle energies, positions and transverse momenta (see below).

To explain the possibility of emittance increase we consider a thin lens providing a restoring force on the beam particles proportional to the third power of the particle positions,

$$x'' + ax^3 = 0. \tag{1.17}$$

This corresponds to a focusing strength directly proportional to the square of the particle positions, $k = ax^2$. The lens length is L and it provides the particles with a kick $\Delta x' = -aLx^3$ and leaves their positions unchanged. By computing the square of the rms emittance of the beam after the lens and subtracting the expression of the emittance before entering the lens, one obtains the following expression, giving the variation of the squared emittance:

$$\Delta(\epsilon^2) = -2aL \left\langle x^2 \right\rangle \left\langle x^3 x' \right\rangle + (aL)^2 \left\langle x^2 \right\rangle \left\langle x^6 \right\rangle + 2aL \left\langle xx' \right\rangle \left\langle x^4 \right\rangle - (aL)^2 \left\langle x^4 \right\rangle^2. \tag{1.18}$$

In the case of an initially laminar beam, with particles propagating perfectly parallel to the longitudinal axis (which implies zero initial emittance), the first and third term on the right hand side are zero and we are left with:

$$\Delta(\epsilon^2)\Big|_{x'=0} = (aL)^2 \left\langle x^2 \right\rangle \left\langle x^6 \right\rangle - (aL)^2 \left\langle x^4 \right\rangle^2 > 0. \tag{1.19}$$

It is not difficult to prove that this quantity is always positive, providing an emittance increase, from zero to a certain positive value. Instead, if we consider a real beam at waist, the third term of eq. (1.18) vanishes, since $\langle xx' \rangle = 0$, and the expression becomes:

$$\Delta(\epsilon^2)\Big|_{\langle xx' \rangle = 0} = -2aL \left\langle x^2 \right\rangle \left\langle x^3 x' \right\rangle + (aL)^2 \left\langle x^2 \right\rangle \left\langle x^6 \right\rangle - (aL)^2 \left\langle x^4 \right\rangle^2. \tag{1.20}$$

As before, the last two terms provide a positive contribution, but the sign of the first one is not known a priori. The overall result depends on the kind of correlation of the particle angles with their positions, and in principle it is even possible that the emittance will decrease.

1.2 Beams in plasmas

Since the topic of this thesis is on the use of current carrying plasmas to focus electron beams, we cover here briefly also the theory of the interaction of electron beams with plasmas. In fact, it is not possible to study the effect of active lensing without considering the presence of free electrons and ions in the region of the space transversed by the beam. Depending on their densities, different kind of wakes (with their associated electromagnetic wake fields) may be excited in the plasma. Since we do not cover the topic of the combination of beam focusing and acceleration in the same plasma, but we rather discuss only-focusing stages, we will limit the discussion to the aspects that are useful for studying the effect on the plasma wakes on the beam focusing and the related undesired effects, such as emittance increase.

In addition, the contribution of beam electrons scattering with the plasma ions have to be considered.

In section 1.2.1, we present the main features of the linear regime, that applies when the electron plasma density is much greater than the beam density and the plasma electron move at speed much smaller than the speed of light. In section 1.2.2 we briefly discuss the non-linear regime, that applies when the plasma density is comparable or smaller than that of the beam. Lastly, in section 1.2.3 we will give some consideration on the importance of the scattering between beam electrons and plasma ions.

1.2.1 Linear plasma wakefield regime

When an electron beam enters a plasma that is much denser than the beam itself, its electric field causes a movement of the plasma electrons, while the ions are almost immobile, due to their much greater mass. Intuitively, we can imagine that the plasma electrons initially move trying to shield the beam space charge and eventually they will start oscillating.

We follow the derivation of the linear regime pedagogically rewritten by Blumenfeld [17]. We begin by considering the continuity equation for plasma electron fluid:

$$\frac{\partial n_e}{\partial t} + \boldsymbol{\nabla} \cdot n_e \mathbf{v}_e = 0, \tag{1.21}$$

and the Lorentz force acting on an electron:

$$\frac{\partial \mathbf{p}_e}{\partial t} = -e(\mathbf{E} + \mathbf{v}_e \times \mathbf{B}). \tag{1.22}$$

In this last equation, the electric and magnetic fields are the superposition of the ones provided by the plasma and by the beam electrons. The magnetic field generated by the passage of a cylindrically symmetric ultra-relativistic beam has a magnitude that is of the order of the ratio between the transverse component of the electric field and the speed of light, $\|\mathbf{B}_b\| \approx \|\mathbf{E}_{\perp,b}/c\|$. If the plasma electrons move at a speed that is much smaller than the speed of light, the contribution of the $\mathbf{v}_e \times \mathbf{B}_b$ term in eq. (1.22) is negligible with respect to the one due to the electric field. In addition, the magnetic field generated by the plasma electrons is even smaller than

that of the beam. Hence, we can drop the $\mathbf{v}_e \times \mathbf{B}$ term and we obtain:

$$m_e \frac{\partial \mathbf{v}_e}{\partial t} = -e\mathbf{E}. \tag{1.23}$$

Then, we linearize eq. (1.21) by considering the electron density as a result of the superposition of a constant value, n_0, with a very small perturbation term, δn:

$$n_e = \delta n + n_0, \quad |\delta n| \ll n_0, \tag{1.24}$$

Using again the assumption of small speed and neglecting second order terms we get:

$$\frac{\partial \delta n}{\partial t} + n_0 \boldsymbol{\nabla} \cdot \mathbf{v}_e = 0. \tag{1.25}$$

Taking the time derivative of this equation and using eq. (1.23) to substitute for $\frac{\partial \mathbf{v}_e}{\partial t}$, we arrive at:

$$\frac{\partial^2 \delta n}{\partial t^2} - \frac{n_0 e}{m} \boldsymbol{\nabla} \cdot \mathbf{E} = 0, \tag{1.26}$$

where we can substitute the electric field with its expression obtained from Gauss' Law, particularized by remembering that, due to the local charge neutrality of plasma, the ion charge density, ρ_i, shields the unperturbed electron charge density, and including the contribution of the electron beam density n_b:

$$\boldsymbol{\nabla} \cdot E = \frac{\rho_\mathrm{i} - en_\mathrm{e} - en_\mathrm{b}}{\epsilon_0} = -\frac{e\delta n + en_\mathrm{b}}{\epsilon_0}. \tag{1.27}$$

Thus we obtain:

$$\frac{\partial^2 \delta n}{\partial t^2} + \frac{e^2 n_0}{\epsilon_0 m_\mathrm{e}} \delta n = -\frac{e^2 n_0}{\epsilon_0 m_\mathrm{e}} n_\mathrm{b}, \tag{1.28}$$

that we can rewrite using the definition of plasma wavenumber, $k_p = \sqrt{\frac{e^2 n_0}{\epsilon_0 m_\mathrm{e} c^2}}$ (for the definition of plasma wavenumber see appendix A), and switching to the co-moving frame by setting $\xi \doteq z - ct$:

$$\frac{\partial^2 \delta n}{\partial \xi^2} + k_p^2 \delta n = -k_p^2 n_\mathrm{b}, \tag{1.29}$$

This is the equation of a driven harmonic oscillator. It shows that the plasma responds to the perturbation due to an electron beam by generating charge density waves. Its solution may be found using Green's functions. In the special case where the electron beam density is separable and the beam is longitudinally limited to $\xi < 0$, i.e.

$$n_b = n_{b,0} f(r) g(\xi), \qquad\qquad \xi < 0 \tag{1.30}$$
$$n_b = 0, \qquad\qquad\qquad\qquad \xi \geq 0$$

it takes the simple form:

$$\delta n = n_{b,0} f(r) G(\xi), \tag{1.31}$$

with $G(\xi)$ defined by:

$$G(\xi) \doteq k_p \int_\xi^0 g(\xi') \sin[k_p(\xi' - \xi)] \, \mathrm{d}\xi'. \tag{1.32}$$

Expressions for 2-D wakefields

The wake field is defined as the Lorentz force acting on a unit charge that moves at the same speed as the beam. It can be split in longitudinal wake,

$$\mathbf{W}_{\parallel}(r, \xi) = \mathbf{E}_z \tag{1.33}$$

that involves only the longitudinal electric field, and transverse wake,

$$\mathbf{W}_{\perp}(r, \xi) = (\mathbf{E} + c\boldsymbol{\beta} \times \mathbf{B})\Big|_r \approx \mathbf{E}_r - c\mathbf{B}_\theta \tag{1.34}$$

that has also a magnetic field component.

One can derive expressions for the wake fields starting from the electromagnetic wave equation, plugging in the source terms and applying the same assumptions of small plasma perturbation and slow plasma electron motion as in section 1.2.1. For the special case where the electron beam density is separable and longitudinally limited to $\xi < 0$, and thus the plasma perturbation δn is as in eq. (1.31), the wake fields have the following expressions [32]:

$$W_{\parallel} = -\frac{en_{b,0}}{\epsilon_0 k_p^2} \frac{\partial G}{\partial \xi} F(r) \tag{1.35}$$

$$W_{\perp} = -\frac{en_{b,0}}{\epsilon_0 k_p^2} G(\xi) \frac{\partial F}{\partial r} \tag{1.36}$$

with $F(r)$ defined by:

$$F(r) \doteq k_p^2 K_0(k_p r) \int_0^r r' f(r') I_0(k_p r') \, \mathrm{d}r' \tag{1.37}$$

$$+ k_p^2 I_0(k_p r) \int_r^\infty r' f(r') K_0(k_p r') \, \mathrm{d}r' \,,$$

where I_0 is the 0-th order modified Bessel function of first kind and K_0 is the 0-th order modified Bessel function of second kind.

Equation (1.35) and eq. (1.36) allow to calculate the kick experienced by the beam particles due to the plasma response to its passage.

Maximum longitudinal field

A rough estimate of the maximum longitudinal electric field that may be produced in the linear case may be performed by assuming a plasma density perturbation equal to the initial value. This is just meant to set a maximum limit that cannot be exceeded from inside the linear theory, and the procedure itself is obviously not strictly correct. In fact, in the linear theory we assumed that the perturbations are small with respect to the unperturbed situation.

If all the plasma electrons are expelled by the beam passage and they oscillate coherently with a typical frequency ω_p, they will generate an oscillating electric field,

$$\mathbf{E} \approx \mathbf{E}_0 e^{-ik_p z}. \tag{1.38}$$

Computing the divergence of this field one obtains,

$$\|\boldsymbol{\nabla} \cdot \mathbf{E}\| \approx \|-ik_p\mathbf{E}_0\| = \frac{\omega_p}{c}E_0 \tag{1.39}$$

Applying Gauss law considering the full evacuation of plasma electrons we have

$$\frac{\omega_p}{c}E_0 \approx \frac{en_0}{\epsilon_0}, \tag{1.40}$$

that may be rearranged as:

$$E_0 \approx \frac{m_e c}{e}\omega_p \doteq E_{\mathrm{WB}}, \tag{1.41}$$

This expression, already introduced in section 0.1, is the *wave-breaking* field and, as said above, represents the maximum field sustainable by a plasma in the linear regime. It depends only on the plasma density; its expression is often provided in the engineering form:

$$E_{\mathrm{WB}} \approx 96\sqrt{\frac{n_0}{\mathrm{cm}^{-3}}}(\mathrm{V\,m}^{-1}). \tag{1.42}$$

As already explained in section 0.1, with realistic plasma densities the values obtained from eq. (1.42) can greatly exceed those attainable in conventional radio-frequency accelerating structures. This is one of the main reasons that motivates the research towards plasma wakefield acceleration.

1.2.2   Nonlinear plasma wakefield regime

When the beam density is comparable to the plasma electron density, the plasma response becomes non linear. Approximately all the plasma electrons are expelled from the beam passage region due to the repulsive electric field of the beam. The passage of the beam is not anymore a small perturbation to the plasma, whose electrons may also move at relativistic speeds. At first order, the result is a bubble co-moving with the beam, depleted of electrons and containing only the ions, which are too heavy to move significantly during the beam passage time. Due to the possible relativistic effects, the wave breaking field (see eq. (1.42)) may be exceeded.

A model for the nonlinear dynamics of electrons in this regime, that allows to compute the shape of the bubble and accelerating field was developed by Lu [84, 85], and recently another theory has been provided by Stupakov [123]. We do not enter the details of any of the these theories here, since it is not necessary for the purpose of this work.

In addition, we note that for more accurate results, numerical simulations exploiting more rigorous and complete models have to be used. Typically, particle-in-cell (PIC) codes are employed, that model the beam and the plasma by using macro-particles and compute their electromagnetic fields by weighting and distributing their charges densities on a computational grid; the PIC method provides a great boost in computational costs with respect to straight forward particle-particle algorithms that take into account the interaction of each particle with every other separately [12]. For instance, some PIC codes used in accelerator physics are ALaDyn [9], PIConGPU [28] and Smilei [38]. Also hybrid PIC-fluid methods are used, that model the beam with a kinetic approach and treat the plasma as a cold fluid, providing a reduction in computational time with respect to a fully kinetic algorithm. Among the codes implementing these methods, we find the program Architect [88].

Transverse electric field and envelope oscillations

In the approximation of a uniform and infinitely long, axially symmetric ion column, the transverse electric field experienced by the beam particles may be easily computed with Gauss Law. It is dependent on the ion density and on the distance from the axis:

$$E_r = \frac{e}{2\epsilon_0} n_p r, \tag{1.43}$$

and the associated focusing strength is:

$$k = \frac{e^2}{2\epsilon_0 m_e c^2} \frac{n_p}{\gamma}. \tag{1.44}$$

In this approximation the focusing strength is uniform. Therefore it is expected that in this case, i.e. when the plasma is much less dens than the beam, the aberrations are much smaller with respect to the opposite case in which the ratio of the two densities is inverted. This is at the base of the concept of underdense plasma lens [124].

The nonlinear plasma regime is of great importance when intense beams are concerned, such that the background electron density (much smaller than that of the beam, as we said) is still high enough to produce significant focusing/accelerating fields. This is a commonly encountered situation in plasma acceleration modules. In those cases, the beam envelope will naturally tend to oscillate in the focusing field of the ions, unless the beam meets the so called *matching* condition. We derive this condition here since the possibility of reaching it with the help of an APLs is one of the motivations behind this technology.

To study the envelope evolution, we refer to eq. (1.4). In order to express the term $\langle xx'' \rangle$ as a function of k, we note that k and x fulfill eq. (1.8), from which it follows that:

$$\langle xx'' \rangle = -\left\langle kx^2 \right\rangle = -k\sigma_x^2, \tag{1.45}$$

where we used the fact that k is uniform and may be brought outside from the expectation symbol. Hence, the envelope equation becomes

$$\sigma_x'' + \sigma_x k = \frac{\epsilon_x^2}{\sigma_x^3}, \tag{1.46}$$

that is the equation of a harmonic oscillator with an additional source term on the right hand side. When the size of the beam is large, the term $\sigma_x k$ prevails over the term $\frac{\epsilon_x^2}{\sigma_x^3}$ and thus we have $\sigma'' < 0$. The beam size will therefore decrease, until the emittance term becomes dominant, implying $\sigma'' > 0$. The beam envelope will then grow, but the term $\sigma_x k$ will eventually prevail again, forcing once more a decrease in size. This is the mechanism of the beam envelope oscillation (note that the envelope will remain positive in any case). There exists an ideal condition, where the beam does not oscillate, and it is found by setting $\sigma_x'' = 0$ in eq. (1.46). It follows that the envelope will be constant (of course every single particle will oscillate anyway) if its rms size is:

$$\sigma_x = \sqrt{\frac{\epsilon_x c}{e}} \sqrt[4]{\frac{2\gamma\epsilon_0 m_e}{n_p}} \tag{1.47}$$
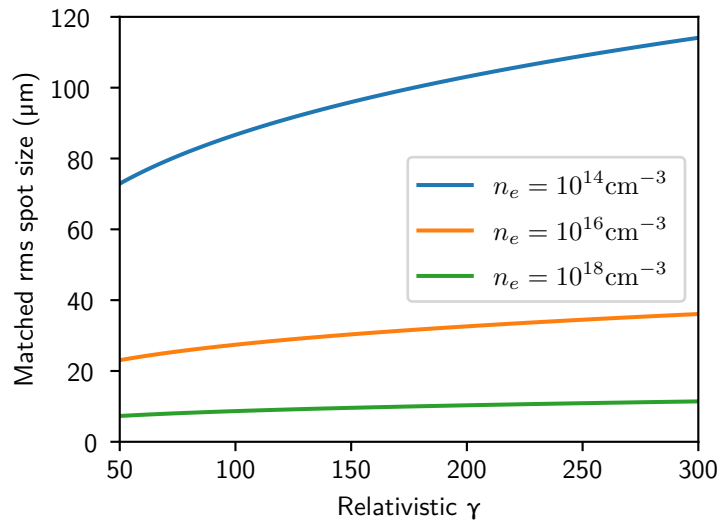
Figure 1.1. Matched rms spot size value for some typical electron densities employed in plasma acceleration studies

If this situation occurs one says that the beam is matched to the plasma. In fig. 1.1, we plotted the value of the matched rms spot size against the relativistic γ of the beam and for some typical plasma densities in plasma wakefield acceleration. For further details see also Ref. [68, pp. 130-133, 173-178].

1.2.3 Multiple Coulomb scattering

In a particle accelerator the beam is usually kept under conditions of high vacuum and this prevent it from important (elastic or inelastic) interactions with gas particles[1]. For linear accelerator purposes, the effect of inelastic collisions is usually negligible. Obviously, in a focusing or accelerating device based on plasma, this vacuum condition cannot be fulfilled, and one should also take into account the possibility of having beam-neutral or beam-ion scattering.

In a neutral gas, elastic scattering occurs when the impact parameter of a particle is comparable to (or smaller than) the atomic radius. Instead, the scattering with charged ions occurs also beyond the atomic radius, due to their electric charge. The largest impact parameter to be considered is the distance above which the ion field is shielded. For a quasi neutral plasma, this distance is the Debye length (for its definition see appendix A), above which ions are screened by the charge of free electrons. Instead, for the positively charged bubble generated by a beam in the nonlinear blowout regime, this length is the radius of the ion column, which is of the same order as the plasma skin depth, k_p (see appendix A for the definition of plasma skin depth).

The problem of beam-gas scattering has been extensively studied [16, 10, 66, 112], and it has been also generalized to scattering with ions [73, 95]. For the rate of

---

[1]Besides this, there are other reasons why beams are kept under high quality vacuum, for instance the safe operation of the radio frequency devices.

normalized emittance growth of an ultra-relativistic electron beam we take the expression derived by Kirby [73, eq. 22]:

$$\epsilon'_{x,n} = 2\pi r_e^2 \frac{n_0 \sigma_x^2}{\gamma \epsilon_x} \left[Z_i^2 \ln \left(\frac{\lambda}{R_a} \right) + 1.78 Z(Z+1) \ln \left(\frac{287}{\sqrt{Z}} \right) \right]. \qquad (1.48)$$

Here, n_0 is the neutral vapor density, Z_i the ion ionization degree, λ is either the Debye length or the or the plasma skin depth, Z is the atomic number of the gas species, r_e is the classical electron radius and $R_a \approx 1 \times 10^{-10}$ m is the atomic radius. The left addend in the parenthesis on the right hand side takes into account the long range interaction of the beam electrons with the plasma ions, instead the right addend is due to the close range interaction with the heavy particles, either ionized or not. For fully ionized hydrogen ($Z = 1, Z_i = 1$), in the fully blowout regime ($\lambda = k_p$) the two terms are approximately the same size, but for increasing Z, the term due to neutral vapor becomes dominant [73] (assuming singly ionized ions). In the case where the beam perturbs the plasma only slightly and no bubble is generated (linear regime) the plasma deviation from local neutrality can be neglected and the Debye length should be used as larger impact parameter in eq. (1.48), $\lambda = \lambda_{\text{Deb}}$. The Debye length is approximately 3 orders of magnitude shorter than the plasma skin depth, for temperatures of few eV; nevertheless since it appears inside a logarithm, the rate of emittance increase does not change significantly with respect to the fully blowout situation. When multiple Coulomb scattering with ions is an issue, one possibility to reduce it is using a plasma made of a low Z element.

Chapter 2

Active plasma lensing

Plasmas may be used in different manners to focus (or defocus) a particle beam. The kind and quality of the focusing provided may be related to different physical effects and, depending on the underlying principles, beams with different properties can be delivered after a plasma lens. The focusing strength may be provided by an electrical current flowing in the plasma, as well as, by the wake due to the passage of the beam in the plasma itself. When the focusing is provided by the wake, the term *passive plasma lens* is used [124]. Instead, when the focusing is provided by the magnetic field generated by an externally driven current, the term *active plasma lens* (APL) is used.

In section 2.1 we explain the basic physical principle of an APL and we will talk about its capabilities, whereas in section 2.2 we will discuss the related problems and drawbacks that have to be taken into account for its design and operation. Lastly, in section 2.3 the recent results on the application of APLs to electron beams will be summarized.

2.1 Working principle and main features

In an APL an azimuthal magnetic field is generated by a current flowing through a plasma channel in the same direction as the beam current. The magnetic field lines lay on the transverse plane and wrap around the axis of the capillary, thus producing a focusing Lorentz force on a charged particle beam passing coaxially through the discharge. In Fig. 2.1 a scheme of principle of an APL is presented.
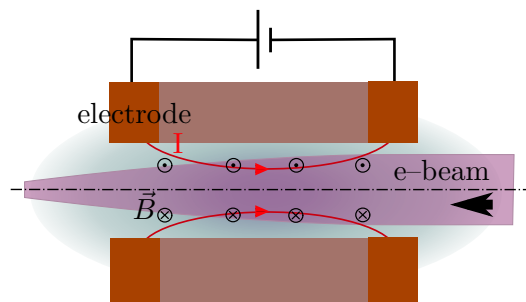
Figure 2.1. Schematic view of an active plasma lens.

To derive the expression for the focusing strength we start from the Lorentz force acting on a beam electron,

$$\frac{\mathrm{d}\mathbf{p}_e}{\mathrm{d}t} = -e\mathbf{v} \times \mathbf{B}. \tag{2.1}$$

Watching only at the radial component of the momentum and considering that the magnetic field has only an azimuthal component the previous equation becomes:

$$\frac{\mathrm{d}p_{e,r}}{\mathrm{d}t} = -ev_z B_\phi. \tag{2.2}$$

Writing explicitly the electron transverse momentum and longitudinal velocity,

$$\frac{\mathrm{d}}{\mathrm{d}t}(\gamma m_e c \beta_r) = -e\beta_z c B_\phi, \tag{2.3}$$

substituting the time derivative for the longitudinal one, according to $\frac{\mathrm{d}}{\mathrm{d}t}(\gamma\beta_r) = c(\gamma\beta_r)''$, and using the paraxaial approximation ($\beta_r \ll \beta_z \approx 1$) one obtains:

$$\gamma r'' = -\frac{e}{m_e c} B_\phi. \tag{2.4}$$

Now, defining the focusing gradient, $g \doteq B_\phi/r$ as for quadrupoles[1], we arrive at the equation for the transverse electron positions,

$$r'' + \frac{eg}{m_e c\gamma} r = 0. \tag{2.5}$$

To derive the focusing strength of the lens, one has to compute (see section 1.1.1)

$$k_{\mathrm{APL}} \doteq \frac{x''}{x}. \tag{2.6}$$

Considering $x = r\cos\phi$, and plugging together the last two equations, we have:

$$k_{\mathrm{APL}} = \frac{eg}{m_e c\gamma} = \frac{e}{m_e c\gamma}\frac{B_\phi(r)}{r} = \frac{e}{m_e c\gamma}\frac{B_\phi(\sqrt{x^2 + y^2})}{\sqrt{x^2 + y^2}}. \tag{2.7}$$

It is useful to rewrite this expression as a function of the current flowing in the plasma. The magnetic field is given by Ampere's law, and when the current density is uniform on the transverse plane its expression is

$$B_\phi = \frac{\mu_0}{2\pi}\frac{Ir}{R^2}, \tag{2.8}$$

where I is the electrical current and R is the radius of the (capillary) discharge. We may therefore rewrite the k_{APL} parameter as:

$$k_{\mathrm{APL}} = \frac{\mu_0}{2\pi}\frac{e}{m_e c}\frac{I}{\gamma R^2}. \tag{2.9}$$

In the following of this thesis, we assume rotational symmetry around the beam propagation axis. This is a realistic approximation, when the geometry of the

---

[1]For $r = 0$, g is defined by the derivative $\frac{\partial B_\Phi}{\partial r}\big|_{r=0}$.

capillary containing the discharge is also rotationally symmetric and no effects capable of breaking this condition occur (such as, for instance, instabilities of the discharge that may occur at high currents). This assumption is acceptable in a number of recent literature cases [106, 108, 130, 131, 82], even though in some cases indications of asymmetries have been noticed and are probably related to the presence of gas inlets in the capillary [108][2]. In addition, studies where the transverse planes have different focusing gradients with different situations are also present [7, 5]

In the most recent applications (see section 2.3), APLs are implemented by discharges contained in capillaries of few cm length and radius in the mm order. They can be made of sapphire (sometimes with printed plastic holders) or directly of printed plastic. See for instance Ref. [54], where capillaries made of VeroClear-RGD810 material have been studied.

In addition, applications where the discharge plasma self-pinches under the effect of the Lorentz force generated between its own current density and magnetic field existed [21]. This is a well known phenomenon called *z-pinch* that eventually leads to instabilities in the discharge column. Regarding the use of APL for high brightness electron beam focusing, this effect has not been explored in detail: all the studies consider situations with marginal or negligible pinches.

APLs can focus simultaneously in both transverse planes, as it is clear from eqs. (2.1) to (2.7), and their focusing strength scales like $1/\gamma$. As a comparison, we note that the focusing strength of the solenoids, which also provide transversely symmetric focusing, scales like $1/\gamma^2$. This makes solenoids not suitable for application at high energies, while APLs are as applicable as quadrupoles are, since also the focusing strength of quadrupoles scales like $1/\gamma$.

Table 2.1. Focusing gradient $(\mathrm{T\,m}^{-1})$ of an active plasma lens with uniform current density for various currents and radii.

		R (m)		
		100	200	500
	100	2000	500	80
I (A)	500	10000	2500	400
	1000	20000	5000	800

In table 2.1 some examples of focusing gradients attainable with an APL are presented. It is possible to reach values up to $\mathrm{kT\,m}^{-1}$, even higher than those attainable with permanent magnet quadrupoles that in recent applications attain gradients of the order of $600\,\mathrm{T\,m}^{-1}$ [79, 107]. Therefore the lens length required for attaining satisfying beam confinement and transport is smaller than what required for quadrupoles, that also need to be placed in doublets (or triplets) for focusing in both transverse planes. In recent experimental studies, lens of few centimeters have been used [106, 108, 130, 82]

---

[2]See for instance the difference in emittance growth between the horizontal (12 %) and vertical (80 %) planes in Ref. [108]

2.2   APL issues

The above described features, make APLs very appealing. However, some issues and criticalities need to be overcome for stable and optimal focusing of high quality particle beams. In the following we will discuss the main sources of aberrations that affect active plasma lenses: the possibility that the azimuthal magnetic field has a non linear dependence on the radial position inside the lens (section 2.2.1), the excitation of undesired wakes when a beam passes inside the lens (section 2.2.2) and the possibility of beam scattering with plasma ions and neutrals (section 2.2.3).

2.2.1   Non linearity of the magnetic field

In a capillary discharge, the establishment of a transverse thermal equilibrium acts against the formation of a magnetic field profile with a linear dependence on the radial coordinate. In fact, the capillary wall remains relatively cold during a discharge, providing a cooling effect on the plasma itself, which rapidly becomes hotter on longitudinal axis than it is on the walls. For temperatures higher than a certain threshold (around $2\,$eV for hydrogen) the plasma electrical resistivity is monotonically increasing with the temperature, which means that the plasma offers less electrical resistance on the discharge axis than near the walls. This facilitates the concentration of current density near the axis of the discharge, which in turn deposits most part of its ohmic heating power in that region of the plasma. The process self sustains and an equilibrium condition is eventually reached.

Bobrova [19] developed a semi-analytical model to study a capillary discharge under such thermal equilibrium conditions and this model has been used recently (see for instance Ref.[131]) to compute the magnetic field in a plasma lens and explain the aberrations that have been observed experimentally. We report it here because it offers a handy representation of the physics underlying the capillary discharge in equilibrium conditions and it gives easy explanations for the lens aberration that may be observed [3].

The model has been developed for a discharge in hydrogen. It takes 1-D with axial symmetry, which means that all the physical quantities are constant over the longitudinal coordinate (also with no longitudinal motion) and the only coordinate along which any quantity may variate is the radial one. If the electrical current is constant over time, or it variates slowly enough with respect to the time required for establishing the equilibrium, the system reaches a steady state condition the plasma is in local thermodynamic equilibrium, it does not move anymore and no quantity changes over time. Under these conditions, the plasma temperature is governed by

---

[3]An extension of that model has also been developed, with the inclusion of an axial magnetic field [120]. We do not discuss it here, since its relevance is mainly related to laser channeling and not to active plasma lensing.

the heat conduction problem:

$$\frac{\mathrm{d}}{\mathrm{d}r}\left(r\kappa\frac{\mathrm{d}T}{\mathrm{d}r}\right) + \frac{E^2}{\eta} = 0, \tag{2.10}$$

$$\left.\frac{\mathrm{d}T}{\mathrm{d}r}\right|_{r=0} = 0, \tag{2.11}$$

$$T(r=0) = T^*, \tag{2.12}$$

where κ is the thermal conductivity, E is the electric field and η is the electrical resistivity. The first term represents the heat flow due to conduction, whereas the second term represents the ohmic heating. We note that under steady state condition the electric field is uniform. To write this equation, phenomena such as Nernst and Ettinghausen effect are neglected. This is possible only when the ratio between the electron cyclotron frequency (which depends on the intensity of the magnetic field) and the electron collision frequency is much smaller than 1; for the cases of our interest this condition is usually satisfied, see Ref. [19] for further information. In this condition the electrons are said to be *non magnetized*. Radiation cooling is also neglected. When the hydrogen plasma is close to full ionization and the electrons are non magnetized, one may approximate the transport parameters with [119]:

$$\kappa = \kappa_0 T^{5/2}, \quad \eta = \eta_0 T^{-3/2}, \tag{2.13}$$

being κ_0 and η_0 suitable constant values. Moreover, it is possible to define a normalized radial coordinate and a normalized temperature as:

$$s \doteq \frac{r}{R}, \quad u(s) \doteq \left[\frac{T(sR)}{A}\right]^{7/2}, \quad A \doteq \sqrt{\frac{7R^2E^2}{2\eta_0\kappa_0}}. \tag{2.14}$$

In this way, eqs. (2.10) to (2.12) may be rewritten as

$$\frac{1}{s}\frac{\mathrm{d}}{\mathrm{d}s}\left(s\frac{\mathrm{d}u}{\mathrm{d}s}\right) + u^{3/7} = 0, \tag{2.15}$$

$$\left.s'\right|_{s=0} = 0, \tag{2.16}$$

$$u(0) = u^*. \tag{2.17}$$

$$\tag{2.18}$$

Bobrova takes $T^* = 0$ and hence $u^* = 0$, but Ref.[131] considers $u^* = 0.01$ to match with rigorous numerical simulations and experiments. For symplicity we follow Bobrova's choice, even thought it is less accurate for our case. The system is easy to integrate numerically[4]. Its solution is plotted in fig. 2.2 together with the corresponding temperature, in normalized units. It is possible to compute the current density by dividing the electric field by the resistivity; the result is directly proportional to $u^{3/7}$:

$$j_z(s) = \frac{E}{\eta} = \frac{E}{\eta_0}Au^{3/7}(s). \tag{2.19}$$

---

[4]We solved it with a 4-th order collocation algorithm with control of residuals, that is implemented in the python library *scipy* (version: 0.18.1, function: integrate.solve_bvp)
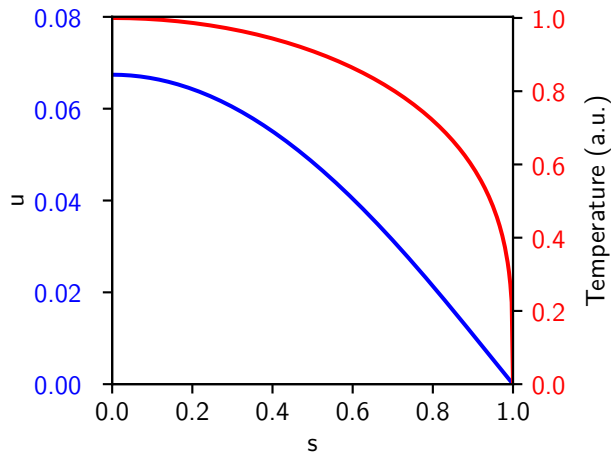
Figure 2.2. Solution of eq. (2.15) and corresponding temperature, normalized with respect to its peak value.

The magnetic field results from Ampere's law and thus may be computed as

$$B_\phi(sR) = \frac{\mu_0 R}{s} \int_0^s s' j(s') ds', \tag{2.20}$$

The result is plotted in fig. 2.3 together with the current density and the corresponding focusing gradient B_ϕ/r in normalized units. It is clear that the corresponding APL has an aberration, that may be quantified as:

$$\frac{\Delta k}{k} = \frac{k|_{s=0} - k|_{s=1}}{k|_{s=0}} \approx 0.32. \tag{2.21}$$

2.2.2 Undesired plasma wakes

When a beam passes trough an APL, it necessarily traverses a plasma region, where it excites some electron density wakes. The extent of these wakes, and the related fields and forces acting on the beam must be taken into account when evaluating the performance of the lens as a whole. The situation is such that the APL is superimposed to a passive plasma lens.

The part of plasma that sustains the electrical current of the APL is usually required to be much denser than the beam, otherwise the perturbation brought by the beam to the current carrying electrons reduces the plasma current density in the beam region and hence the lens magnetic field (and the focusing strength). The ratio of the two densities is such that the wakes produced belong to the linear regime, and the corresponding passive lens is termed as *overdense*.

Furthermore, since the electron beam must be allowed to pass through the lens preserving its quality, it is often preferred to have open capillary extremities. An alternative is the possibility of closing the capillary with polymer windows, but this solution may cause beam emittance growth due to multiple scattering[5]. If the

---

[5]A polymer (Mylar, $3\,\mu m$ thick) window has been recently used in Ref. [82], with a beam with
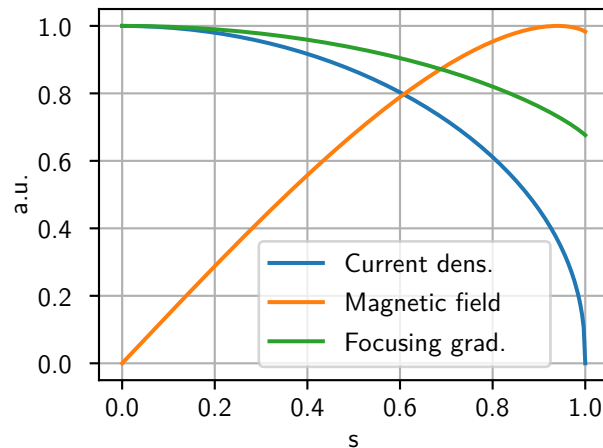
Figure 2.3. Radial profiles of magnetic field, current density and temperature in a steady state capillary discharge according to the equilibrium model in Ref. [19]. Data are plotted normalized to their peak values.

capillary extremities are open, the plasma exits from the discharge region producing plums with electron density ramps [90]. In the final part of the plums, the electron density becomes comparable or lower than the one of the beam and the generated wakes obey the non linear theory. We have an *underdense* passive plasma lens. The effects of this last part of the plums is often negligible with respect to the regions where the plasma density is higher than the one of the beam [90]. In fact, the passive focusing strength in the extremities of the plums (which is proportional to n_p) is much lower than that of the core of the APL plasma (proportional to n_b). In addition, it is usually considered that the aberrations in an underdense passive lens are also smaller than the ones of an overdense lens [124, 90]. Thus, it is reasonable to expect that the associated emittance increase is limited and plays a minor role with respect to the overdense part.

For estimating the emittance degradation due to the overdense plasma, the linear wakefield theory that has been introduced in section 1.2.1, can be used. For more accurate computations, numerical simulations exploiting more rigorous models, such as Particle-In-Cell(PIC) or hybrid PIC-fluid methods, are required. The effect of the undesired passive focusing highly depends on the specific experimental conditions, i.e. on the plasma and beam density map, and it needs to be estimated for each situation singularly.

However, in Ref. [81] some wakefield limits for high quality focusing in APLs have been analytically computed, using a combination of linear and nonlinear theory. Those analytical limitations are useful when studying the performance limitations of APLs from a general point of view, without examining the details of the single implementation. The study is based on the worst case aberration of the maximum

---

an initial normalized emittance higher than 3 mm mrad. It provided negligible emittance growth. However, one may expect that the relative emittance growth is much more relevant when the starting value is smaller (i.e. for $\epsilon_N \approx 1$ mm mrad).

focusing gradients induced by wakefield. In the thin lens limit, this leads to an approximate expression for the emittance growth [80]:

$$\Delta(\epsilon_{x,n}^2) \approx \left[\int_0^L \frac{\sqrt{7}\mu_0 e Q k_p^2 \sigma_z \sigma_x}{12(2\pi)^{3/2} m \sigma_y \left(1 + \frac{k_p \sigma_x \sigma_z}{2}\right)\left(1 + 23^{1/4} k_p^2 \sigma_z^2\right)} dz \right]^2, \qquad (2.22)$$

where Q is the beam charge. Obviously, the emittance growth in the other transverse plane (y) may be computed with the same formula, just changing the subscripts x for y. The formula works well also for asymmetric beams, up to a ratio of rms spots in the two transverse planes of the order of 10.

2.2.3   Electron scattering with plasma ions and neutrals

We discussed beam scattering on plasma ions and neutrals in section 1.2.3. Now we use eq. (1.48) to estimate the importance of this effect for typical design conditions of the active plasma lenses recently implemented and studied (see next section). We plot the emittance growth in hydrogen, helium and argon as a function of their atomic density. We assume that the gases are singly ionized and have a temperature of 4 eV. We consider a beam with a relativistic γ of 250, an rms spot size of 100 µm and a normalized emittance of 1 mm mrad. The result is shown in fig. 2.4.

It is clear that for light species like helium and hydrogen the beam degradation due to scattering is negligible up to densities of 10^{18} cm^3. Instead, for the example beam considered, the scattering in an argon gas provides non negligible emittance growth already at densities around 1×10^{17} cm^{-3}. However, experimental testing is highly desirable, in order to have more reliable estimations than what provided by the formula employed here.

2.3   Experimental advances on the use of APLs for high brightness electron beams

The first reported use of an APL is by Panofsly and Baker, that focused a 350 MeV ion beam at the 184 inch cyclotron at the Berkeley Radiation Laboratory [101]. Fifteen years later, the first z-pinch active plasma lens was operated at the AGS facility of the Brookhaven National Lab, by Forsyth et al. [56], which was used for focusing of pions and kaons. In the eighties and nineties, a motivation for the study of APLs came from the possibility of using them as final focusing for heavy ion beams, in the reactor chamber for an ion-driven-fusion scenario [37, 100, 57, 99, 97, 132] Z-pinch active plasma lenses were used at the CERN antiproton source [76, 74] and also at the GSI in Darmstadt for focusing heavy ion beams[21]; an unpinched lens was also used at the GSI on heavy ion beams[20, 122].

Recently, interests have been concentrated on the use of capillary discharges (with no pinching) for focusing electron beams. In 2015, at the BELLA center of the Lawrence Berkeley National Lab, a discharge inside a capillary of 3 cm length and 250 µm diameter was used to focus a beam of 100 MeV produced with laser-wakefield acceleration, demonstrating focusing gradients up to 3500 T m^{-1} [130]. Then at
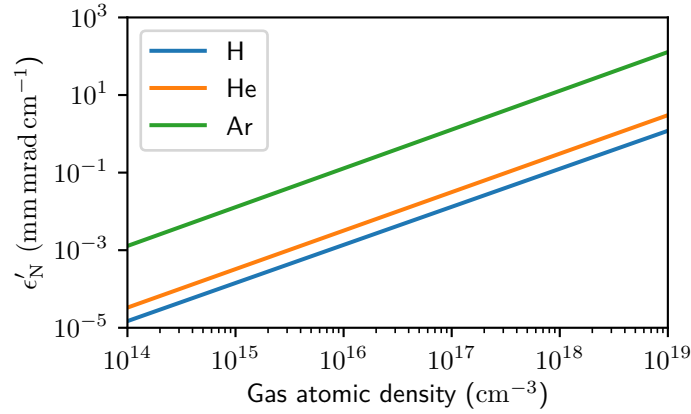
Figure 2.4. Normalized emittance growth rate for an ultra-relativistic electron beam with an emittance of 1 mm mrad, a spot of 100 µm and $\gamma = 250$ passing through singly ionized hydrogen (blue), helium (orange), argon (green) as function of the atomic number density of the gas. A gas temperature of 4 eV was assumed.

BELLA a plasma lens was used to demonstrate the staging of two laser plasma accelerators [121].

Other studies followed, a great motivation being the possibility to combine APLs with plasma wakefield acceleration. For instance, in addition to staging plasma acceleration modules, we mention the potential use of discharge capillaries for delivering small spot beams. Beams with small transverse dimensions are required in order to satisfy the matching condition at injection in plasmas. In addition, APLs may be used for capturing the highly divergent beams exiting from plasma acceleration modules.

At SPARC_Lab and at LBNL, it has been shown that the non uniformity of the current flowing inside the discharge capillary may produce aberration inside the lens, leading to over-focusing of the beam core and emittance increase [131, 108]. At LBNL a discharge in a helium filled capillary (at atomic density 8×10^{-3} cm^{-3}) with 15 mm length and 1 mm diameter was operated with a current lasting approximately 1 µs and with a peak of 440 A. Aberrations compatible with the steady state plasma model developed by Bobrova [19] (see section 2.2.1) were observed by imaging a laser-plasma accelerated beam of 60 MeV on a screen placed downstream the lens. At SPARC a hydrogen-filled 3 cm length, 1 mm diameter capillary, with a discharge lasting 1 µs and a peak current of 93 A was used for focusing a 126 MeV beam of approximately 130 µm transverse size (rms) with an initial normalized rms emittance of 1 mm mrad. Spot reduction down to 24 µm were observed, but emittance increase up to a factor 10 were also measured ((3.6 ± 2.0) mm mrad in the best case). It was inferred that due to incomplete ionization of the discharge channel, aberrations even higher than those expected from the steady state Bobrova model are possible.

At the race-track Microtron of the University of Mainz an electron beam with

great stability was used to probe the magnetic field of an active plasma lens [113]. The aberration of the lens was estimated by measuring the kick experienced by a 80 μm transverse size electron beam of 850 MeV energy inside a discharge capillary filled with hydrogen. The emittance increase was also measured, for different values of the discharge current up to 740 A, showing an increase of a factor between 2 and 6. After excluding space charge, wakefield and scattering effects, it was evident that the result was compatible with the bending of the magnetic field radial profile due to wall cooling effects on the plasma.

In 2018 at SPARC, Pompili *et. al* managed to focus a beam with substantial emittance conservation, i.e. the beam had $\epsilon_{n,x} = 0.8$ mm mrad and $\epsilon_{n,y} = 0.5$ mm mrad before entering the capillary and $\epsilon_{n,x} = \epsilon_{n,y} = 0.9$ afterwards [108]. This was achieved by means two key elements. One consisted in increasing the discharge current (from an initial setup consisting of a 93 A peak profile to a 237 A peak profile) to increase the hydrogen ionization degree. The second one consisted in taking an optimal beam size, and finding a trade off between the wake field effects and the magnetic field nonlinearity. If the beam has a small transverse spot it samples only the region of the discharge that is closer to the capillary axis, where the field exhibits a linear profile. Nevertheless, if the total charge of the beam is fixed, squeezing it too much leads to important wakefield effects. An optimum was found at a spot of approximately $\sigma_{x,y} = 115$ μm rms, for a current value of 70 A and a beam of 127 MeV energy and 50 pC charge.

At the CLEAR User Facility, Lindstrøm *et al.* (2018) performed a transverse scan of an active plasma lens, comparing the results obtained when filling their capillary (1 mm diameter, 15 mm length) with helium and with argon [82, 83]. The scan was performed by measuring the transverse kick experienced by a beam of 50 μm rms spot size. They recognized that the helium discharge exhibited a non linearity in the magnetic field profile, in accordance with what found by the other works here summarized; most importantly, it was found that the argon discharge provided a magnetic field with a linear dependence on the radial coordinate, up to measurement accuracy. While interpreting their finding, they suggest that this is due to the fact that argon gas has a lower thermal conductivity and a lower rate of thermal transfer between electrons and ions, therefore the peak current is reached before the steady state condition is established. Emittance was also measured downstream the capillary, confirming that in the helium discharge the magnetic field nonlinearity causes degradation of the beam quality, but emittance is preserved downstream the argon discharge, as expected by the measured magnetic field.

Chapter 3

Plasma production for lensing and acceleration

The work related to this thesis has been performed at the SPARC_LAB test facility (Sources for Plasma Accelerators and Radiation Compton with Lasers And Beams), located at INFN National Laboratories in Frascati [52]. SPARC_LAB is a test facility that combines a photo-injector, SPARC [1], capable of producing high brightness electron beams, and a high power, multi-hundred TW laser, FLAME [14] (Frascati Laser for Acceleration and Multidisciplinary Experiments), furnishing high intensity-ultra short pulses. The laser and the photo-injector can operate in a combined fashion as well as independently. The possibility of coordinating a high brightness linac with a high power laser for studying aspects of high interest in the field of beam physics and radiation sources. Among these, we find the laser-plasma wakefield acceleration with external injection [116], and Thomson back-scattering [128].

SPARC is a highly flexible machine, which performed extensive research activity in the field of ultra-brilliant electron beam photo-injectors [50, 114, 51] and in free electron lasers (FEL) physics [59, 75, 60, 103]. Furthermore, studies have also been carried out in the field of radiation sources other than FEL, among these, the study of THz radiation sources [62], the installation and complete characterization of a RF linac-based THz source [34] and a Thomson-back scattering experiment [128].

Recently, the facility has been focused on the application of plasmas to accelerator physics. In particular, research has been devoted to plasma-wakefield acceleration techniques, involving the generation and manipulation of high brightness electron bunch trains, that have applications in exciting resonant plasma waves for plasma wakefield acceleration and in multi color FEL [96, 35, 103, 105, 104]. Schemes of laser-wakefield acceleration that make use of external injection of witness beams in wakes generated by high power lasers, fully exploiting the combination with FLAME, are also under study [13, 116]. Beam manipulation and evolution in plasmas has been investigated [117] and special attention has been given to focusing by means of active [106, 108] as well as passive lensing [90, 115].
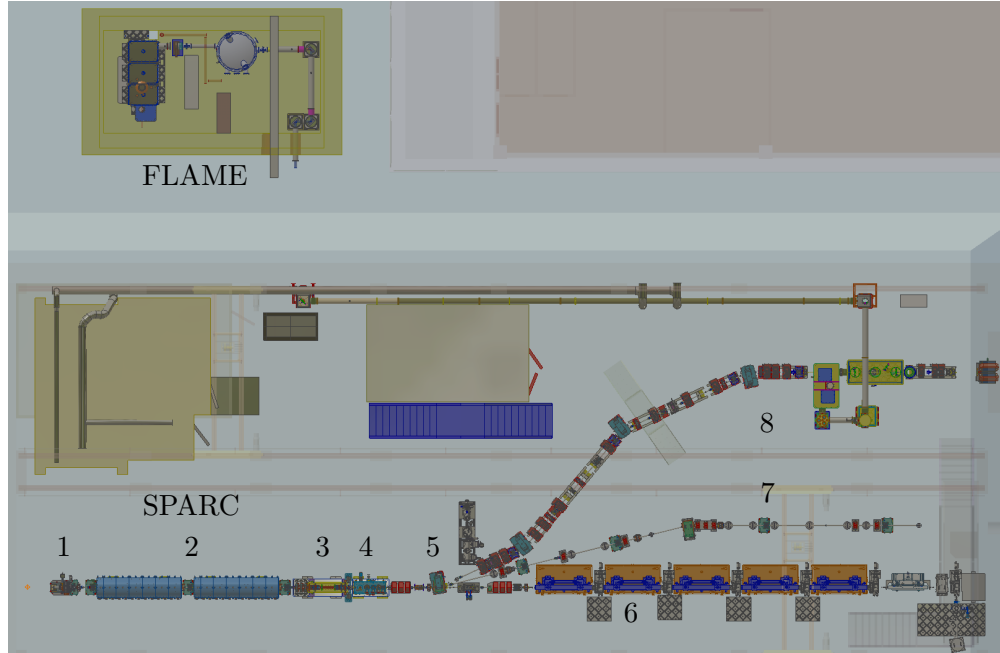
Figure 3.1. Layout of the SPARC_LAB facility. An S-band RF gun (1) is followed by two S-band accelerating cavities (2), then a last RF acceleration stage is provided by a C-band structure (3). After that the experimental chamber devoted to plasma capillaries is present (4). A tunable electromagnet dipole allows for steering the beam and transport it towards various experimental areas, as the free electron laser undulator (6) (straight line), beam diagnostics (7) (14° line), Thomson backscattering and external injection laser wakefield plasma acceleration physics (8) (25° line), in combination with the laser pulse delivered by FLAME [picture courtesy of Mario Del Franco]

3.1 Main properties of the SPARC_LAB facility

SPARC is composed by a photo-injector capable of producing electron beams up to 180 MeV. The linear accelerator feeds a 12 m long undulator and in between the acceleration sections and the undulator, the vacuum chamber hosts the plasma source for capillary discharge-related experiments. In addition, a tunable electromagnet dipole allows steering the beam and transport it towards other experimental areas, as shown in fig. 3.1, where the SPARC and FLAME bunker are schematically represented. The main beam parameters achievable at SPARC are summarized in table 3.1. For the sake of completeness, in table 3.2 the properties of the FLAME laser are presented too.

3.2 System for hydrogen discharge

The capillaries used for the experiments at SPARC_LAB are made of sapphire or of 3D-printed plastic. However, also for sapphire capillaries, a printed holding is used. In this thesis, we compare (in chapter 6) our numerical results with two capillaries that have been experimentally characterized at SPARC. They are cylindrical, with a diameter of 1 mm. One is long 1 cm and the other one is long 3 cm.
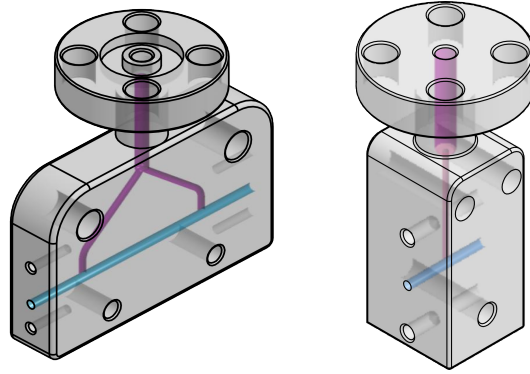
Figure 3.2. Axonometric drawing of capillary supports, for capillaries of 3 cm length (left) and 1 cm length (right), with 1 mm diameter. The blue channel represents the actual capillary, where the discharge takes place and electron beams pass through, the violet channel is used for filling the capillary with neutral gas. [Reprinted from technical drawings by V. Lollo]

Gas inlets necessary for filling the capillaries with neutral gas prior to discharging have a diameter of 0.5 mm and differ in number and position for the two cases. For 1 cm length capillaries there is a single inlet, placed at the center; for 3 cm length capillaries there are two inlets, placed at 1/4 and 3/4 of the length. An axonometric representation of the two capillaries is shown in fig. 3.2.

Two flat copper electrodes, each with a hole as wide as the capillary section, are placed at the extremities of the capillaries (see fig. 3.3) and are powered in order to trigger the discharge. They are connected to a circuit that is designed to provide the current and voltage necessary for the discharge process. A schematic representation of the electrical circuit is shown in fig. 3.4. In order to variate the time profile of the current, two discharge circuits with similar topologies but different components are available [53]. In one configuration, a capacitor of 2 nF is connected in series to a resistor of 100 Ω, whereas in the other configuration two 3.6 nF capacitors are connected in parallel (furnishing a total capacity of 7.2 nF) and then in series to a resistor of 36.5 Ω. The capacitors are charged by a high voltage generator whose current is limited by a high impedance, to prevent components damaging. A fast solid state thyristor (Belke HTS 320-200-SCR) is triggered to power the electrodes. We note that the maximum voltage sustainable by the thyristor is 25 kV; this limits the maximum voltage applicable to the capillary. Most often, the applied voltage

Table 3.1. Main properties of the SPARC photo injector

Charge	10-1000 pC
Energy	30-180 eV
Energy spread	0.01-1 %
Bunch length (FWHM)	0.1-10 ps
Spot size (rms)	5-20 µm
Normalized emittance	1-3 mm mrad
Repetition rate (max)	10 Hz
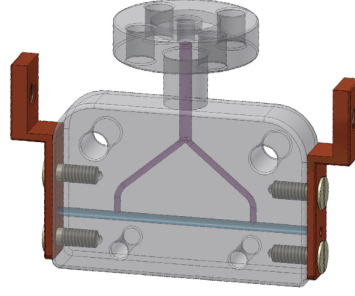
Figure 3.3. Drawing of a capillary of 3 cm length with mounted electrodes [Reprinted from Ref. [109]].
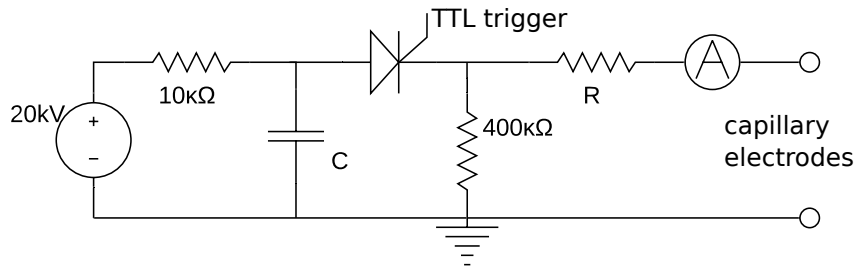
Figure 3.4. Electrical circuit used to trigger the discharge in the capillary. Two configurations have been implemented, one with the resistor $R = 100\,\Omega$ and the capacitor $C = 2\,nF$, and another with $R = 36.5\,\Omega$ and $C = 7.2\,nF$. The parasitic impedances (mainly inductive) have not been drawn.

is kept at no more than 20 kV. Furthermore, parasitic inductive impedances are present, whose measurement is not trivial. In Ref. [3] a value of 600 nH has been assumed as representative for the parasitic inductances in series with the capacitor, in the 2 nF-100 Ω circuit configuration.

The hydrogen required is provided by a generator (Linde NM Plus Hydrogen Generator) exploiting the electrolysis of water. The gas pressure is set outside the vacuum chamber, by means of a pressure regulator located more than 1 m upstream the fast valve which lets the gas flow in the capillary. The inlet pressure is usually set at few hundred millibars. The valve is opened for no more than 3 ms, then it is closed and after few microseconds the discharge is triggered. According to preliminary gas dynamics simulations performed with the open source tool OpenFoam, the gas reaches a steady flow condition during the opening of the valve. The few

Table 3.2. Main properties of the FLAME laser

Power	250 TW
Fundamental wavelength	800 nm
Energy on target	5 J
Pulse length (FWHM)	25-40 fs
Spot size	$<30\,\mu m$
Repetition rate (max)	10 Hz
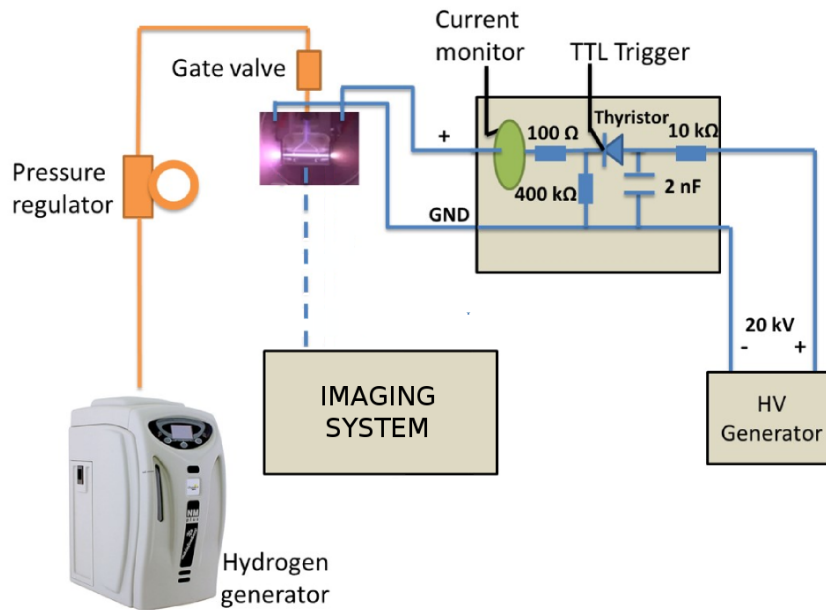
Figure 3.5. Scheme of principle of the system for capillary filling and discharging [reprinted from Ref. [53]]

microseconds waiting time is necessary only in order to distinguish the trigger signals on the oscilloscopes used to monitor the processes; however, this is a short time with respect to the typical dynamics of the gas and the flow condition does not deviate significantly from the steady state during this interval. A scheme of principle of the whole discharge system is represented in fig. 3.5 [53].

Since the plasma capillary is placed at the end of the linac and in close proximity with the C-band accelerating structure, the vacuum ressure in the plasma experimental area must be kept around 10^{-8} mbar. In this regard, several studies have been performed to define the proper opening time of the valve, i.e. 3 ms, and the most suitable repetition rate, i.e. 1 Hz., even though the other components are able to sustain higher operation rates (up to 10 Hz) and the time required for charging the capacitors is much shorter than $1\,\text{s}$[1].

3.3   Plasma diagnostics and measurements

For the measurement of the discharge current a Pearson beam current monitor (with 2ns of usable rise time) is mounted around the cable that sends current from the capacitor to a capillary electrode. Its signal is analyzed with a 500 MHz-bandwith oscilloscope (Oscilloscope LeCroy Wavesurfer 454). In fig. 3.6 two typical discharge currents are plotted. It is worth to point out that the shape of the discharge current shows little dependence on the capillary length, once the electrical circuit setting is

---

[1]This limitation applies to the experimental apparatus that has been used to benchmark the simulations of this thesis. Improvement to the whole system have undergone and discharge frequencies up to 10 Hz may currently be sustained.
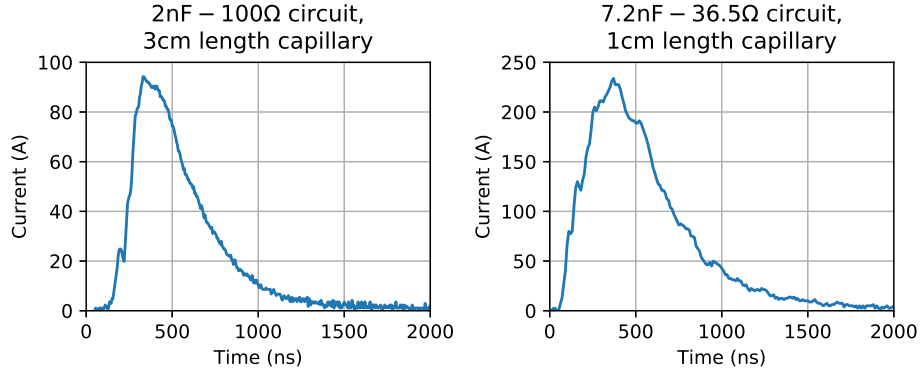
Figure 3.6. Discharge current time profiles obtained for $2\,\mathrm{nF}$-$100\,\Omega$ circuit (left) and $7.2\,\mathrm{nF}$-$36.5\,\Omega$ (right). Capacitors charging voltage is $20\,\mathrm{kV}$ and backing pressure is approximatly $300\,\mathrm{mbar}$ for both cases.
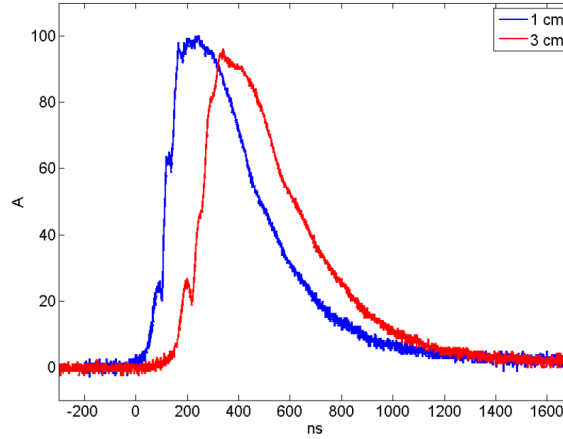
Figure 3.7. Comparison between the current profiles obtained with 1 cm long and 3 cm long capillary, by applying $20\,\mathrm{kV}$ to the $2\,\mathrm{nF}$-$100\,\Omega$ circuit [53]

fixed, the main effect being a delay (or an anticipation) of the discharge current. In fact, once ionized, the plasma offers an equivalent resistance of few ohms, which is much lower than the resistance of the other part of the system (in primis, the main limitation resistance of 100 or $36.5\,\Omega$), and therefore it plays an almost negligible role in the whole circuit. The main effect of the capillary length is a delay in the development of the discharge. In fact, by switching from a capillary of $1\,\mathrm{cm}$ to a capillary of $3\,\mathrm{cm}$ length (with the $2\,\mathrm{nF}$-$100\,\Omega$ circuit, $20\,\mathrm{kV}$ charging voltage), the current profile exhibits a very similar shape but it is translated approximately $170\,\mathrm{nm}$ forward in time, as shown in fig. 3.7 Ref.[53], page 85). This may be explained with the greater amount of energy required to ionized a bigger volume of gas. The electrical circuit requires more time to ionized the gas in the $3\,\mathrm{cm}$ capillary with respect to the $1\,\mathrm{cm}$ one and the equivalent resistance falls down slower, hence the current rises in a longer time.

The electron density is measured with longitudinal (mm) and time ($100\,\mathrm{ns}$) resolved optical method exploiting the Stark broadening effect [53, 55]. For definite

discharge conditions and capillary geometry of interest, the time profile of the current and the electron density evolution have been extensively characterized [53, 55, 54].

Recently, a measurement of gas temperature and outflow velocity has also been performed, based on the imaging of the gas plums exiting from the capillary during the discharge[11].

3.3.1 Discharge reproducibility

Capillary discharge reproducibility and shot-to-shot variation is an important requirement in order to have a reliable plasma source for either acceleration or focusing purposes. Moreover, the entity of shot-to-shot variations in plasma properties gives an insight on the underlying physics. It is well known that the process of initial ionization (the so called *electron avalanche*) of the gas starts and develops, in the first few nanoseconds, by means of kinetic effects that are not fully deterministic. If the discharge exhibited unpredictable shot-to-shot variations, this would be an indicator that kinetic and non deterministic processes play a non negligible role, thus fluid models could not be employed to study the plasma.

Discharge stability has been tested with positive results in Ref. [53]. In fact, the time required for the discharge to reach the peak current, and the value of the peak current itself, in the case of the 1 cm long capillary, for both the circuital configurations, exhibits satisfactory stability, as shown by the plots in fig. 3.8. From these plots it can be seen that the time jitter with respect to the trigger (left plots) is of few tens of nanoseconds, and the peak current (right plots) variates of no more than few amperes [53, 55, 54]. The discharge reproducibility is also confirmed by the electron density measurements performed with the technique of the Stark Broadening of Balmer–beta line[53], as it is clear from fig. 3.9.
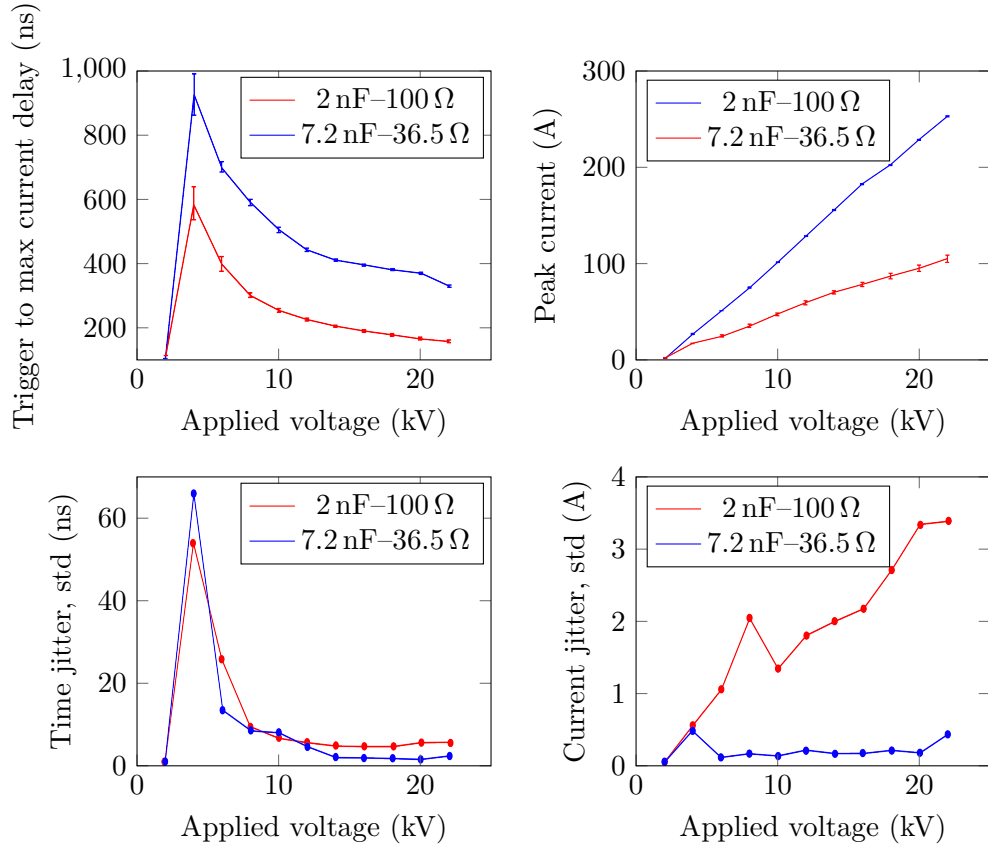
Figure 3.8. Plots showing the stability properties of the current profile for the capillary of 1 cm length, 1 mm diameter with backing hydrogen pressure of 300 mbar and for both the circuital configuration explored. In the top-left plot the average time required for reaching the peak current is displayed; the corresponding time jitter is shown as time delay standard deviation in the bottom-left plot. In the top-right plot, the average peak value of the current is plotted; the corresponding intensity jitter is shown in the bottom right plot as peak current standard deviation. These statistics refer to two samples of approximately 100 discharges [Reprinted from Ref[53]].
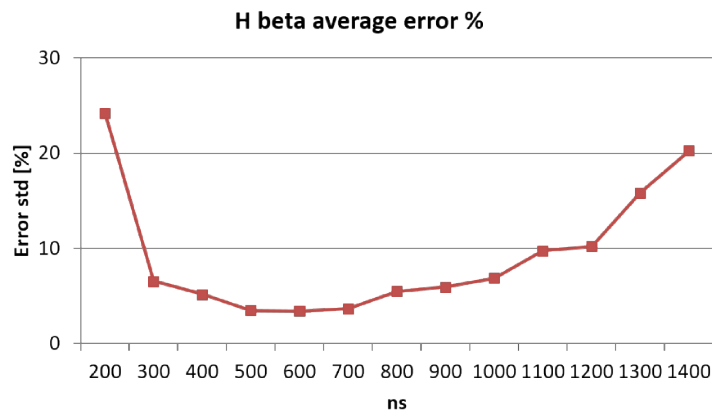
Figure 3.9. Average over the capillary length of the relative error (standar deviation) in the measurement of electron density with Stark broadening of Balmer–beta line. The measurement has been performed on a 3 cm long and 1 mm diameter capillary, fed a backing pressure of 100 mbar with a capacitor charging voltage of 20 kV [53, p. 100].

Chapter 4

Modeling a discharge plasma

In this chapter we provide an idea od the derivation of the model that we use for simulating a capillary discharge. We start by deriving multi fluid plasma models from the more general Boltzmann equation. Then we derive a single fluid model and we make further assumptions to arrive at the magneto-hydrodynamic equations that we will later use for solving capillary discharges.

4.1 From kinetic to fluid models

A plasma is an ionized gas that exhibits a collective behavior, that exists for times longer than the reciprocal of the plasma frequency and is extended in space for distances longer than the Debye length. The plasma frequency is the typical frequency at which plasma electrons oscillate after that their position has been perturbed (see appendix A). The Debye length is the typical length at which a perturbation in the plasma is screened (see appendix A). The plasma particles move under the effect of electromagnetic and gravitational forces that may be generated inside the plasma or imposed from outside.

We make the hypothesis that the knowledge of the position and velocity of each single particle of the plasma is not important for modeling the macroscopic behavior of our plasma with satisfying accuracy. Hence, the system can be described in a statistical way, by means of a single particle distribution functions $f_s(\mathbf{x}, \mathbf{u})$, per each species s present inside the plasma. This distribution models the probability corresponding the positions in the 6-D phase space $((\mathbf{x}, \mathbf{u})$, where $\mathbf{x} = (x, y, z)$ is the spacial location of a particle and $\mathbf{u} = (u_x, u_y, u_z)$ is the velocity of a particle) of a each particle belonging to the species s. Indeed, one may interpret f_s as the number of particles (of species s) per unit phase space volume. Such volume should be much smaller than the typical dimension of the whole system but big enough to contain a high number of particles. The existence of this volume is a necessary condition for the validity of a fluid description of the plasma, that we will outline in the following. Obviously, the integral over the full phase space volume Ω gives the number of particles of species s at time t:

$$\int_{\Omega} f_s \mathrm{d}^3\mathbf{x}\mathrm{d}^3\mathbf{u} = N_s(t), \tag{4.1}$$

The amount of particles inside a certain phase space control volume may vary due to different reasons. The particles may outflow the volume as they move to other spatial location or they may change their velocity under the influence of some kind of force. Their number may also increase (or decrease) due to chemical reactions that transform particles of a certain species into another.

This may be formalized by saying that $f_s(\mathbf{x}, \mathbf{u})$ fulfills Boltzmann equation:

$$\left(\frac{\partial}{\partial t} + \mathbf{u} \cdot \boldsymbol{\nabla} + \frac{\mathbf{F}_s}{m_s} \boldsymbol{\nabla}_{\mathbf{u}}\right) f_s = \left[\frac{\partial f_s}{\partial t}\right]_{\mathrm{c}}. \tag{4.2}$$

Here we have $\boldsymbol{\nabla}_{\mathbf{u}} \doteq (\frac{\partial}{\partial u_x}, \frac{\partial}{\partial u_y}, \frac{\partial}{\partial u_z})$, $\boldsymbol{\nabla} \doteq (\frac{\partial}{\partial x}, \frac{\partial}{\partial y}, \frac{\partial}{\partial z})$, and m_s is the mass of particles belonging to species s. $\mathbf{F}_s$ is a volume force acting on species s and does not include the close range forces between particles. Instead, these are included in the right hand side term, which is a source term that takes into account the combined effect of collisions between particles and chemical reactions. The term with $\mathbf{F}_s$ is responsible for the collective effects of the plasma. In addition, particle acceleration/deceleration is hidden also inside the collisional term at the right hand side and is related to forces acting at microscopic scale between particles of the same species s, as well as between species s and all the other available species.

The most important volume force in our plasma the one due to electric and magnetic fields $\mathbf{F}_s = q_s(\mathbf{E} + \mathbf{u} \times \mathbf{B})$, where $\mathbf{E}$ and $\mathbf{B}$ are the macroscopic electric and magnetic fields respectively and q_s is the particles charge of species s. Considering the small size (centimeters), the mass density (less than $1 \times 10^{-8}\,\mathrm{g\,cm^{-3}}$) of the devices that we study and the time scales at which we are interested (less than $2\,\mathrm{\mu s}$), gravity is certainly negligible.

4.1.1   Multi fluid model

Unfortunately, a kinetic description of a plasma, as the one provided by eq. (4.2), is often too complicated to be solved in reasonable amount of time. However, many of the commonly encountered plasma problems (and among these, our capillary discharges) may be solved introducing further simplifications in the model. The first of these simplifications is the derivation of a fluid description by substituting Boltzmann equation with approximate equations for certain moments of the one particle distribution function. The equations are derived by multiplying both sides of Boltzmann equation by a function of the velocity, $\psi(\mathbf{u})$, and performing an integration over the full velocity space, $\Omega_{\mathbf{u}}$. When $\psi = 1$ (zeroth order moment) we will obtain the mass conservation equation, when $\psi = m_s\mathbf{u}$ (first order moment) we will obtain the momentum conservation equation and when $\psi = mu^2$ (third order moment) we will obtain the energy conservation equation. In principle one may proceed further and consider higher order moments of Boltzmann equation. In this way additional conservation equations would be derived. Obviously, the description becomes increasingly more accurate (and more complicated) every time a new moment equation is included. However, common practice is to stop at the second one. In the following we comment on the process of derivation of the mass, momentum and energy conservation equations; the detailed calculations are available in the literature [15, 45, 110].

Zeroth order moment

When eq. (4.2) is integrated over the velocity space, the third term gives zero contribution. By using the fact that the zeroth order moment of f_s is the particle number density,

$$\int_{\Omega_\mathbf{u}} f_s \mathrm{d}^3\mathbf{u} = n_s, \tag{4.3}$$

and defining the center of mass velocity $\mathbf{v}_s$ of species s as

$$\mathbf{v}_s \doteq \frac{\int_{\Omega_\mathbf{u}} f_s \mathbf{u} \mathrm{d}^3\mathbf{u}}{n_s}, \tag{4.4}$$

a species number density conservation equation is obtained:

$$\frac{\partial n_s}{\partial t} + \boldsymbol{\nabla} \cdot (n_s \mathbf{v}_s) = \left[\frac{\partial n_s}{\partial t}\right]_\mathrm{c}. \tag{4.5}$$

The right hand side of this equation is a due to the component of the collisional term that is related to chemical reactions. If no reactions are occurring in the plasma, the right hand side will be equal to zero.

First order moment

As it is clear from eq. (4.4), the first order moment of f_s is the momentum density of species s per unit of plasma volume. The result of the computation of the first moment of Boltzmann equation is a relation that expresses the conservation of momentum for species s,

$$\frac{\partial}{\partial t}(m_s n_s \mathbf{v}_s) + \boldsymbol{\nabla} \cdot (m_s n_s \mathbf{v}_s \mathbf{v}_s) + \boldsymbol{\nabla} \cdot \vec{\mathbf{P}}_s - n_s \mathbf{F}_s = m_s \int_{\Omega_\mathbf{u}} \mathbf{u}\left[\frac{\partial f_s}{\partial t}\right]_\mathrm{c} \mathrm{d}^3\mathbf{u} - m_s \mathbf{v}_s \left[\frac{\partial n_s}{\partial t}\right]_\mathrm{c}, \tag{4.6}$$

where the quantity P_s is called *pressure tensor* and it has been defined as:

$$\vec{\mathbf{P}}_s \doteq m_s n_s \int_{\Omega_\mathbf{u}} (\mathbf{u} - \mathbf{v}_s) f_s \, \mathrm{d}^3\mathbf{u}. \tag{4.7}$$

The first term at the left hand side of eq. (4.6) comes from the first term of Boltzmann equation; the second and third terms come from the second term of Bolzmann equation. The fourth one comes from the third term of Boltzmann equation. The first term on the right hand side represent the momentum change due to collisions between the particles of species s with the particles of the other species (due to momentum conservation principle, the momentum of a certain species does not change for collisions internal to that species). Lastly, the second term at the right hand side is the loss (gain) of momentum due reactions that generate (destroy) particles of species s.

It is important to mention that the pressure tensor is usually decomposed into its isotropic and anisotropic parts,

$$\vec{\mathbf{P}}_s = p_s \vec{\mathbf{I}} + \vec{\mathbf{\Pi}}_s \tag{4.8}$$

where $\vec{\mathbf{\Pi}}_s$ is termed viscous stress tensor and p_s, the scalar pressure, is defined by:

$$p_s \doteq \frac{1}{3}m_s n_s \int_{\Omega_{\mathbf{u}}} |(\mathbf{u} - \mathbf{v}_s)|^2 f_s \, \mathrm{d}^3\mathbf{u}. \tag{4.9}$$

Using the kinetic definition of temperature,

$$T_s \doteq \frac{1}{3}\frac{m_s}{k_{\mathrm{B}}} \int_{\Omega_{\mathbf{u}}} |(\mathbf{u} - \mathbf{v}_s)|^2 f_s \, \mathrm{d}^3\mathbf{u}, \tag{4.10}$$

where k_{B} is Boltzmann constant, we may rewrite the pressure as:

$$p_s = n_s k_{\mathrm{B}} T_s. \tag{4.11}$$

Second order moment

The result of the computation of the second order moment of Boltzmann equation is:

$$\frac{\partial}{\partial t}\left(\frac{3}{2}n_s T_s + \frac{1}{2}m_s n_s v_s^2\right) + \mathbf{\nabla} \cdot \left[\mathbf{Q}_s + \vec{\mathbf{P}}_s \cdot \mathbf{v}_s + \left(\frac{3}{2}n_s T_s + \frac{1}{2}n_s m_s v_s^2\right)\mathbf{v}_s\right] =$$
$$= n_s \mathbf{v}_s \cdot \mathbf{F}_s + \frac{1}{2}m_s \int_{\Omega_{\mathbf{u}}} u^2 \left[\frac{\partial f_s}{\partial t}\right]_{\mathrm{c}} \mathrm{d}^3\mathbf{u}. \tag{4.12}$$

The quantities inside the time derivative come from the first term on the left hand side of Boltzmann equation. The terms to which the divergence operator is applied come from the second term of Boltzmann equation. The first term on the right hand side is related to the third term of Boltzmann equation. Lastly, the second term at the right hand side contains the energy gained (or lost) by species s, as a consequence of the elastic and inelastic collisions occurring in the plasma (including reactions).

The term $\mathbf{Q}_s$ is the heat flux density and is defined by:

$$\mathbf{Q}_s = \frac{1}{2}m_s n_s \int_{\Omega_{\mathbf{u}}} |\mathbf{u} - \mathbf{v}_s|^2 (\mathbf{u} - \mathbf{v}_s) f_s \, \mathrm{d}^3\mathbf{u} \tag{4.13}$$

It may be easily shown that the summation $\frac{3}{2}n_s T_s + \frac{1}{2}m_s n_s v_s^2$ is the kinetic energy of species s. Indeed, as we anticipated, we found an energy conservation equation.

Note that this equation relates the second order moments $(T_s, \vec{\mathbf{P}}_s)$ to a third order moment: the heat flux density $\mathbf{Q}_s$. If we proceeded further with the evaluation of the moments of Boltzmann equation, the next relation found would relate third order moments to new forth order moments of f_s. In order to close the model one needs to take some kind of assumption which allows to express $\vec{\mathbf{\Pi}}_s$ (contained inside $\vec{\mathbf{P}}_s$), $\mathbf{Q}_s$ and $\left[\frac{\partial f_s}{\partial t}\right]_c$ in terms of n_s, $\mathbf{v}_s$, T_s.

4.1.2   One fluid model

From the multi fluid model it is possible to derive other conservation equations, that represent a single fluid approximation of the plasma. In order to do so, it is

convenient to define the following quantities:

$$\rho = \sum_s m_s n_s, \tag{4.14}$$

$$\mathbf{v} = \frac{1}{\rho} \sum_s m_s n_s \mathbf{v}_s, \tag{4.15}$$

$$\mathbf{j} = \sum_s q_s n_s \mathbf{v}_s, \tag{4.16}$$

$$\rho_q = \sum_s q_s n_s. \tag{4.17}$$

The first equation defines the mass density, ρ; the second one defines the center of mass velocity (also called bulk velocity), $\mathbf{v}$; the third one defines the current density, $\mathbf{j}$; the forth the electric charge density, ρ_q.

We may multiply the number density conservation equations of each species by the particle mass of that species and then sum up the resulting relations. In this way one easily obtains the mass conservation equation, which is also called continuity equation:

$$\frac{\partial \rho}{\partial t} + \boldsymbol{\nabla} \cdot (\rho \mathbf{v}) = 0. \tag{4.18}$$

Note that there are no source component at the right hand side. This is an obvious consequence of the fact that in chemical reactions particles are not destroyed and neither created but only transformed from one species into another. Mass is a conserved quantity in the plasmas we study, as we have no nuclear reactions occurring.

For deriving the single fluid momentum conservation equation, one needs to redefine the pressure tensor of each species taking as reference the bulk velocity, instead of the center of mass velocity of species s:

$$\vec{\mathbf{P}}_s \doteq m_s n_s \int_{\Omega_{\mathbf{u}}} (\mathbf{u} - \mathbf{v}) f_s \, \mathrm{d}^3 \mathbf{u}. \tag{4.19}$$

Then one may build the one fluid thermal pressure tensor as:

$$\vec{\mathbf{P}} \doteq \sum_s \vec{\mathbf{P}}_s. \tag{4.20}$$

Now, recomputing the first moment of Boltzmann equations for each species, employing the new definition of species pressure tensor and summing up over the species, one obtains:

$$\frac{\partial \rho \mathbf{v}}{\partial t} + \boldsymbol{\nabla} \cdot (\rho \mathbf{v} \mathbf{v}) + \boldsymbol{\nabla} \cdot \vec{\mathbf{P}} = \rho_q \mathbf{E} + \mathbf{j} \times \mathbf{B}. \tag{4.21}$$

Note that in this equation the effect of momentum change due to collisions is not present. The reason is that the physical principle of momentum conservation obviously holds even for collisions between different species[1].

---

[1] We are neglecting the momentum of the photons generated or absorbed during chemical reactions.

One can also derive an equation for the current density, by taking the first moment of Boltzmann equation and multiply it by q_s/m_s, and then we summing up over the species. The result is:

$$\frac{\partial \mathbf{j}}{\partial t} + \sum_s q_s \boldsymbol{\nabla} \cdot \left(n_s \int_{\Omega_{\mathbf{u}}} \mathbf{u}\mathbf{u} f_s \, \mathrm{d}^3 \mathbf{u} \right) - \sum_s \frac{n_s q_s^2}{m_s} \left(\mathbf{E} + \frac{\mathbf{v}_s}{c} \times \mathbf{B} \right) = \left[\frac{\partial \mathbf{j}}{\partial t} \right]_{\mathrm{c}} \qquad (4.22)$$

The equation above is termed as *generalized Ohm's law.*

The single fluid energy conservation equation is derived in an analogous way. One also needs to redefine the heat flux density taking as reference $\mathbf{v}$:

$$\mathbf{Q} \doteq \sum_s \frac{1}{2} n_s m_s \int_{\Omega_{\mathbf{u}}} |\mathbf{u} - \mathbf{v}|^2 (\mathbf{u} - \mathbf{v}) f_s \, \mathrm{d}^3 \mathbf{u} \,. \qquad (4.23)$$

Using the previously defined quantities in the expression of the second moment of the Boltzmann equation, performing some algebra between the equations for the species we get:

$$\frac{\partial}{\partial t} \left(\frac{1}{2} \rho v^2 + \frac{3}{2} p \right) + \boldsymbol{\nabla} \cdot \left(\frac{1}{2} \rho v^2 \mathbf{v} + \frac{3}{2} p \mathbf{v} + \vec{\mathbf{P}} \cdot \mathbf{v} + \mathbf{Q} \right) = \mathbf{j} \cdot \mathbf{E} + \left[\frac{\partial \epsilon}{\partial t} \right]_{\mathrm{c}} \qquad (4.24)$$

where p is the diagonal part of $\vec{\mathbf{P}}$, $p\vec{\mathbf{I}} + \vec{\mathbf{\Pi}} = \vec{\mathbf{P}}$ and the second term at the right hand side is the energy that is generated or absorbed by the reactions occurring in the plasma (elastic collisions do not change the energy of the plasma).

We have derived three relations, that represent mass (eq. (4.18)), momentum (eq. (4.21)) and energy (eq. (4.24)) conservation equations for a single fluid description of the plasma, to which we have to add the one for the current density (eq. (4.22)). Unfortunately, these four equations do not provide a closed description of the plasma. Even if we define how to compute $\mathbf{Q}$, $\vec{\mathbf{\Pi}}$ and the collisional terms, the system does not have a unique solution, because we do not know how to compute the net charge density ρ_q and the current density $\mathbf{j}$ with no knowledge on the species fluid velocities $\mathbf{v}_s$ and number density n_s (also, we need to specify how to compute the integral in the second term of eq. (4.22)). It is clear that some additional simplifying assumptions are required in order to perform an actual (and usable) simplification of the multi fluid model to a single fluid model.

4.2 MHD model

MHD equations may be obtained by applying additional simplifications and assumptions to the one fluid equations. In the following we provide an idea of the derivation of the MHD equations that we solve in chapter 5. The main points of the derivation path are: the use of a local thermodynamic equilibrium model (section 4.2.1); the use of Ampere's law (instead of Ampere-Maxwell's) for expressing the current density (section 4.2.2); the reduction of generalized Ohm's law to a simpler relation.

4.2.1 Local thermodynamic equilibrium

We take the assumption that all the species are very fast at exchanging heat with each other, with respect to processes that heat or cool down the plasma. Under this

hypothesis, we are allowed to assume that the species have the same temperature. It is intended that the temperature is defined with respect to the bulk velocity:

$$T = T_s \doteq \frac{1}{3}\frac{m_s}{k_{\mathrm{B}}}\int_{\Omega_{\mathbf{u}}}|(\mathbf{u}-\mathbf{v})|^2 f_s\,\mathrm{d}^3\mathbf{u}\,. \tag{4.25}$$

We justify this assumption by considering the typical time of heat exchange between ions and electrons. We consider a plasma made of electrons and H^+ ions, with zero center of mass velocities: $\mathbf{v}_e = 0$, $\mathbf{v}_i = 0$. In eq. (4.12) for both electrons and ions we neglect all the other sources of temperature variation except for the electron-ion heat exchange term. This term is contained inside the collisional term at the right hand side. The two equations may be written as [69, p.34]:

$$\frac{\partial T_e}{\partial t} = \hat{\nu}_\epsilon(T_i - T_e), \tag{4.26}$$

$$\frac{\partial T_i}{\partial t} = \hat{\nu}_\epsilon(T_e - T_i), \tag{4.27}$$

where, if the electrons and ion temperature are close together ($T_i \approx T_e = T$) we have:

$$\frac{\hat{\nu}_\epsilon}{n_e} = \frac{\hat{\nu}_\epsilon}{n_i} = \frac{\lambda 3.2\times 10^{-9}\,\mathrm{s}}{(k_B T)^{3/2}} \tag{4.28}$$

where λ is the Coulomb logarithm [69, p.34], a parameter that is weekly dependent on the plasma density and temperature. Its value is usually in between a few units and a few tens. If $n_e \approx n_i$, the solution of eqs. (4.26) and (4.27) is:

$$T_i = (T_{i,0} - T_\infty)\mathrm{e}^{-t\hat{\nu}_\epsilon} + T_\infty, \tag{4.29}$$

$$T_e = (T_{e,0} - T_\infty)\mathrm{e}^{-t\hat{\nu}_\epsilon} + T_\infty, \tag{4.30}$$

where $T_{i,0}$ is the initial temperature of the ions, $T_{e,0}$ is the initial temperature of the electrons and $T_\infty = \frac{T_i + T_e}{2}$ is the equilibrium temperature. For a plasma density of $1\times 10^{17}\,\mathrm{cm}^{-3}$ and a temperatures around $1\,\mathrm{eV}$, the typical decay time of the electron-ion temperature difference is of the order of $\frac{1}{\hat{\nu}_\epsilon} \approx 1\times 10^{-9}\,\mathrm{s}$, which is below the timescales of our interest.

Furthermore, it is easy to prove that the following relation holds:

$$p = k_{\mathrm{B}}T\sum_s n_s, \tag{4.31}$$

This is usually called *thermal equation of state.*

In addition, we take the assumption that the reactions occurring inside our plasma are fast enough so that when a small perturbation in the plasma state appears, the equilibrium shifts instantaneously to a new position. As a consequence the direct and inverse processes are aways balanced and the collisional source terms in the energy conservation equation are dropped. Analogously, the chemical fractions are provided by another equation, that gives the degree of advancement of the processes from the temperature and mass density. Furthermore, an additional component appears in the energy equation of the gas, that forms, together with the pressure component, the internal energy of the plasma. This term takes into account the

energy stored in the plasma depending on the equilibrium state of the reactions. Hence, the energy conservation equation becomes:

$$\frac{\partial}{\partial t}\left(\frac{1}{2}\rho v^2 + \epsilon_{\text{int}}\right) + \boldsymbol{\nabla} \cdot \left(\frac{1}{2}\rho v^2 \mathbf{v} + \epsilon_{\text{int}}\mathbf{v} + \vec{\mathbf{P}} \cdot \mathbf{v} + \mathbf{Q}\right) = \mathbf{j} \cdot \mathbf{E} \qquad (4.32)$$

The internal energy is provided by a caloric *equation of state*, in terms of the gas temperature and mass density. At this point one may drop the species conservation equation. The actual formulas that link pressure, internal energy and temperature for our discharge studies are explained in section 5.1.2.

4.2.2   Electric and magnetic fields

One obviously needs to specify the time evolution of the electric and magnetic fields appearing in the one fluid model. Such fields obey Maxwell's equations:

$$\boldsymbol{\nabla} \times \mathbf{E} = -\frac{\partial \mathbf{B}}{\partial t}, \qquad (4.33)$$

$$\boldsymbol{\nabla} \times \mathbf{B} = \mu_0 \mathbf{j} + \mu_0 \epsilon_0 \frac{\partial \mathbf{E}}{\partial t}, \qquad (4.34)$$

$$\boldsymbol{\nabla} \cdot \mathbf{E} = \frac{\rho_q}{\epsilon_0}, \qquad (4.35)$$

$$\boldsymbol{\nabla} \cdot \mathbf{B} = 0. \qquad (4.36)$$

From eqs. (4.34) and (4.35) it is possible to derive the continuity equation for the electrical current,

$$\frac{\partial \rho_q}{\partial t} + \boldsymbol{\nabla} \cdot \mathbf{j} = 0. \qquad (4.37)$$

Just for the purpose of showing the typical decay time of an unbalanced charge ρ_q we relate the current density with the magnetic field with the usual Ohm's law $\eta \mathbf{j} = \mathbf{E}$. Substituting it inside eq. (4.37) and using eq. (4.35) we obtain

$$\frac{\partial \rho_q}{\partial t} + \frac{\rho_q}{\epsilon_0 \eta} = 0, \qquad (4.38)$$

whose solution is:

$$\rho_q = \rho_0 \mathrm{e}^{-t/t_{\text{eq}}}, \ t_{\text{eq}} = \epsilon_0 \eta \qquad (4.39)$$

If the plasma resistivity is $1\,\Omega\,\text{m}$ (this is a conservative choice, since typical values for η are often much smaller in our discharges, i.e. $1 \times 10^{-5}\,\Omega\,\text{m}$-$1 \times 10^{-3}\,\Omega\,\text{m}$), we have $t_{\text{eq}} \approx 1 \times 10^{-11}\,\text{s}$, that is much smaller than the time scales of the phenomena that we study. Hence, we may safely neglect the presence of unbalanced charges and assume that the plasma is locally *quasi-neutral*: $\rho_q \approx 0$. One may interpret this choice by imagining that when a net charge appears in the plasma, an electric field is generated which moves the electrical charges in order to recover the local neutrality.

Furthermore, we may estimate the importance of the displacement current in Ampere-Maxwell law, eq. (4.34), with respect to the other terms. A rough estimate of the order of magnitude of the electric and magnetic fields can be provided by considering that the rotor of a certain quantity scales like the inverse of a typical length of interest, $\mathcal{L}$. Analogously, the time derivative of a certain quantity scales

like the inverse of a typical time of interest, $\mathcal{T}$. With this approach, from Faraday's law, eq. (4.33), we get

$$\frac{E}{\mathcal{L}} \approx \frac{B}{\mathcal{T}} \Rightarrow E \approx \frac{\mathcal{L}B}{\mathcal{T}}, \tag{4.40}$$

and eq. (4.34) becomes

$$\frac{B}{\mathcal{L}\mu_0} \approx j + \frac{\epsilon_0 E}{\mathcal{T}}. \tag{4.41}$$

The importance of the displacement current may be estimated by computing the ratio of term containing the electric field to the term containing the magnetic field in eq. (4.41),

$$\frac{\frac{B}{\mu_0\mathcal{L}}}{\frac{\epsilon_0 E}{\mathcal{T}}} = \frac{\frac{B}{\mu_0\mathcal{L}}}{\frac{\epsilon_0\mathcal{L}B}{\mathcal{T}^2}} = \frac{\mathcal{T}^2}{\mathcal{L}^2}c^2, \tag{4.42}$$

where we used the relation $c^{-2} = \epsilon_0\mu_0$. Since we are only interested in modeling phenomena that have characteristic speeds, $\mathcal{V}$, much smaller than the speed of light, $\mathcal{L}/\mathcal{T} = \mathcal{V} \ll c$, we may safely neglect the displacement current term in eq. (4.34).

4.2.3 Ohm's law in MHD

We use local quasi-neutrality assumption to rewrite eq. (4.22). We write it for a plasma composed only by electrons and singly ionized ions. This is a situation similar to the one of our hydrogen filled capillary discharges, with the exception that when the plasma is not fully ionized we also have neutral particles. However, neutrals only affect the collisional term at the right hand side of that equation.

Under the assumptions above, eq. (4.22) becomes:

$$
\begin{aligned}
\mathbf{E} + \mathbf{v} \times \mathbf{B} = & \frac{1}{ne}\mathbf{j} \times \mathbf{B} \\
& - \frac{1}{ne}\boldsymbol{\nabla} \cdot \left(\vec{\mathbf{P}}_e - \frac{m_e}{m_i}\vec{\mathbf{P}}_i \right) \\
& + \frac{m_e}{ne^2}\left[\frac{\partial \mathbf{j}}{\partial t} + \boldsymbol{\nabla} \cdot (\mathbf{uj} + \mathbf{ju}) \right] \\
& + \frac{1}{ne}\mathbf{R}_e,
\end{aligned}
\tag{4.43}
$$

where we used $n \doteq n_e = n_i$ (which makes sense because of local charge neutrality) and $\mathbf{R}_e$ is the resultant of the forces related to collisions between electrons and ions. It is the only term coming from the collisional term at the right hand side of eq. (4.22), and it has been derived neglecting the ion contribution to the current density. In eq. (4.43) the first term on the right hand side corresponds to the electromotive force due to Hall effect. The second term represents the so-called thermoelectric effects, i.e. those electromotive forces resulting from pressure gradients. The third term represents the effects related to electron inertia.

It is worth to mention that eq. (4.22) provides a description of the current density evolution that is too detailed for most purposes. The order of magnitude of the first and second terms on the right hand side is much smaller than that of the $\mathbf{v} \times \mathbf{B}$, when the Larmor radius (see appendix A for the definition of Larmor radius) is smaller than the typical length of the spatial variations in the plasma. In addition,

the third term is negligible when the electron inertia is neglected. At this point we are left only with:

$$\mathbf{E} + \mathbf{v} \times \mathbf{B} = \frac{1}{ne}\mathbf{R}_e. \tag{4.44}$$

We may rewrite the right hand side term by imagining that electrons collide with ions at a certain frequency ν_{ei} and that they loose their momentum after a collision. Therefore we pose:

$$\mathbf{R}_e = m_e n \mathbf{v}_e \nu_{ei}. \tag{4.45}$$

Using also the definition of current density (remember that we neglected the ion contribution to the current), eq. (4.44) becomes:

$$\mathbf{E} + \mathbf{v} \times \mathbf{B} = \frac{m_e \nu_{ei}}{ne^2}\mathbf{j} = \eta\mathbf{j}, \tag{4.46}$$

where we defined the electrical resistivity as $\eta \doteq \frac{m_e \nu_{ei}}{ne^2}$. For fully ionized gases the computation of electrical resistivity in terms of electron-ion collision frequency provides usually sufficient accuracy. Nevertheless, when partially ionized gases are studied, the electrical resistivity is often computed with more rigorous strategies, that also take into account also the scattering with neutrals (as well as the collisions between electrons). For our discharges we used the Chapman-Enskog method, that does not involve the computation of a collision frequency for the electrons section 5.3. However, we reported the definition of η above as it is useful for understanding the physics and to explain the proportionality between the electric and magnetic field terms on the left hand side of eq. (4.46) and the current density.

Lastly we mention that in literature also eq. (4.46) is often termed as generalized Ohm's law.

4.2.4   Pressure tensor and heat flux

In order to close the system, we still have to specify how to compute the pressure tensor $\vec{\mathbf{P}}$ and the heat flux density $\mathbf{q}$. For the heat flux density a natural choice is to link it with the temperature gradient by means of Fourier's law:

$$\mathbf{q} = -\kappa\boldsymbol{\nabla}T. \tag{4.47}$$

The proportionality constant between the temperature gradient and the heat flux, κ, is called thermal conductivity. In our model we compute it with the Chapman-Enskog method, as we do for the electrical resistivity. For a more detailed discussion on heat flux see Ref. [30].

For the pressure tensor, we keep only the diagonal part, which contains the pressure. Hence we rewrite its divergence as:

$$\boldsymbol{\nabla} \cdot \vec{\mathbf{P}} \approx \boldsymbol{\nabla}p \tag{4.48}$$

4.2.5   MHD equations

For convenience, we rewrite here the equations that we derived for modeling the plasma as a single fluid, with the assumption of local quasi-neutrality, local thermodynamic equilibrium, using the simplified form of the generalized Ohm's law,

neglecting the displacement current, with the choice of Fourier law for heat flow and a thermal equation of state for the temperature:

$$\frac{\partial \rho}{\partial t} + \boldsymbol{\nabla} \cdot (\rho \mathbf{v}) = 0, \tag{4.49}$$

$$\frac{\partial \rho \mathbf{v}}{\partial t} + \boldsymbol{\nabla} \cdot (\rho \mathbf{v} \mathbf{v}) + \boldsymbol{\nabla} p = \mathbf{j} \times \mathbf{B}, \tag{4.50}$$

$$\frac{\partial}{\partial t}\left(\frac{1}{2}\rho v^2 + \epsilon_{\text{int}}\right) + \boldsymbol{\nabla} \cdot \left(\frac{1}{2}\rho v^2 \mathbf{v} + \epsilon_{\text{int}} \mathbf{v} + p \mathbf{v}\right) + \kappa \boldsymbol{\nabla} T = \mathbf{j} \cdot \mathbf{E}, \tag{4.51}$$

$$\mathbf{E} + \mathbf{v} \times \mathbf{B} = \eta \mathbf{j}, \tag{4.52}$$

$$\boldsymbol{\nabla} \times \mathbf{E} = -\frac{\partial \mathbf{B}}{\partial t}, \tag{4.53}$$

$$\boldsymbol{\nabla} \times \mathbf{B} = \mu_0 \mathbf{j}, \tag{4.54}$$

$$\boldsymbol{\nabla} \cdot \mathbf{E} = 0, \tag{4.55}$$

$$\boldsymbol{\nabla} \cdot \mathbf{B} = 0. \tag{4.56}$$

This system may be reduced and adapted to a more convenient formulation.

One may substitute $\mathbf{E} \cdot \mathbf{j}$ in eq. (4.51) with the expression that may be obtained from Poynting's theorem,

$$\frac{1}{\mu_0}\boldsymbol{\nabla} \cdot (\mathbf{E} \times \mathbf{B}) + \epsilon_0 \mathbf{E} \cdot \frac{\partial \mathbf{E}}{\partial t} + \frac{\mathbf{B}}{\mu_0} \cdot \frac{\partial \mathbf{B}}{\partial t} = -\mathbf{J} \cdot \mathbf{E}. \tag{4.57}$$

where we may also neglect the term containing the time derivative of the electric field, in agreement with what we did for Ampere-Maxwell law. Also, we use eq. (4.52) to express the electric field in terms of current density and eq. (4.54) to express the current density in terms of the magnetic field. Reordering the result one obtains:

$$\frac{\partial \epsilon}{\partial t} + \boldsymbol{\nabla} \cdot (\epsilon \mathbf{v}) = - \boldsymbol{\nabla} \cdot (p \mathbf{v}) + \boldsymbol{\nabla} \cdot (\kappa \boldsymbol{\nabla} T),$$
$$- \boldsymbol{\nabla} \cdot \left[\left(\frac{\eta}{\mu_0^2}\boldsymbol{\nabla} \times \mathbf{B}\right) \times \mathbf{B}\right],$$
$$+ \frac{1}{\mu_0}\boldsymbol{\nabla} \cdot [\mathbf{B}(\mathbf{B} \cdot \mathbf{v})], \tag{4.58}$$

where we defined the *total energy*, ϵ, as:

$$\epsilon \doteq \epsilon_{\text{int}} + \frac{\rho \mathbf{v}^2}{2} + \frac{\mathbf{B}^2}{2\mu_0}. \tag{4.59}$$

Furthermore, we may take the rotor of eq. (4.52) and substitute eq. (4.53) for the rotor of the electric field. We may also use again eq. (4.54) to express the current density in terms of the magnetic field in the resulting equations, as well as in eq. (4.50). In this way we obtain a system of equations where the electric field and the current density do not appear explicitly. Note that we may also drop eq. (4.56) because it follows from eq. (4.53) that the divergence of the magnetic field does not change in time. Thus if we properly choose the initial conditions,

i.e. $\boldsymbol{\nabla} \cdot \mathbf{B}(t = 0) = 0$, the magnetic field will remain divergence free.[2]. The final (rearranged) form of the system is:

$$\frac{\partial \rho}{\partial t} + \boldsymbol{\nabla} \cdot (\rho \mathbf{v}) = 0, \tag{4.60}$$

$$\frac{\partial}{\partial t}(\rho \mathbf{v}) + \boldsymbol{\nabla} \cdot (\rho \mathbf{v} \mathbf{v}) = \frac{1}{\mu_0}(\boldsymbol{\nabla} \times \mathbf{B}) \times \mathbf{B} - \boldsymbol{\nabla} p, \tag{4.61}$$

$$\frac{\partial \epsilon}{\partial t} + \boldsymbol{\nabla} \cdot (\epsilon \mathbf{v}) = -\boldsymbol{\nabla} \cdot (p\mathbf{v}) + \boldsymbol{\nabla} \cdot (\kappa \boldsymbol{\nabla} T),$$

$$-\boldsymbol{\nabla} \cdot \left[\left(\frac{\eta}{\mu_0^2} \boldsymbol{\nabla} \times \mathbf{B} \right) \times \mathbf{B} \right],$$

$$+\frac{1}{\mu_0} \boldsymbol{\nabla} \cdot [\mathbf{B}(\mathbf{B} \cdot \mathbf{v})], \tag{4.62}$$

$$\frac{\partial \mathbf{B}}{\partial t} = \boldsymbol{\nabla} \times (\mathbf{v} \times \mathbf{B}) - \boldsymbol{\nabla} \times \left[\frac{\eta}{\mu_0}(\boldsymbol{\nabla} \times \mathbf{B}) \right]. \tag{4.63}$$

.

---

[2]This is true if the equations are solved exactly. In fact, for certain approximate numerical solutions of the MHD equations a *divergence control* method is required for the magnetic field divergence to remain close to zero.

Chapter 5

Numerical model of capillary discharges

In this chapter the mathematical model and numerical techniques employed to simulate gas filled capillary discharge are explained. We model the plasma as a compressible fluid, since a particle in cell approach would be computationally impractical, due to the time scales involved ($>1\,\mu$s) and to the spacial resolution required ($<100\,\mu$m). Thus, we employed a *magneto-hydrodynamic* (MHD) model, as explained in section 5.1. Furthermore, we take a *local thermodynamic equilibrium* (LTE) assumption, which allows to compute the plasma chemical composition and internal energy (by means of en equation of state), as a function of the local fluid temperature and density, instead of integrating in time the reaction equations. The transport parameters required in the MHD equations, i.e. the electrical resistivity and thermal conductivity, are computed within the Chapman-Enskog framework, using accurate collision integrals from the literature; the details of the computation are provided in section 5.3.

The model is numerically solved with the open source code PLUTO [93][1], which is a software developed for the numerical solution of mixed hyperbolic/parabolic systems of partial differential equations, arising from gas and plasma flows in astrophysical fluid dynamics. Facilitated by the modular and flexible design structure of the code, we implemented an additional scheme, meant for advancing the diffusive term of the magnetic field evolution equation and the diffusive term of the energy conservation equation in an implicit fashion. This has been done with the aim of overcoming the severe time step limitations due to explicit methods, that are well suited for the main field of application of the code, that may also run on parallel machines, but perform poorly when applied to the study of capillary discharges on serial machines. In subsection section 5.4.1 the implicit solution of the diffusive terms is explained in detail.

---

[1]See also `http://plutocode.ph.unito.it/`

5.1 Plasma as a compressible fluid

We model the plasma as a compressible fluid. Especially, we chose a one fluid MHD model, thereby taking the assumption of locally neutral plasma (i.e. that ions and electrons always move in order to mutually neutralize their charge) and also neglecting fast varying electromagnetic phenomena (i.e. the displacement current in Ampere-Maxwell equation). In addition, since we aim at studying discharges in cylindrically shaped capillaries, we solve the problem inside an axially symmetric geometry, where the symmetry axis coincident with the capillary axis. This choice greatly simplifies the study with respect to a fully 3-D geometry, while still allowing to investigate the effect of gas outflow from the capillary extremities during the development of the discharge.

5.1.1 Magneto-hydrodynamic model

The MHD system that we solve is the one composed by eqs. (4.60) to (4.63). For the sake of completeness, we rewrite those equations in cylindrical components notation, applying also the simplifications due to the axial symmetry:

$$\frac{\partial \rho}{\partial t} + \frac{1}{r}\frac{\partial}{\partial r}(r\rho v_r) + \frac{\partial}{\partial z}(\rho v_z) = 0, \tag{5.1}$$

$$\rho\left(\frac{\partial v_r}{\partial t} + v_r\frac{\partial v_r}{\partial r} + v_z\frac{\partial v_r}{\partial z}\right) = -\frac{\partial p}{\partial r} - \frac{B_\phi}{\mu_0 r}\frac{\partial}{\partial r}(rB_\phi), \tag{5.2}$$

$$\rho\left(\frac{\partial v_z}{\partial t} + v_r\frac{\partial v_z}{\partial r} + v_z\frac{\partial v_z}{\partial z}\right) = -\frac{\partial p}{\partial r} - \frac{B_\phi}{\mu_0}\frac{\partial B_\phi}{\partial z}, \tag{5.3}$$

$$\rho\left(\frac{\partial \epsilon}{\partial t} + v_r\frac{\partial \epsilon}{\partial r} + v_z\frac{\partial \epsilon}{\partial z}\right) = -p\left[\frac{1}{r}\frac{\partial}{\partial r}(rv_r) + \frac{\partial v_z}{\partial z}\right],$$
$$+ \frac{1}{r}\frac{\partial}{\partial r}\left(r\kappa\frac{\partial T}{\partial r}\right) + \frac{\partial}{\partial z}\left(\kappa\frac{\partial T}{\partial z}\right),$$
$$+ \frac{\eta}{\mu_0^2}\left[\left(\frac{\partial B_\phi}{\partial z}\right)^2 + \frac{1}{r^2}\left(\frac{\partial}{\partial r}(rB_\phi)\right)^2\right], \tag{5.4}$$

$$\frac{\partial B_\phi}{\partial t} = -\frac{\partial}{\partial z}\left(v_z B_\phi\right) - \frac{\partial}{\partial r}\left(v_r B_\phi\right),$$
$$+ \frac{\partial}{\partial z}\left(\frac{\eta}{\mu_0}\frac{\partial B_\phi}{\partial z}\right) + \frac{\partial}{\partial r}\left(\frac{\eta}{\mu_0}\frac{1}{r}\frac{\partial r B_\phi}{\partial r}\right), \tag{5.5}$$

where r is the radial coordinate, z is the longitudinal coordinate and ϕ is the azimuthal coordinate.

5.1.2 Local thermodynamic equilibrium

The plasma chemistry is modeled exploiting an LTE assumption. We assume that the reactions occurring in the plasma are always locally at steady state, thus we compute the composition only by knowing the temperature and the mass density; as a result, the pressure and the internal energy are provided by an equation of state. In the following, we first explain how we compute the plasma composition, then we write the expressions for the thermal pressure and internal energy.

Hydrogen dissociation and ionization

The computation of the composition of a hydrogen gas in LTE conditions, according to Saha's teory is here briefly discussed. More details can be found in the literature [61, 31, 71].

The main reactions taking place in hydrogen in the range of temperature and mass densities of our interest are the molecular dissociation and atomic ionization, both represented in table 5.1.

For the range of temperature and mass density of our interest, dissociation of hydrogen molecules and ionization of hydrogen atoms are the most important chemical processes. The corresponding energy required is written in table 5.1.

Table 5.1. Dissociation and ionization processes occurring in a hydrogen gas.

Process	Reaction	Energy required
Molecular dissociation	$H_2 \rightarrow H + H$	$\Psi = 4.476\,\mathrm{eV}$
Atomic ionization	$H \rightarrow H^+ + e^-$	$\chi = 13.597\,\mathrm{eV}$

From considerations on the partition function [61] it is possible to derive the following relations between the component concentrations and the gas temperature:

$$\frac{n_H^2}{n_{H_2}} = e^{\Psi/(k_B T)}\left(\frac{2\pi k_B T}{h^2}\frac{m_H^2}{m_{H_2}}\right)^{3/2} \tag{5.6}$$

$$\frac{n_p n_e}{n_H} = e^{\chi/(k_B T)}\left(\frac{2\pi k_B T}{h^2}\frac{m_p m_e}{m_{H_2}}\right)^{3/2} \tag{5.7}$$

If we call n_0 the concentration of H_2 molecules at low temperature (when dissociation and ionization have not taken place yet), the four concentrations can be expressed using two reaction coordinates, x, y, as:

$$n_{H_2} = (1-x)n_0 \tag{5.8}$$

$$n_H = 2(x-y)n_0 \tag{5.9}$$

$$n_p = n_e = 2yn_0. \tag{5.10}$$

Rearranging the eqs. (5.6) to (5.10), the system becomes:

$$\frac{[2(x-y)]^2}{1-x} = \frac{e^{\Psi/(k_B T)}}{n_0}\left(\frac{2\pi k_B T}{h^2}\frac{m_H^2}{m_{H_2}}\right)^{3/2} \doteq \alpha \tag{5.11}$$

$$\frac{(2y)^2}{2(x-y)} = \frac{e^{\chi/(k_B T)}}{n_0}\left(\frac{2\pi k_B T}{h^2}\frac{m_p m_e}{m_H}\right)^{3/2} \doteq \beta \tag{5.12}$$

From these two coupled nonlinear equations it follows

$$\frac{16}{\alpha\beta}y^4 + 2y^2 + \beta y - \beta = 0. \tag{5.13}$$

The only acceptable root of this polynomial can be very easily computed with a root finding algorithm[2]. We note that in order to calculate x once y is known, the

---

[2]The one we employed relies on the computation of the eigenvalues of the companion matrix, from the open source python package *numpy*, `https://docs.scipy.org/doc/numpy-1.15.0/reference/generated/numpy.roots.html`
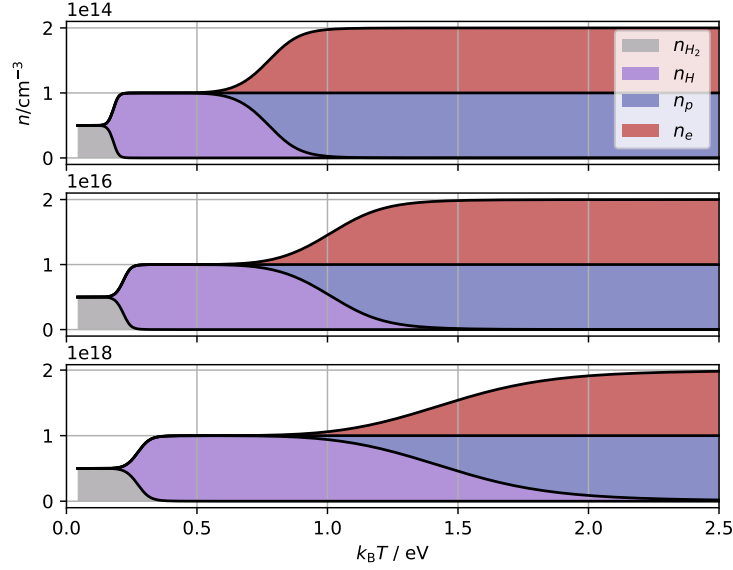
Figure 5.1. Concentration of free electrons, H$^+$ ions, H atoms and H$_2$ molecules as function of temperature and for different densities.

expression

$$x = \frac{-(\alpha - 8y) + \sqrt{(\alpha - 8y)^2 - 16(4y^2 - \alpha)}}{8} \tag{5.14}$$

has better numerical stability than the simpler

$$x = y\left(1 + 2\frac{y}{\beta}\right), \tag{5.15}$$

which exhibits some oscillations when x is supposed to smoothly approach zero. Figure 5.1 shows the concentrations of reactants with varying temperature for different densities of pure hydrogen in LTE conditions, computed with the Saha model just explained. It is clear that, for the concentrations of our interest, ionization and dissociation may be treated as separate processes, since when ionization takes place, the gas is already fully dissociated. Moreover, if we are not interested in plasma temperatures below 0.3 eV-0.4 eV, we may take the assumption of fully dissociated hydrogen.

In this case, the system reduces to Saha's equation for hydrogen ionization degree, y:

$$\frac{y^2}{1 - y} = \frac{m_p}{h^3} \frac{(2\pi m_e k_B T)^{3/2}}{\rho} e^{-\chi/(k_B T)}, \tag{5.16}$$

where we used also the relations $n_0 \approx \frac{\rho}{2m_p}$ and $m_H \approx m_p$. And we have that:

$$n_{H_2} = 0, \tag{5.17}$$

$$n_H = 2(1 - y)n_0, \tag{5.18}$$

$$n_p = n_e = 2yn_0. \tag{5.19}$$

In our numerical studies we always initialize the hydrogen at a temperature of at least $0.3\,\mathrm{eV}$, and lower temperatures are found only in regions of minor interest (i.e. not inside, nor in the vicinity of the capillary), that have negligible influence on the rest of the computational domain. Thus we decide to neglect the molecular dissociation process (i.e. we assume that our gas is always fully dissociated) and we compute the ionization degree using eq. (5.16). Obviously, in this way we miss to study the initial development of the discharge, where the gas heats up from room temperature to few thousands of Kelvin. Unfortunately, that part of the discharge cannot be modeled with a 2-D MHD approach. Indeed the fluid model itself is not applicable and one would need to perform a kinetic study. Nevertheless, once the arc regime is established in the discharge, the kinetic effects have minor importance (for the range of parameters that we study) and the fluid model is applicable. A hint that the initial kinetic development has little relevance for the subsequent arc discharge comes from the experimental repeatability of the discharges that we study (see Ref. [53] for more details on discharge reproducibility). In fact, the initial gas ionization is also a stochastic process, which is expected to behave slightly differently from shot to shot.

Internal energy and thermal pressure

We model the gas with a *thermal* equation of state, i.e. the pressure is computed with:

$$p = n k_\mathrm{B} T \approx (1 + y) \frac{\rho}{m_\mathrm{p}} k_\mathrm{B} T. \tag{5.20}$$

To compute the internal energy, we take into account the three translational degrees of freedom of the species H, H^+ and e^-, and we include the contribution of the ionization energy:

$$\epsilon_\mathrm{int} = \frac{3}{2} n k_\mathrm{B} T + \chi n_{H^+} \approx \frac{3}{2} (1 + y) \frac{\rho}{m_\mathrm{p}} k_\mathrm{B} T + \chi y \frac{\rho}{m_\mathrm{p}} \tag{5.21}$$

5.2 Boundary conditions and geometry

In this thesis we model only straight capillaries; we do not include tapered or curved shapes. We aim at emulating the experimental environments in which discharge capillaries are typically located, i.e. a vacuum chamber of dimensions greater than the size of capillary. A description of the discharge system implemented at SPARC_LAB can be found in section 3.2. We model only a small portion of the real vacuum environment, taking care that it is sufficiently big with respect to the rest of the capillary. The size of the region mimicking the vacuum outside the capillary is usually longer than the capillary and it is more than 5 times wider. In fig. 5.2 a schematic view of the computational domain is represented, including the boundary conditions applied on which we will comment below. The computational domain is discretized with a non-uniform rectilinear grid. The grids that we typically employ have a number of cells between 25000 and 100000. Note that the domain drawn in fig. 5.2 has a concave/reentrant shape. For this reason, we also implemented the possibility of setting the boundary conditions for the reentrant corner cells in a rigorous way.
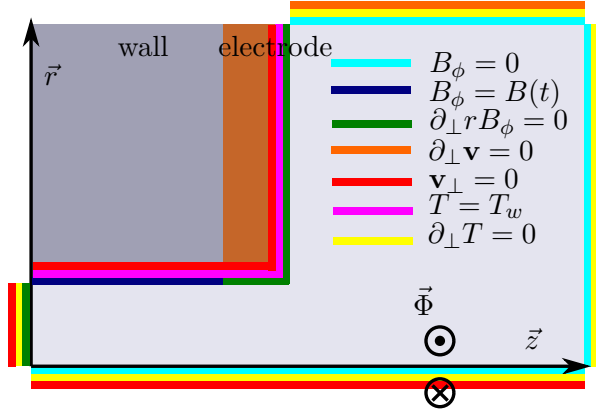
Figure 5.2. Schematic view of the domain, not in scale

5.2.1 Symmetries

As anticipated, we employed a 2-D, cylindrically symmetric geometry. The symmetry axis is coincident with the capillary axis, which is defined by the points where $r = 0$. In addition, we placed another symmetry plane at the center of the capillary, even though the physical system is not rigorously symmetric with respect to that plane. What brakes the symmetry is the $\mathbf{v} \times \mathbf{B}$ term in eq. (4.63). The velocity vector is expected to point outwards at both the capillary extremities, as the gas exits from the discharge region because of the thermal pressure generated inside. Instead, the magnetic field is expected to point in the same direction at both extremities (either entering in or exiting from the computational plane). Thus their vector product has different orientations at the two extremities. Nevertheless, if this played an effective role in the whole computation, one would find appreciable differences between solutions obtained with different current flow directions (with no variation in the other settings). During our tests, we could not find such effects; thus, we concluded that the error due to this symmetry forcing is acceptable. Note that the choice of placing this additional symmetry plane may be physically interpreted as if we closed the capillary at the center with a flat electrode and connected a current generator between this plate and one of the electrodes located at the capillary extremity.

5.2.2 Boundary conditions

In our simulations we impose the time profile of the electrical current flowing in the gas. We do that by imposing the value of the magnetic field on the cylindrical capillary wall, such that its circulation around the capillary section gives the desired electrical current (according to Ampere's law). On the portion of capillary wall that represents the electrode, we do not impose the value of the magnetic field, but we prescribe that the gradient of the product between the magnetic field and the radial coordinate is parallel to the electrode surface. This condition is equivalent to imposing the orthogonality of the electric field to the electrodes surface.

Thermal conduction occurs between the plasma and the rigid capillary walls (including the electrodes). Accurately modeling convective heat exchange between
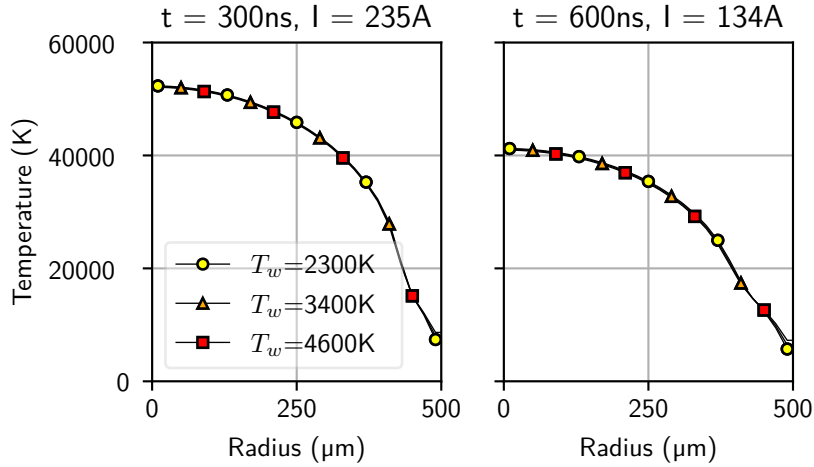
Figure 5.3. Radial temperature profiles computed in a discharge capillary with different boundary conditions. The profiles at 300 ns from the beginning of the discharge (corresponding to a current of 235 A) have been plotted on the left. The profiles at 600 ns from the beginning of the discharge (corresponding to a current of 135 A) have been plotted on the right.

fluid and surface is challenging. From an experimental point of view it is difficult to know which phenomena play an important role depending on the regime explored. From a computational point of view, high temperature gradients are expected in a thin layer just below the rigid wall surface: a very dens mesh, with short time steps would be required in order to model the process, retaining stability and/or satisfying accuracy. Bobrova [19] and Broks [26] performed this modeling (with different strategies) in their 1-D studies.

We imposed various fixed temperature values on the capillary walls and checked for differences in the computed solutions. We have seen that for boundary temperatures in the range 2600 K-4600 K(corresponding to 0.2 eV-0.4 eV) no important difference is visible in the transverse temperature profiles. In fig. 5.3 we compare the results for a simulation of a 3 cm long capillary, with a diameter of 1 mm, uniformly filled with a mass density of 2.5×10^{-7} g cm^{-3} and with an imposed current having a peak value of 235 A and lasting approximately 1.2 µs[3]. As a consequence, we chose not to model in detail the wall surface heating and we set it to a constant temperature of 3400 K. This is also the temperature at which we initialize the hydrogen gas in the domain, as explained above.

Regarding the rigid walls, advection of mass density momentum energy and magnetic field cannot occur across those interfaces. Thus the component of the velocity orthogonal to such surfaces is set to zero. Practically, this occurs on the dielectric capillary walls, on the electrodes, on the symmetry axis $r = 0$ and on the symmetry plane $z = 0$.

---

[3]A profile of this current is plotted in fig. 6.2

5.3 Transport parameters

The thermal conductivity and electrical resistivity are computed assuming a fully dissociated, partially ionized hydrogen gas. The mixture is thus entirely composed by monatomic species. In this section, whenever useful to simplify the notation, we will use integer subscripts to refer to the plasma components:

$$1 \leftrightarrow \mathrm{e}^-, \quad 2 \leftrightarrow \mathrm{H}^+, \quad 3 \leftrightarrow \mathrm{H}. \tag{5.22}$$

For computing the plasma transport parameters, we employ one of the most accurate and rigorous techniques available, which consists in using high approximations of the Chapman–Enskog method. Note that the transport models that have been used in many of the capillary discharge studies available in literature are not suitable for our case [19, 26, 6]. Indeed the accuracy of the thermal conductivity and electrical resistivity employed in those works is poor for temperatures below 20 000 K; and we certainly need to explore situations where the gas temperature is also below that value.

Regarding the Chapman–Enskog method, most of the required expressions have been developed in the fifties and sixties [39, 40, 41, 67, 24, 29] (a review of the theory is available in Ref.[71, 30]). Those expressions depend on quantities called *collision integrals*, whose accuracy is crucial for obtaining satisfactorily accurate transport parameters. We employed the same collision integrals as used by Bruno et al. [27], who computed the hydrogen transport parameters for temperatures between 50 K and 50 000 K and a pressure of 1atm. Then we compared our results with the ones of Ref. [27].

5.3.1 Thermal conductivity

In the computation of the thermal conductivity we take into account the translational component contribution, κ_{tr}, as well as the reactive contribution, κ_{reac}, but we neglect the internal thermal conductivity contribution, κ_{int}:

$$\kappa = \kappa_{\mathrm{tr}} + \kappa_{\mathrm{reac}} + \kappa_{\mathrm{int}} \approx \kappa_{\mathrm{tr}} + \kappa_{\mathrm{reac}}. \tag{5.23}$$

The internal thermal conductivity takes into account the heat flow due to the diffusive transport of enthalpy related to the excited states under thermal equilibrium conditions. The reason why we neglect it is that for the range of temperatures of 3400 K-50 000 K, it is few points percent with respect to the reactive one, as it is evinced from Ref.[27, table VIII].

For the translational contribution to the thermal conductivity, we exploited the discussion given by Devoto[39], particularizing the relations for our gas mixture and choosing the third approximation of the Chapman-Enskog formalism (unless differently specified). The expression for κ_{tr} (see Ref. [39, eq. (17)]) is:

$$\kappa_{\mathrm{tr}} = \kappa' + \frac{\rho k_{\mathrm{B}}}{n} \sum_{i,j=1}^{3} \frac{E_{ij} D_i^{\mathrm{T}} D_j^{\mathrm{T}}}{n_i m_i m_j}, \tag{5.24}$$

where $n \doteq \sum n_i$, E_{ij} is the element at row i and column j of the inverse of the matrix whose elements are $D_{ij} m_j$. D_{ij} and D_i^{T} are respectively the diffusion and

the thermal diffusion coefficients (see Ref. [39, eq. (9)]):

$$
D_{ij} = \frac{3\rho n_i}{2nm_j|\mathbf{q}|}\sqrt{\frac{2\pi k_{\mathrm{B}}T}{m_i}}
\begin{vmatrix}
\mathbf{q}^{00} & \mathbf{q}^{01} & \mathbf{q}^{02} & \mathbf{0} \\
\mathbf{q}^{10} & \mathbf{q}^{11} & \mathbf{q}^{12} & \begin{matrix} n_{\mathrm{e}} \\ n_{\mathrm{H}^+} \\ n_{\mathrm{H}} \end{matrix} \\
\mathbf{q}^{20} & \mathbf{q}^{21} & \mathbf{q}^{22} & \mathbf{0} \\
\delta_{\mathrm{e},i}\ \ \delta_{\mathrm{H}^+,i}\ \ \delta_{\mathrm{H},i} & \mathbf{0} & \mathbf{0} & 0
\end{vmatrix}
\tag{5.25}
$$

$$
D_i^{\mathrm{T}} = \frac{15n_i\sqrt{2\pi m_i k_{\mathrm{B}}T}}{4|\mathbf{q}|}
\begin{vmatrix}
\mathbf{q}^{00} & \mathbf{q}^{01} & \mathbf{q}^{02} & \begin{matrix} \delta_{\mathrm{e},j}-\delta_{\mathrm{e},i} \\ \delta_{\mathrm{H}^+,j}-\delta_{\mathrm{H}^+,i} \\ \delta_{\mathrm{H},j}-\delta_{\mathrm{H},i} \end{matrix} \\
\mathbf{q}^{10} & \mathbf{q}^{11} & \mathbf{q}^{12} & \mathbf{0} \\
\mathbf{q}^{20} & \mathbf{q}^{21} & \mathbf{q}^{22} & \mathbf{0} \\
\delta_{\mathrm{e},i}\ \ \delta_{\mathrm{H}^+,i}\ \ \delta_{\mathrm{H},i} & \mathbf{0} & \mathbf{0} & 0
\end{vmatrix}
\tag{5.26}
$$

where $|\mathbf{q}|$ is the determinant of the matrix that one build by stacking together the submatrices $\mathbf{q}^{mp}$, and placing each element at the macro-row m and macro-column n, with $m,n = 0,1,2$. $\mathbf{q}^{mp}$ matrices are defined as:

$$
\mathbf{q}^{mp} \doteq \begin{pmatrix}
q_{\mathrm{ee}}^{mp} & q_{\mathrm{eH}^+}^{mp} & q_{\mathrm{eH}}^{mp} \\
q_{\mathrm{H}^+\mathrm{e}}^{mp} & q_{\mathrm{H}^+\mathrm{H}^+}^{mp} & q_{\mathrm{H}^+\mathrm{H}}^{mp} \\
q_{\mathrm{He}}^{mp} & q_{\mathrm{HH}^+}^{mp} & q_{\mathrm{HH}}^{mp}
\end{pmatrix}.
\tag{5.27}
$$

The parameter κ' is defined by [39, eq.(14)]:

$$
\kappa' = -\frac{75k_{\mathrm{B}}}{8}\frac{\sqrt{2\pi k_{\mathrm{B}}T}}{|\mathbf{q}|}
\begin{vmatrix}
\mathbf{q}^{00} & \mathbf{q}^{01} & \mathbf{q}^{02} & \mathbf{0} \\
\mathbf{q}^{10} & \mathbf{q}^{11} & \mathbf{q}^{12} & \begin{matrix} n_{\mathrm{e}} \\ n_{\mathrm{H}^+} \\ n_{\mathrm{H}} \end{matrix} \\
\mathbf{q}^{20} & \mathbf{q}^{21} & \mathbf{q}^{22} & \mathbf{0} \\
\mathbf{0}\ \ \ \frac{n_{\mathrm{e}}}{\sqrt{m_{\mathrm{e}}}}\ \ \frac{n_{\mathrm{H}^+}}{\sqrt{m_{\mathrm{H}^+}}}\ \ \frac{n_{\mathrm{H}}}{\sqrt{m_{\mathrm{H}}}} & \mathbf{0} & \mathbf{0} & 0
\end{vmatrix}
\tag{5.28}
$$

The q_{ij}^{mp} parameters can be expressed in terms of the collision integrals and are defined in Ref. [39].

The reactive thermal conductivity takes into account the heat flow due to the diffusive transport of enthalpy related to the chemical reactants and products concentration gradients occurring under thermal equilibrium conditions when a temperature gradient is present. We compute the κ_{reac} coefficient with the expressions developed by Butler and Brokaw [29, 24] who neglect thermal diffusion, pressure gradients and external force field in order to obtain a handy formulation. For the actual computation, we particularized the expressions from Ref [71, eq. (5.29) to (5.32)], that are only a slight modification of (but equivalent to) the ones by Butler and Brokaw, considering that we have only one chemical reaction.

We call R_i the stoichiometric coefficients of the ionization reaction:

$$
R_{1 \leftrightarrow \mathrm{e}^+} = +1, \quad R_{2 \leftrightarrow \mathrm{H}^+} = +1, \quad R_{3 \leftrightarrow \mathrm{H}} = -1,
\tag{5.29}
$$

The enthalpy of the reaction is defined as:

$$\Delta H = \sum_{i=1}^{3} R_i H_i, \tag{5.30}$$

where H_i is the enthalpy per particle of species i. One can easily compute the enthalpy per particle by noting that it is equivalent to the product of the mass of that particle by the mass specific enthalpy of a gas of that particle,

$$H_i = h_i m_i, \tag{5.31}$$

thus:

$$H_1 = \frac{3}{2}\frac{k_{\mathrm{B}}T}{m_1} + \frac{p_1}{\rho_1} = \frac{5}{2}\frac{k_{\mathrm{B}}T}{m_1}, \tag{5.32}$$

$$H_2 = \frac{3}{2}\frac{k_{\mathrm{B}}T}{m_2} + \frac{\chi}{m_2} + \frac{p_2}{\rho_2} = \frac{5}{2}\frac{k_{\mathrm{B}}T}{m_2} + \frac{\chi}{m_2}, \tag{5.33}$$

$$H_3 = \frac{3}{2}\frac{k_{\mathrm{B}}T}{m_3} + \frac{\chi}{m_3} + \frac{p_2}{\rho_3} = \frac{5}{2}\frac{k_{\mathrm{B}}T}{m_3}. \tag{5.34}$$

Therefore the enthalpy of the atomic ionization reaction is:

$$\Delta H = \frac{5}{2}k_{\mathrm{B}}T + \chi. \tag{5.35}$$

If we define:

$$A \doteq \sum_{i=1}^{2} \sum_{j=i+1}^{3} \frac{k_{\mathrm{B}}T}{\hat{D}_{ij}} x_i x_j \left(\frac{R_i}{x_i} - \frac{R_j}{x_j} \right)^2, \tag{5.36}$$

where $x_i = n_i/n$ and $\hat{D}_{ij}$ is defined by

$$\hat{D}_{ij} = \frac{3}{16} \frac{(k_{\mathrm{B}}T)^2}{p m_{ij} \Omega_{i,j}^{(1,1)}}, \tag{5.37}$$

where $\Omega_{i,j}^{(1,1)}$ is a collision integral, a quantity that will be defined in section 5.3.3. Therefore, we may write the reactive thermal conductivity as [24, eq. (3)]:

$$\kappa_{\mathrm{reac}} = \frac{1}{k_{\mathrm{B}}T^2} \frac{(\Delta H)^2}{|A|} \tag{5.38}$$

5.3.2   Electrical resistivity

For the electrical conductivity, Devoto's third order expression is used, neglecting the contribution of the ions to the current. From Ref.[39], eq. (29):

$$\eta = \frac{\rho k_{\mathrm{B}}T}{\mathrm{e}^2 n} \frac{1}{n_2 m_2 D_{1,2}} \tag{5.39}$$

5.3.3 Collision integrals for the computation of transport parameters

Collision integrals are parameters that result from three integrations performed in sequence. The first integration computes the scattering angle of interacting particles, and involves their trajectories, which depend on the impact parameter, on the interaction potential and on their initial velocities. From the second integration a cross section is computed by weighting all possible impact parameters by a function depending on the scattering angle. Finally, the third integration considers all the initial velocities and weights the cross sections by a function which depends on these velocities. The expression for the collision integral of order (l, s) (with l and s positive integers) for the interaction of species i and j is

$$\Omega_{i,j}^{(l,s)} = \sqrt{\frac{k_{\mathrm{B}}T}{2\pi m_{i,j}}} \int_0^\infty \gamma^{2s+3} Q_{i,j}^{(l)}(\gamma^2 k_{\mathrm{B}}T)\mathrm{e}^{-\gamma^2}\,\mathrm{d}\gamma\,, \tag{5.40}$$

where $\gamma = \frac{m_{i,j}g^2}{2k_{\mathrm{B}}T}$, g is the initial particle relative speed at large distance, $m_{ij} = \frac{m_i m_j}{m_i + m_j}$ is the reduced mass, and $Q_{i,j}^{(l)}$ is the transport cross section, defined by

$$Q_{i,j}^{(l)}(\epsilon_{i,j}) = 2\pi \int_0^\infty \left[1 - cos^l\chi_{i,j}(\epsilon_{i,j}, b)\right] b\,\mathrm{d}b, \tag{5.41}$$

with b being the impact parameter and $\chi_{i,j}$ the scattering angle:

$$\chi_{i,j}(\epsilon_{i,j}, b) = \pi - 2b \int_{r_0}^\infty \frac{\mathrm{d}r}{r^2\sqrt{1 - \frac{b^2}{r^2} - \frac{V(r)}{\epsilon_{i,j}}}}. \tag{5.42}$$

In the previous expression $r = |\mathbf{r}| = |\mathbf{r}_i - \mathbf{r}_j|$ is the distance between the colliding particles and $V(r)$ is their interaction potential, i.e. the scalar field whose gradient drives the evolution of the relative position of the particles:

$$m_{ij}\frac{\partial^2 \mathbf{r}}{\partial t^2} = -\boldsymbol{\nabla}V(r). \tag{5.43}$$

We computed the values of the collision integrals for the interactions between charged particles ($\mathrm{H}^+ - \mathrm{e}^-$, $\mathrm{H}^+ - \mathrm{H}^+$, $\mathrm{e}^- - \mathrm{e}^-$) using the analytical approximation developed by Hahn *et al.* [64, eq. (51)], where the approximation of screened screened Coulomb potential was employed. In order to use the analytical approximation of Ref. [64] an expression for the Debye length is required. We use the expression of Debye length that includes the screening of both electrons and ions (that we reported in eq. (A.1), see appendix A for more details), because this is the correct formulation when ion and electron temperatures are equal[27][4]. For the interaction between hydrogen atoms and between hydrogen atoms and hydrogen ions, we used the fitting expression from Bruno [27, eq. (11)]). Lastly, for the electron-hydrogen atom interaction, it is employed the fitting expression of Ref.[27, eq. (19)].

---

[4]For a discussion concerning the inclusion of the ion and electron contributions in the Debye length, see Ref. [71, pp.99-100]
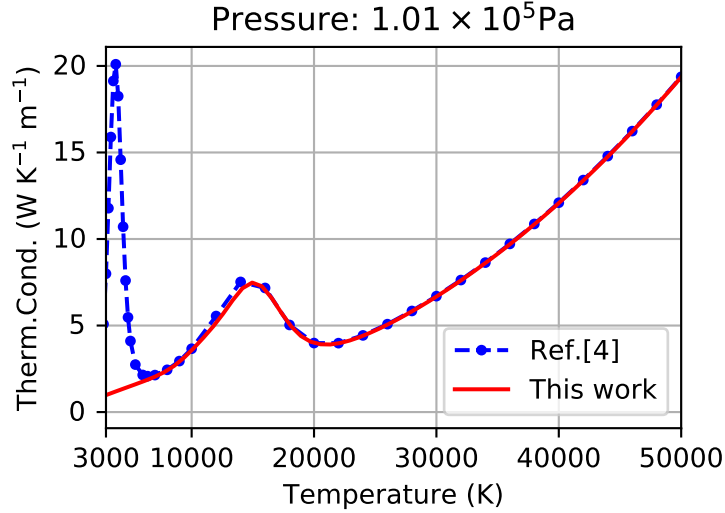
Figure 5.4. Comparison between the total thermal conductivity as computed in this work, and as computed by Ref.[27, table VIII],

5.3.4 Comparison with literature

In the following, we compare the electrical resistivity and the thermal conductivity that we computed with the results by Ref. [27].

In fig. 5.4 the thermal conductivities of LTE hydrogen are plotted as a function of temperature at atmospheric pressure. One can notice that the agreement is satisfactory for the range of temperatures 6000 K-50 000 K, while for temperature below 5000 K the agreement is poor. The difference is due to the fact that our model neglects the reactive conductivity component related to molecular dissociation[5]. However, when the electrical discharge develops, most part of the plasma heats up quickly (in a few tens of nanoseconds) and reaches temperature above 5000 K. Thus, we are confident that such inaccuracy in the thermal conductivity does not represent a major issue for the accuracy of the whole discharge simulation, since it will affect only a small portion of less hot plasma, mainly located near the capillary walls or outside from the capillary.

In fig. 5.4 the electrical resistivity is plotted as a function of temperature at atmospheric pressure. As expected, the agreement is excellent for the full range of the plotted temperature.

5.4 Numerical solution of the MHD system

The code PLUTO is used to solve the model equations with a finite volumes approach. The whole dissipative MHD problem can be viewed as composed by a so called hyperbolic part (which is related to the advection of mass, momentum, energy and magnetic field) and a parabolic part (related to the diffusion-like processes, such as

---

[5]As shown by [27, table (VIII)], at temperatures of few thousand kelvin, the reactive component of the thermal conductivity is much greater than the translational and internal ones
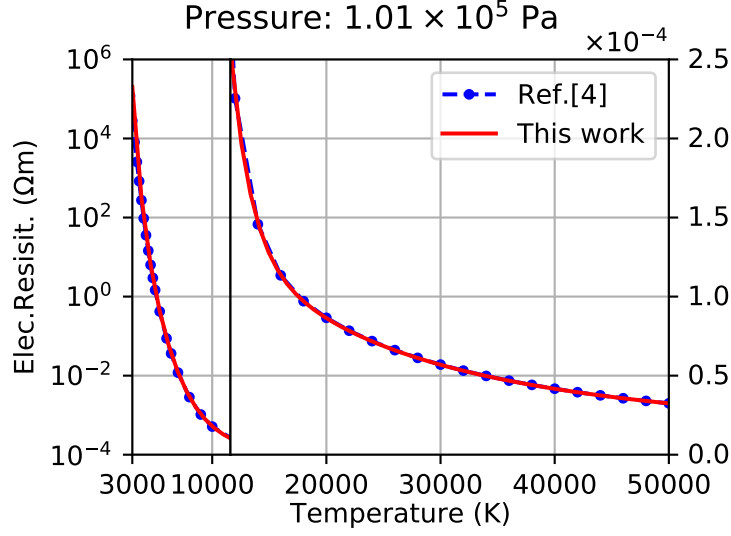
Figure 5.5. Comparison between the electrical resistivity as computed in this work, and as computed by Ref.[27], table VIII.

the thermal conduction and magnetic field evolution due to resistivity). Thus, we can equivalently rewrite eqs. (4.60) to (4.63) as:

$$\frac{\partial \mathbf{U}}{\partial t} + \mathbf{H}(\mathbf{U}) + \mathbf{P}(\mathbf{U}) = \mathbf{0} \tag{5.44}$$

Where $\mathbf{U}$ represents the conservative variables

$$\mathbf{U} \doteq \begin{pmatrix} \rho \\ \rho\mathbf{v} \\ \epsilon \\ \mathbf{B} \end{pmatrix}, \tag{5.45}$$

$\mathbf{H}$ is a (non-strict) hyperbolic operator, defined by

$$\mathbf{H}(\mathbf{U}) \doteq \boldsymbol{\nabla} \cdot \begin{pmatrix} \rho\mathbf{v} \\ \rho\mathbf{v}\mathbf{v} - \frac{1}{\mu_0}\mathbf{B}\mathbf{B} + \mathbf{I}p \\ (\epsilon + p)\mathbf{v} - \frac{1}{\mu_0}\mathbf{B}(\mathbf{v}\cdot\mathbf{B}) \\ \mathbf{v}\mathbf{B} - \mathbf{B}\mathbf{v} \end{pmatrix}, \tag{5.46}$$

and $\mathbf{P}$ is the operator containing parabolic terms, defined by

$$\mathbf{P}(\mathbf{U}) \doteq \begin{pmatrix} 0 \\ \mathbf{0} \\ -\boldsymbol{\nabla}\cdot(\kappa\boldsymbol{\nabla}T) + \boldsymbol{\nabla}\cdot\left[\left(\frac{\eta}{\mu_0^2}\boldsymbol{\nabla}\times\mathbf{B}\right)\times\mathbf{B}\right] \\ +\boldsymbol{\nabla}\times\left[\frac{\eta}{\mu_0}(\boldsymbol{\nabla}\times\mathbf{B})\right] \end{pmatrix}. \tag{5.47}$$

Considering that the hyperbolic and parabolic parts have different dynamics and bring different time step limitations to the solution scheme, we chose to employ a

splitting technique, in order to prevent the most restrictive time step limitation (usually the diffusive one) to affect the computational effort required for the whole solution. In PLUTO, the Strang splitting technique is implemented.

When the Strang splitting is applied to a system like 5.44, the computed solution is advanced in time applying only one operator at a time, and alternating the operators and the time step width as [78]:

$$\mathbf{U}^{n+1} = e^{\mathbf{H}\frac{\Delta t}{2}} e^{\mathbf{P}\Delta t} e^{\mathbf{H}\frac{\Delta t}{2}} \mathbf{U}^n \qquad (5.48)$$

The order of alternation of the operators is not prescribed a priori, however it may affect the stability and accuracy of the solution. In fact, one may apply the opposite order:

$$\mathbf{U}^{n+1} = e^{\mathbf{P}\frac{\Delta t}{2}} e^{\mathbf{H}\Delta t} e^{\mathbf{P}\frac{\Delta t}{2}} \mathbf{U}^n. \qquad (5.49)$$

After some testing, we chose the splitting 5.49, which performed better in terms of robustness.

We solve the problem related to the **H** operator with the an explicit finite volumes method, already implemented in PLUTO. Specifically, the time stepping is performed with a second order Runge-Kutta method and the single time advance is performed with a dimensionally split approach, with linear spatial reconstruction and employing the Rieman solver by Harten, Lax and Van Leer [127, 44]. The problem represented by the **P** operator is solved with a semi implicit scheme belonging to the family of the alternating direction implicit methods (ADI) as discussed in section 5.4.1. Since the only component of the magnetic field is in the ϕ direction, its divergence is identically null and there is no need to apply any divergence control scheme, which would otherwise be required.

5.4.1 Implicit method for parabolic operators

In order to show the impracticality of solving the eqs. (4.61) to (4.63) with a fully explicit scheme, we take as example a linear one dimensional diffusion equation:

$$\frac{\partial w}{\partial t} = D\frac{\partial^2 w}{\partial x^2}. \qquad (5.50)$$

When trying to solve it with an explicit scheme, in order to keep the method stable[6], the time step, Δt, must be limited by a quantity which is directly proportional to the square of the grid spacing Δx and inversely proportional to the diffusion parameter D [8],

$$\Delta t \leq C\frac{(\Delta x)^2}{D}. \qquad (5.51)$$

The quantity C is the Courant-Friedrichs-Lewy number, it is of the order of the unity and it depends on the particular method employed and on the dimensionality of the problem. It is common practice to keep it well below 0.5. The extension of the limitation 5.51 to multidimensional problems and to other geometries only adds technical details which complicate the discussion but do not change the conclusions of the argument. Further information can be found in Ref.[8]. If we apply this limit

---

[6]Note that this is only a necessary condition for stability.

to the case of magnetic field diffusion with a uniform resistivity of $1\,\Omega\,\mathrm{m}$ and we prescribe a grid spacing of $10\,\mu\mathrm{m}$, we have

$$D = \frac{\eta}{\mu_0} \approx 8 \times 10^5\,\mathrm{m}^2\,\mathrm{s}^{-1}, \tag{5.52}$$

and thus:

$$\Delta t \leq C\frac{(10\,\mu\mathrm{m})^2}{8 \times 10^5\,\mathrm{m}^2\,\mathrm{s}^{-1}} \approx C \cdot 1.3 \times 10^{-16}\,\mathrm{s}. \tag{5.53}$$

If we wish to solve up to few microseconds, we have to advance in time the solution for some billion steps, this is clearly impractical on serial workstations available nowadays.

There exist some techniques, usually called *super time stepping* methods, capable of accelerating an explicit scheme. Among those we find the Runge-Kutta-Legendre (RKL) and the Runge-Kutta-Chebyshev (RKC) methods [92, 2]. At the time of writing, both the RKL and RKC are implemented in the production version of PLUTO[129], nonetheless when we carried out our studies only the RKC was available[7]. We tested it for some of the problems of our interest and we found that the method was capable of accelerating an explicit scheme by a factor 10 to 100, which is still not sufficient for running our simulations on a serial machine. Moreover, RKC exhibited poor robustness for the problems of our interest. Thus we decided to implement an ADI scheme.

Alternating direction implicit methods

Alternating direction implicit (ADI) methods allow to overcome the time step limitations of the explicit schemes, while still avoiding some of the complications of fully implicit methods. They consist in *predictor corrector* schemes where the predictor step evolves implicitly only a part of the differential operator (the other part is evolved explicitly) and the corrector step evolves implicitly the remaining other part of the operator (instead, the first part evolved explicitly). One may decide to split the operator along the directions (r and z for us), which practically results in alternating explicit and implicit updates of the solution vector along the different coordinates For the case of diffusive problems, such as heat conduction or magnetic field diffusion in 2-D [8], discretized with 5 points stencil centered finite differences, ADI schemes are capable of providing more accurate solutions than a Strang splitting performed on the directions; still requiring only to solve linear systems whose matrices are tridiagonal. This translates in ease of implementation with respect to fully implicit methods, that require the inversion of banded sparse matrices.

Among the most studied, we find the Peaceman-Rachford (PR) [102] and the Douglas-Rachford (DR) [42] variants. To illustrate how the ADI methods work, we take the simple case of an initial value problem of the form:

$$\frac{\mathrm{d}}{\mathrm{d}t}\Psi + A(\Psi, t) = 0, \tag{5.54}$$

$$\Psi(0) = \Psi_0 \tag{5.55}$$

---

[7]We are referring to PLUTO's version 4.2 (August 2015)
[8]For the generalization to 3-D situations, see Ref. [63].

for $t > 0$, where the operator A may be decomposed in two simpler components A_1, A_2, such that: $A = A_1 + A_2$.

The PR method aims to solve it by stepping from t^n to t^{n+1} with the scheme:

$$\frac{\Psi^{n+1/2} - \Psi^n}{\Delta t/2} + A_1(\Psi^{n+1/2}, t^{n+1/2}) + A_2(\Psi^n, t^n) = \mathbf{0}, \qquad (5.56)$$

$$\frac{\Psi^{n+1} - \Psi^{n+1/2}}{\Delta t/2} + A_1(\Psi^{n+1/2}, t^{n+1/2}) + A_2(\Psi^{n+1}, t^{n+1}) = \mathbf{0}, \qquad (5.57)$$

where $t^{n+1/2} = t^n$ is the midpoint between t^n and t^{n+1} and $\Delta t = t^{n+1} - t^n$. It is worth to mention that $\Psi^{n+1/2}$ is only an intermediate result fo the calculation and should not be treated as an approximation of $\Psi(t^{n+1/2})$. Clearly, the predictor step advances for a half time step the solution according to A_1 operator using forward Euler method, and according to A_2 using backward Euler method. In the corrector step the roles of the operators are reversed. If A_1 and A_2 they are linear, time independent and commute, the scheme is second order accurate. For further information on PR scheme see Ref.[63].

The DR method aims to solve the problem of eqs. (5.54) and (5.55) by stepping from t^n to t^{n+1} with the scheme:

$$\frac{\widehat{\Psi}^{n+1} - \Psi^n}{\Delta t} + A_1(\widehat{\Psi}^{n+1}, t^{n+1}) + A_2(\Psi^n, t^n) = \mathbf{0}, \qquad (5.58)$$

$$\frac{\Psi^{n+1} - \Psi^n}{\Delta t} + A_1(\widehat{\Psi}^{n+1}, t^{n+1}) + A_2(\Psi^{n+1}, t^{n+1}) = \mathbf{0}, \qquad (5.59)$$

A first difference with the PR scheme is that the roles of A_1 and A_2 are not symmetrical; some authors suggest to take as A_2 the operator with the best continuity and monotonicity properties[63]. Also, even if A_1 and A_2 are linear, time independent and commute, the scheme is not second order accurate like PR, but first order at best. However, even though in principle the accuracy of this scheme is lower than that of PR, the prominent role played by backward differencing gives often better stability. This is confirmed by the literature [63] and by a number of numerical tests that we performed In the following we explain how we apply the and ADI scheme to our computational problem. When solving the diffusion-like problem we first split the $\mathbf{P}$ operator (see eq. (5.47)) in two parts,

$$\mathbf{P}(\mathbf{U}) = \mathbf{P}_1(\mathbf{U}) + \mathbf{P}_2(\mathbf{U}), \qquad (5.60)$$

$$\mathbf{P}_1(\mathbf{U}) = \begin{pmatrix} 0 \\ \mathbf{0} \\ -\boldsymbol{\nabla} \cdot (\kappa \boldsymbol{\nabla} T) \\ \mathbf{0} \end{pmatrix} \qquad (5.61)$$

$$\mathbf{P}_2(\mathbf{U}) = \begin{pmatrix} 0 \\ \mathbf{0} \\ \boldsymbol{\nabla} \cdot \left[\left(\frac{\eta}{\mu_0^2} \boldsymbol{\nabla} \times \mathbf{B} \right) \times \mathbf{B} \right] \\ +\boldsymbol{\nabla} \times \left[\frac{\eta}{\mu_0} (\boldsymbol{\nabla} \times \mathbf{B}) \right] \end{pmatrix}, \qquad (5.62)$$

and advance $\mathbf{P}_1$ and $\mathbf{P}_2$ alternatively, performing a Lie splitting between the problems of thermal conduction and magnetic diffusion:

$$e^{\mathbf{P}\Delta t}\mathbf{U} \approx e^{\mathbf{P}_2\Delta t}e^{\mathbf{P}_1\Delta t}\mathbf{U}. \qquad (5.63)$$

In addition, for stability reasons we further subdivide the diffusion time step in N sub-steps (few tens) and perform a sub-cycling applying an ADI scheme on each one of them ($j = 1, 2$):

$$e^{\mathbf{P}_j \Delta t} \mathbf{U} \approx \underbrace{e^{\mathbf{P}_j \frac{\Delta t}{N}} \cdot \ldots \cdot e^{\mathbf{P}_j \frac{\Delta t}{N}}}_{N \text{ times}} \mathbf{U}. \tag{5.64}$$

The transport parameters are kept fixed during a single ADI step and evolved only in between two steps. Moreover, in each sub-step of ADI on $\mathbf{P}_2$, the update of the total energy due to magnetic field evolution (see the forth row of the right hand side of eq. (5.62)) is performed neglecting the effect of energy variation on the whole system. It is worth to note that the use of Lie splitting adds an additional splitting error (which is formally first order), but it is necessary in order to keep the resulting systems tridiagonal. However, considering that the problems are not strongly coupled, we believe the additional error to be fairly negligible. A similar splitting scheme among the thermal and magnetic problems is performed also in the original version of PLUTO, when the super time stepping scheme is employed.

When PR is applied to the diffusive problem of our case we have:

$$\frac{\mathbf{U}' - \mathbf{U}^n}{\Delta t/2} + \widetilde{\mathbf{P}}_{jz}(\mathbf{U}', t^{n+1/2}) + \widetilde{\mathbf{P}}_{jr}(\mathbf{U}^n, t^n) = \mathbf{0}, \tag{5.65}$$

$$\frac{\mathbf{U}'' - \mathbf{U}'}{\Delta t/2} + \widetilde{\mathbf{P}}_{jz}(\mathbf{U}', t^{n+1/2}) + \widetilde{\mathbf{P}}_{jr}(\mathbf{U}'', t^{n+1}) = \mathbf{0}, \tag{5.66}$$

where we defined $\mathbf{U}^n = \mathbf{U}(t^n)$, $\mathbf{U}''$ is an approximation of $\mathbf{U}^n e^{\mathbf{P}_j \Delta t}$, $\widetilde{\mathbf{P}}_{jr}$ is a discretization of operator $\mathbf{P}_j$ that contains all the derivatives with respect to r and $\widetilde{\mathbf{P}}_{jz}$ a discretization of operator $\mathbf{P}_j$ that contains the derivatives with respect to z. Obviously, one is free to exchange the roles of $\widetilde{\mathbf{P}}_{jr}$ and $\widetilde{\mathbf{P}}_{jz}$, and exchange them in order to search for the setting that provide the best stability and accuracy.

The application of DR scheme to our diffusive problem reads:

$$\frac{\mathbf{U}' - \mathbf{U}^n}{\Delta t} + \widetilde{\mathbf{P}}_{jz}(\mathbf{U}', t^{n+1}) + \widetilde{\mathbf{P}}_{jr}(\mathbf{U}^n, t^n) = \mathbf{0}, \tag{5.67}$$

$$\frac{\mathbf{U}'' - \mathbf{U}^n}{\Delta t} + \widetilde{\mathbf{P}}_{jz}(\mathbf{U}', t^{n+1}) + \widetilde{\mathbf{P}}_{jr}(\mathbf{U}'', t^{n+1}) = \mathbf{0}. \tag{5.68}$$

As before, one may exchange the roles of $\widetilde{\mathbf{P}}_{jr}$ and $\widetilde{\mathbf{P}}_{jz}$ in order to search for the setting that provide the best stability and accuracy, bearing in mind the suggestions found in literature.

We performed some numerical tests with the aim of comparing the performance of PR and DR variants on the problems studied in this thesis. It has been found that, both work excellently well when applied to a reduced version of the problem, consisting in a plasma that does not move in space (i.e. for the operator $\mathbf{P}$ alone). Nevertheless, when the plasma is free to move and the entire problem in studied with the combination of the hyperbolic solver and DR scheme, the system is stable if the global time step is kept at approximately 10^{-2} ns (much lower than the Courant-Friederich-Levy limit for explicit solution of advective problems) and the number, N, of ADI sub-cycles is higher than 100. Instead, if the PR variant is used a more costly sub-cycling is required, with $N \geq 500$. Thus, we decided to employ DR scheme throughout this work.

We note that what found is consistent with the in literature, that DR scheme is expected to be more robust than the PR. Moreover, the need for sub-cycling in both DR and PR is also not surprising, considering the non-linearity of the problem and considering that the ADI methods are combined with a hyperbolic solver by means of Strang splitting, and not used *as is*.

Chapter 6

Plasma discharge simulation

In this chapter we perform some capillary discharge simulations with both the aim of validating our computational model and exploring some first possibility for optimizing the operation of APL. First of all, in section 6.1 we compare the results of our simulations with the electron density measurements available in Ref. [53]. Then, in section 6.2 we try to replicate the experimental results of Ref. [106], where an APL was used to focus a high brightness electron beam, by simulating the same discharge and tracking an electron beam through the thus obtained magnetic field. Lastly, in section 6.3, we explore the effect of the width of the capillary section on the magnetic field quality, by simulating a discharge in two capillaries that differ only by the size of their diameters and by the intensity of the imposed current.

## 6.1 Comparison between simulations and electron density measurements

In this section we compare the electron density obtained from our simulations with the longitudinally and time resolved measurements available in Ref. [53, pp. 74-100]. We simulate the same capillaries and apply current profiles that mimic the measured ones. The capillaries studied have been already described in section 3.2. The first one, that here we call capillary (a), is $3\,cm$ long and the other one, capillary (b), is $1\,cm$ long. Both have a diameter of $500\,\mu m$ and are made by a conic sapphire tube, inserted into a printed plastic holder. Capillary (a) has two inlets, located at 1/4 and 3/4 of its length. Capillary (b) has one inlet, located at the center.

Two flat, holed copper electrodes are placed at the capillary extremities. We modeled them with $1\,mm$-thick perfectly conducting material placed at the capillary exits. Electrical discharges in the $1\,cm$ capillary were driven using the $7.2\,nF$-$36.5\,\Omega$ electrical circuit described in section 3.2. A stable current time profile with duration of $1.5\,\mu s$ and peak value of $245\,A$ was measured. Instead, the discharges in the $3\,cm$ capillary were performed using the $2\,nF$-$100\,\Omega$ electrical circuit, also described in section 3.2. In this second case, stable current time profiles with duration of $1.5\,\mu s$ and peak value of $95\,A$ were obtained. The time profiles of the two currents are plotted in figs. 6.1 and 6.2, where they have been overlaid with the current imposed in our simulations.
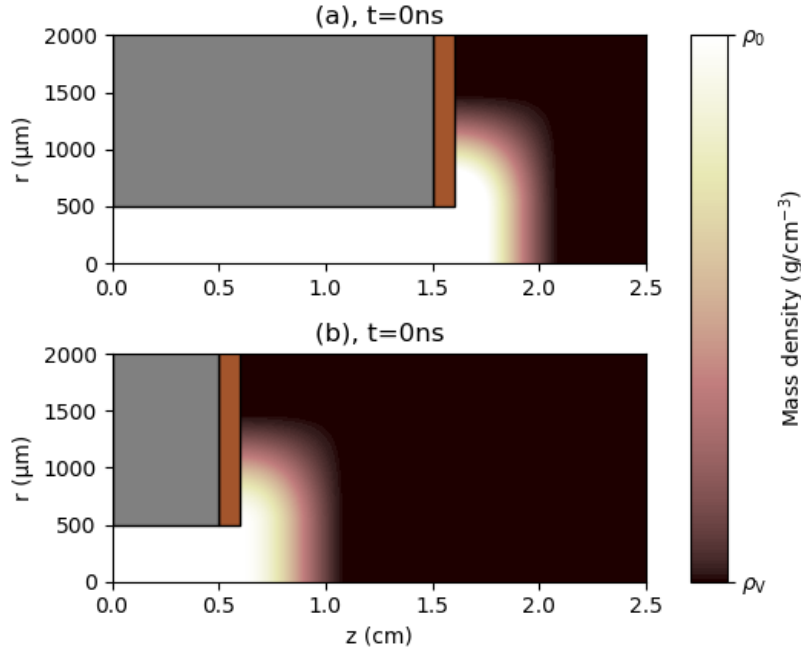
Unfortunately, no measurement of the neutral gas present in the capillary prior
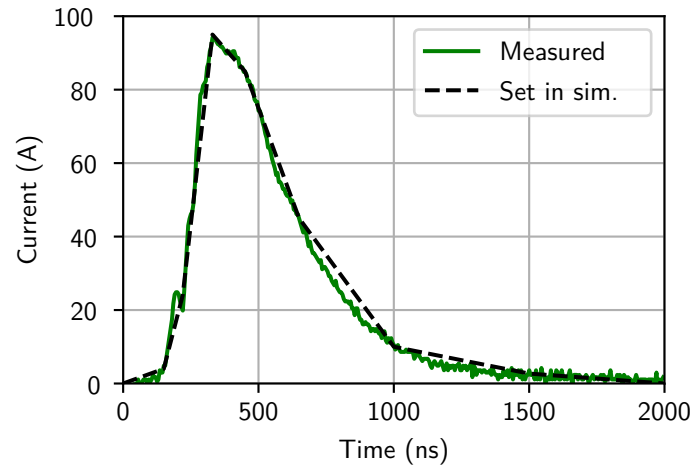
Figure 6.1. Current setting in simulation (black, dashed line), compared with the measured one (green, continuous line) (case (a)).
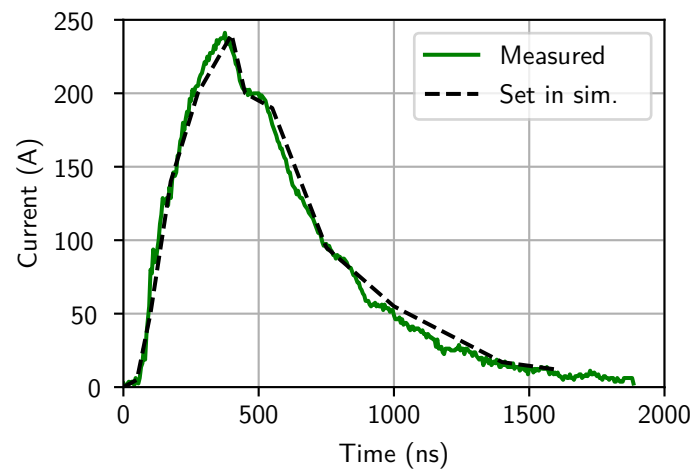
Figure 6.2. Current setting in simulation (black, dashed line), compared with the one measured (green, continuous line) (case b).

Figure 6.3. Mass density at the beginning of the simulation, for case (a) (top) and case (b) (bottom), for a generic value ρ_0 of the mass density filling the capillary and the surrounding vacuum.

to triggering the discharge is available at the time of writing. [1] Therefore, in our simulations we filled the capillaries with an initially uniform mass density, ρ_0. We will specify below the values of ρ_0 in each computation. Outside the capillary, the density drops smoothly and reaches a base value, $\rho_V \approx \rho_0/1000$, that models the vacuum region surrounding the plasma. Namely, the initial density distributions are described by:

$$z < L/2, r < R : \rho = \rho_0, \tag{6.1}$$

$$z > L/2, r < R : \rho = (\rho_0 - \rho_V)\cos^2\left[\frac{\pi}{2}\frac{(z - L/2)}{d_z}\right] + \rho_V,$$

$$z > L/2, r > R : \rho = (\rho_0 - \rho_V)\cos^2\left[\frac{\pi}{2}\frac{(z - L/2)}{d_z}\right]\cos^2\left[\frac{\pi}{2}\frac{(r - R)}{d_r}\right] + \rho_V,$$

where $d_z = 5\,\mathrm{mm}$ and $d_r = 1\,\mathrm{mm}$. The mass distributions for the two cases are plotted in fig. 6.3. We are aware that the choice of uniformly filling the capillaries represents a limitation to the accuracy of our results, but we are confident that a first order benchmarking of our model with experimental cases is still possible.

Furthermore, the gas is initialized at rest and at an initial temperature of $3400\,\mathrm{K}$ (further details on the initial and boundary conditions are available in section 5.2).

---

[1]The preliminary gas dynamics simulations mentioned in section 3.2 serve only to estimate the scale of the timings required for reaching the steady state in the neutral gas flow, but the numerical studies that have been performed on capillary filling gas dynamics are not mature enough to be used as initial conditions for discharge simulations.

We chose the values for ρ_0 consistently with the backing pressure that was set at the capillaries and based on considerations regarding the electron density measurement process, that we will outline below. The backing pressure was set at approximately $100\,\mathrm{mbar}$. Assuming ideal gas law is applicable for hydrogen in these conditions, this corresponds to a mass density of $8 \times 10^{-6}\,\mathrm{g\,cm^{-3}}$, for a gas temperature of $300\,\mathrm{K}$. Considering the length (tens of centimeters), the transverse size ($< 1\,\mathrm{cm}$) of the ducts feeding the inlets and also the presence of few shrinkages, we expect a severe pressure drop (by a factor $10 \div 50$) between the value at the capillary and the one set upstream. We estimate that realistic values for mass density filling the capillaries are of the order of $10^{-7}\,\mathrm{g\,cm^{-3}}$. Thus, we performed simulations with different initial mass densities looking for a condition best fitting the experimental data.

In addition, in order to properly compare the computed and measured data, some important considerations must be given. In Ref. [53] the electron density was obtained by observing the broadening of the H–beta line by Stark effect. For each timing and longitudinal position, the light coming from the full transverse section of the capillary was collected, with a camera gated for $100\,\mathrm{ns}$. In fact, as noted by Ref. [53] in agreement with a number of works [126, 118], in a capillary discharge the electron density may vary considerably over the radial position: between the axial and near wall values factors even grater than 2 are common. Nevertheless, the optical system employed for the measurements did not allow to resolve transverse positions along the capillary radius. It was necessary to consider the measurement as representative of a weighted average of the electron density over the capillary section. A rigorous estimation of the weighting factor was not performed in Ref. [53] and we do not attempt it either. However, we expect that it is monotonically growing with the electron density; we explain why in the following.

The H–beta line is due the electronic transitions $n = 4 \Rightarrow n = 2$ (n being the principal quantum number) occurring in the plasma. Its intensity is dependent only on the population density of the excited level, $n = 4$, which in turn depends (in LTE conditions) on the plasma temperature, density and composition. For the plasmas of our interest, the population density of level $n = 4$ is monotonically growing with the electron density [48]. Therefore the higher is the electron density in a certain region of plasma, the greater is the amount of photons at the H–beta wavelength emitted from that region. Thus the intensity and broadening of the H–beta spectral line is more dependent from regions where the electron density is higher, than it is from regions with lower electron density. Consequently, we treat the values of electron density provided by Ref. [53] as representative of a value in between the pure integral average and the maximum over the capillary section.

For each of the two experimental cases, (a) and (b), we plot the results for two choices of values for ρ_0. One is the case best matching the experimental data, when the maximum value of the computed electron density over the capillary section is considered. The other one is the best matching case when the average of the computed electron density over the capillary section is considered. The results for capillary (a) are plotted in fig. 6.4 whereas the results for capillary (b) are plotted in fig. 6.5

Regarding case (a), an initial mass density of $8 \times 10^{-7}\,\mathrm{g\,cm^{-3}}$ provides the best resemblance between our computations and the measurements, when we plot the
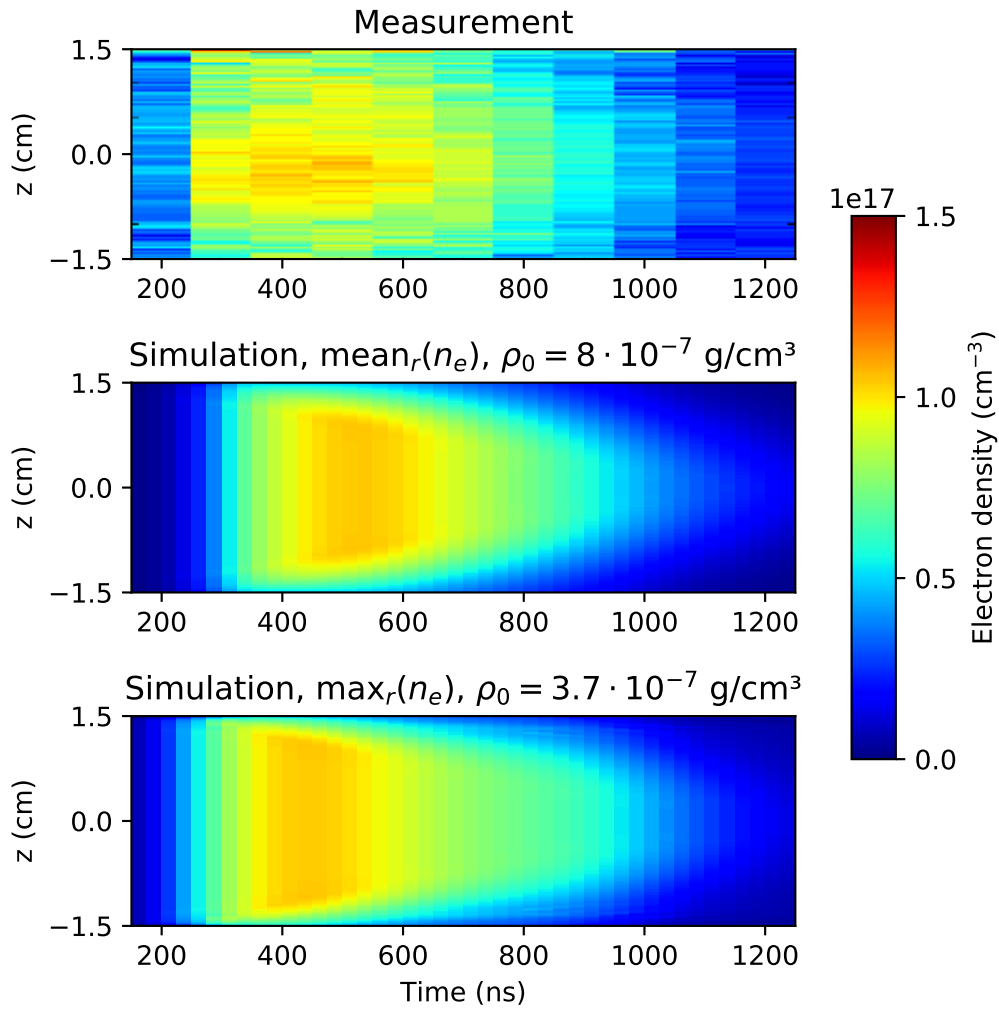
Figure 6.4. Comparison between measured [53] (first row) and simulated (second and third row) time evolution of longitudinal electron density, inside a 3 cm-long, 1 mm-diameter capillary during a discharge with 90 A peak current. In the second (third) row, the average (maximum value) of the electron density over the capillary section is plotted for each longitudinal position and timing.
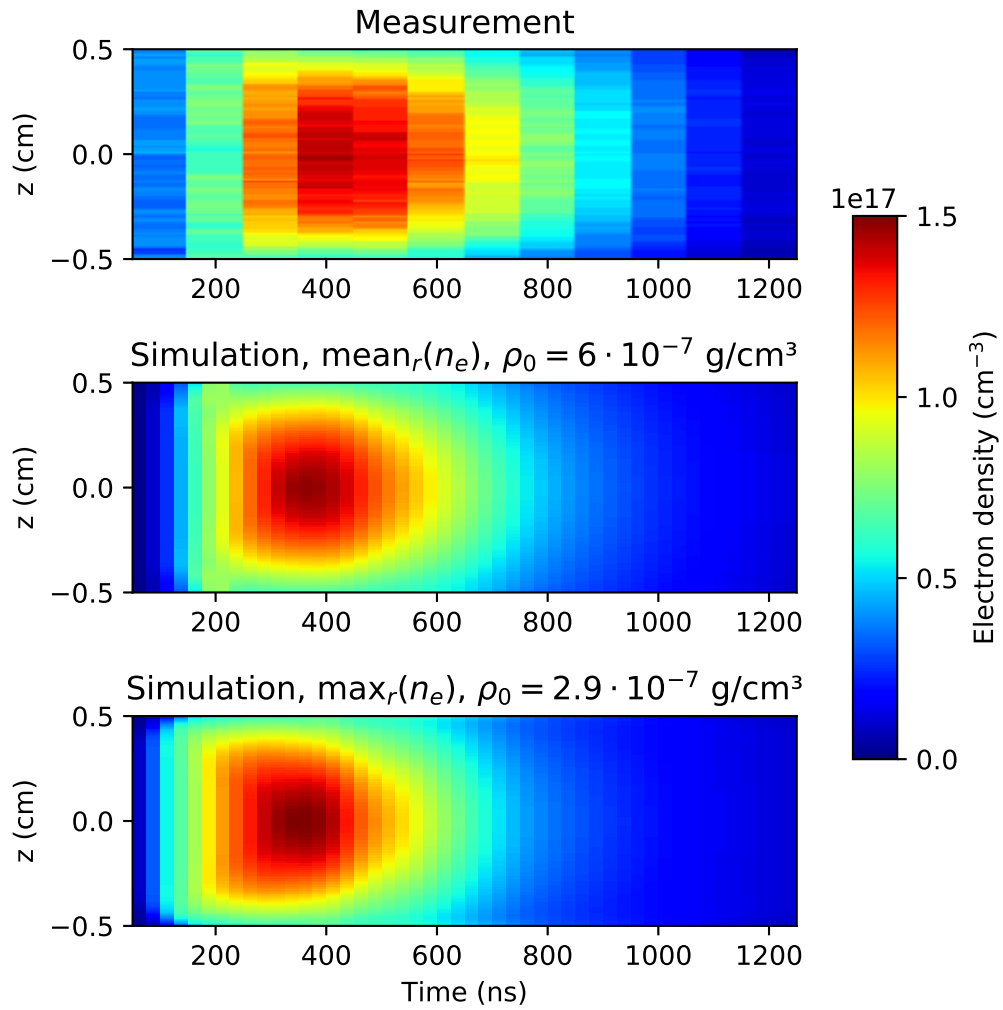
Figure 6.5. Comparison between measured [53] (first row) and simulated (second and third row) time evolution of longitudinal electron density, inside a 1 cm-long, 1 mm-diameter capillary during a discharge with 245 A peak current. In the second (third) row, the average (maximum value) of the electron density over the capillary section is plotted for each longitudinal position and timing.

average of the electron density over the capillary section. Instead, a mass density of $3.7 \times 10^{-7}\,\mathrm{g\,cm^{-3}}$ provides the best resemblance when we plot the maximum value of the electron density over the section. Note that the peak of the electron density value is reached approximately at $450\,\mathrm{ns}$ in the first case, and at $550\,\mathrm{ns}$ in the second case. The peak in the measured data is instead around $500\,\mathrm{ns}$, well in between the two computed cases. We consider the agreement between the measured and simulated distributions satisfactory.

For case (b), an initial mass density of $6 \times 10^{-7}\,\mathrm{g\,cm^{-3}}$ provides the best resemblance between our computations and the measurements, when we plot the average of the electron density over the capillary section. Instead, a mass density of $2.9 \times 10^{-7}\,\mathrm{g\,cm^{-3}}$ provides the best resemblance when we plot the maximum value of the electron density over the section. The time delay between the peaks of the computed electron density distributions is in this case negligible. Most notably, it can be seen that the computed and measured data are in good agreement for the first $400\,\mathrm{ns}$, but at later times the measured data accumulate a delay (around $100\,\mathrm{ns}$) with respect to the simulations.

We explain this difference with our choice of the initial distribution of the neutral hydrogen gas. In the experimental situation, the $1\,\mathrm{cm}$-long capillary has only one inlet, located at the center. Thus, it is reasonable to expect that the neutral gas is initially concentrated near the inlet (i.e. at the center) and its density drops approaching the extremities. Note that this distribution is very different from the one that we chose for our computations. When the discharge is triggered, the gas is heated up by the ohmic losses. The thermal pressure increases and pushes the gas that was concentrated at the capillary center towards the two extremities. It is reasonable to expect that this mass distributes in the whole capillary and, once ionized, provides additional electron density, delaying the quenching of the plasma.

We also expect that such effect does not occur in capillary (a), whose inlets are located at 1/4 and 3/4 of its length. Reasonably, a uniform pressure and mass density distribution is established between the two inlets before the electrical discharge takes place.

From the comparison just performed, we conclude that the electron density computed inside the capillary with our simulation model is realistic, especially for case (a), where the measured and simulated time evolution of the density are in good agreement. Instead, for case (b) we observed some discrepancies. One possibility to explain them is that our choice of the initial neutral gas density distribution may be too far from the experimental situation. It is clear that additional knowledge on the initial gas distribution is required for the discharge simulations to provide reliable time evolutions of the electron density distribution. Such knowledge can be provided by detailed neutral gas measurements, possibly coupled with numerical simulations of gas dynamics.

6.2 Focusing of a high brightness electron beam with a 90A peak current APL

In Ref.[106] a high brightness electron beam was focused by means of an APL made by an electrical discharge inside a hydrogen-filled capillary, with peak current of
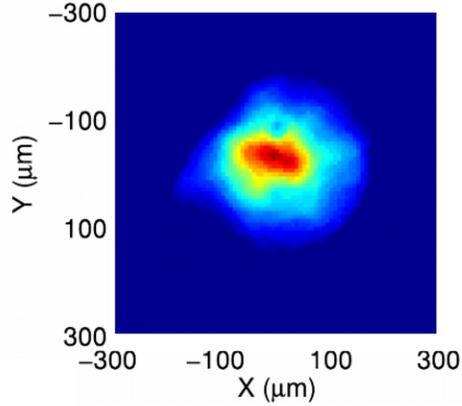
Figure 6.6. Transverse spot of the beam observed by means of a Ce:YAG screen located 20 cm downstream the capillary. Reprinted from Ref. [106]

approximately 90 A. In this section we aim at reproducing those results. The final scope is primarily to validate our computational model and secondly to provide additional insight into the physics of the discharge involved.

6.2.1 Experiment and simulation setup

In Ref. [106], an APL consisting in a capillary discharge was used to focus a single bunch electron beam provided by the SPARC photo-injector. Such a bunch has a charge of 50 pC and an energy of 126 MeV($\gamma \approx 246$), with an rms energy spread of 50 keV. Its normalized emittance is (1.0 ± 0.2) µm and its rms duration is 1.1 ps. At the capillary entrance the minimum rms transverse spot recorded was $\sigma_{x,y} = (130 \pm 10)$ µm; this is also the spot size used for the tracking studies present in Ref. [106], thus we will also use this value for our computations. In addition, as beam density distribution we will consider a cylindrically symmetric one, with a Gaussian radial profile upstream the capillary. This assumption seems reasonable, considering the transverse beam density map recorded downstream the capillary, when the discharge is turned off, as we reported in fig. 6.6.

The plasma current used for focusing the electron beam was obtaining by feeding the electrodes of a hydrogen-filled capillary with the 2 nF-100 Ω electrical circuit described in section 3.2. The capillary used is 3 cm long and it has a radius of 500 µm. The current time profile is the same as the one already plotted in fig. 6.1 of previous section. Note that, in order to simplify the presentation, we chose to refer the time to the start of the discharge, instead of referring it to the instant when the current reaches the peak value (thereby we take a convention that is different from the one of Ref. [106]).

Our approach is to simulate the discharge and track the electron beam through the resulting magnetic field. The current imposed in our simulation is the one plotted in fig. 6.1. Initially, we fill the capillary with a uniform a mass density of 4.5×10^{-7} g cm^{-3}, that we consider realistic, based on the discussion of the previous section. The mass density filling the capillary is matched smoothly to the surrounding vacuum region, modeled with a mass density 1000 times smaller. The smoothing is
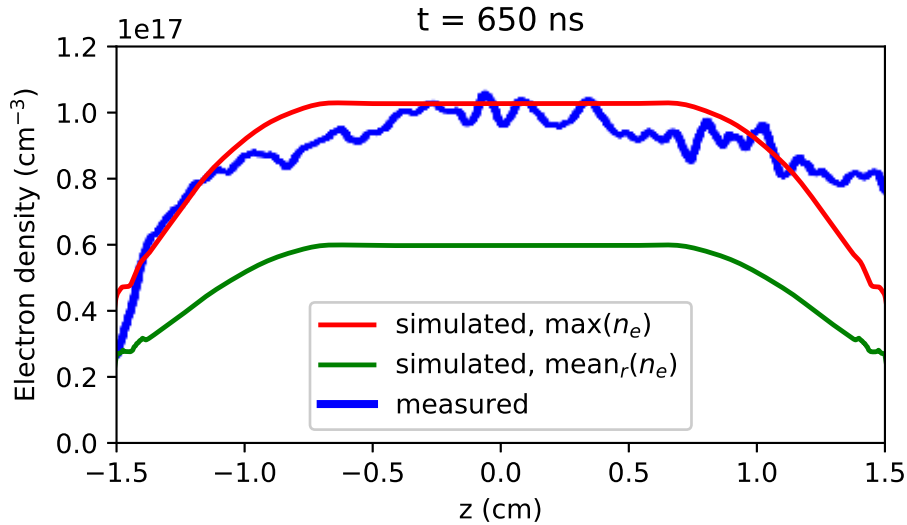
Figure 6.7. Longitudinal electron density profile inside the capillary, obtained from the measurement (blue line), and from the simulation, considering the average over the transverse section (green line) and the maximum over the transverse section (red line)

done as in eq. (6.1). In the experimental case the backing pressure was set to a few hundreds millibar. All the other initial and boundary conditions are in agreement with what explained in section 5.2.

6.2.2   Results

Regarding the electron density, our results at 650 ns are in good agreement with the measured profile that is plotted in Ref. [106] for that timing. In fig. 6.7 we overlaid the measured and computed profiles. The measurement was performed observing the Stark broadening of Balmer–beta line in the assumption of uniform electron density across the capillary section. Thus, for the reasons explained in section 6.1, we plotted both the average and maximum value of the computed electron density over the section.

In order to provide a full view of the focusing capabilities of the simulated capillary, we plot in fig. 6.8 the time evolution of the longitudinal average of the focusing gradient:

$$\langle g \rangle_z(r) \doteq \frac{\int_{-\infty}^{+\infty} B(r,z)\,\mathrm{d}z}{rL}, \tag{6.2}$$

In the same figure we also plot a colored map representing the time evolution of the radial variation of the averaged focusing gradient with respect to its value on the capillary axis. Note that the absolute variation in focusing gradient is directly responsible for beam emittance growth (being directly proportional to the difference in focusing strength).

We tracked the beam electrons through the magnetic field obtained in our simulation, using a leapfrog algorithm. We neglected the space charge effects and the wakefield generated inside the plasma (passive focusing). For the beam that we
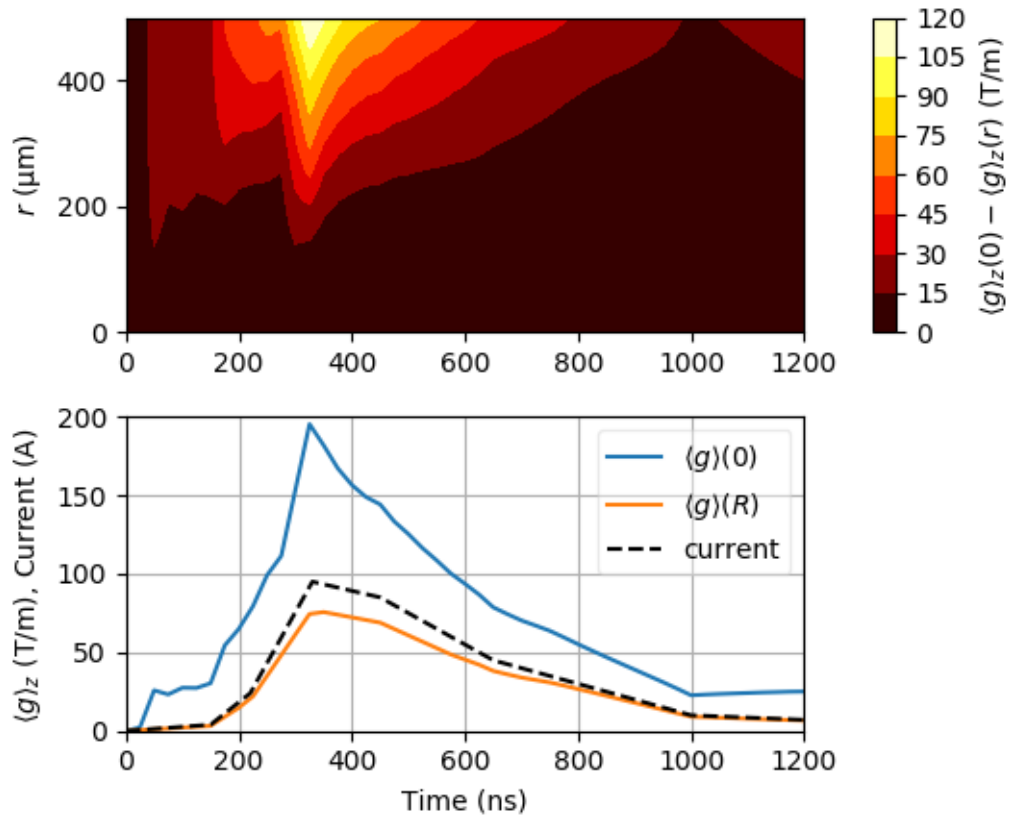
Figure 6.8. Time evolution of the averaged focusing gradient at $r = 0$ (bottom plot, blue line) and at the capillary wall ($r = R$, orange line, bottom plot). The time evolution of the current has also been plotted for completeness (dotted line, bottom plot). In the top plot, the colored map represents the time evolution of the variation of the averaged focusing gradient with respect to the axial value of the averaged focusing gradient.
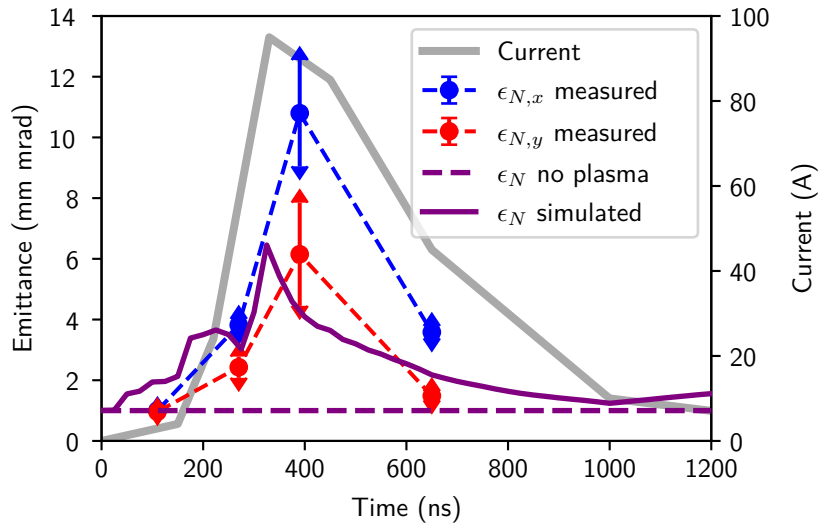
Figure 6.9. Computed (purple) and measured[106] (red, dashed line and blue dashed line) normalized rms emittance downstream the capillary, overlaid with the current time profile (gray).

considered, the space charge is of minor importance because its energy is much higher than what required by the threshold given by eq. (1.16): $\gamma_{tr} \approx 9 \ll 246$. Regarding the passive focusing, we are aware that it is not negligible for the case considered, however we assume that its importance is marginal. Indeed, in Ref. [106] the interaction between the SPARC beam and the APL plasma was simulated using the hybrid kinetic-fluid code Architect [89]: the emittance growth resulting solely from the passive focusing was of the order of 0.1 mm mrad and the spot reduction inside the APL was around 2 μm (when the beam is injected 650 ns from the beginning of the discharge). The emittance growth due to the combined effect of the azimuthal magnetic field and plasma wakefield was estimated to be more than thirty times greater and the spot reduction in the APL was five times higher [106, fig. 6].

We computed the normalized rms emittance downstream the lens and we reported the results in fig. 6.9, together with the measured values from Ref. [106]. We also computed the rms spot 20 cm downstream the lens, corresponding to the location in the line where a Ce:YAG screen is installed. The results are plotted in fig. 6.10, together with the measured values. Note that the measured data are not symmetric in the x and y transverse directions. This is most likely due to any of the two following reasons. One possibility is that the x and y profiles of the beam have a different shape upstream the capillary, regardless of the fact that they have the same rms size[2]. The other one is the presence of the inlets in the real capillary which brake the geometrical symmetry of the insulating walls, and possibly also the one of the focusing magnetic field.

However, except for the point ad 100 ns, the computed emittance is within the error bars of the measured data. Shortly below we will comment on the discrepancy

---

[2]This would obviously imply that, among the x and y profiles, at least one is not Gaussian
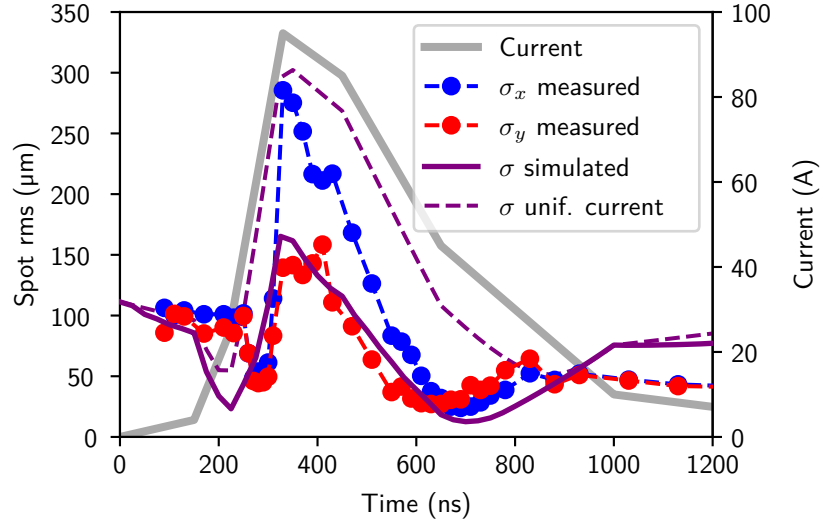
**Figure 6.10.** Computed (purple) from discharge simulation results and measured[106] (red, dashed line and blue dashed line) rms spot 20 cm downstream the capillary, overlaid with the current time profile (gray). Each of the measured spot sizes has an error of the order of few microns. The spot size in the approximation of uniform current density is also plotted, with a purple, dashed line.

between the measured and simulated emittance variation at 100 ns. Regarding the spot size, the measured and computed values are in fair agreement. The first computed local minimum is approximately at 200 ns from the beginning of the discharge: 100 ns before than the measured one. The other computed local minimum is at 700 ns, delayed of approximately 50 ns with respect to the one measured in y direction but almost aligned with the one measured in x direction. Regarding the time location of the first measured minimum, we note that the drop in spot size is quite abrupt, since up to a timing of 250 ns the beam was not focused at all, even thought the current already reached a value higher than 30 A. We interpret this as an indication that the current flows mainly near the capillary walls (up to this timing) and thus the magnetic field sampled by the beam particles is extremely low. If this were not the case, the beam would be focused in way similar to what happens in the descending part of the current profile for the same current intensity. This would also explain why the emittance is fully conserved at 100 ns. Clearly, for the present case the first 250 ns are modeled with little accuracy by our simulation. A possible reason is the choice of the initial mass density distribution or a not satisfying modeling of thermal conduction at low temperatures. Regarding the second minimum, we note that even though there is a discrepancy with respect to the measured value, the spot computed from the simulated magnetic field is much closer than it is the one computed in the approximation of uniform current density; we are therefore satisfied with the agreement between simulated and measured spot.

In addition, we compare the magnetic field that we obtained from our simulation with the one experimentally inferred in Ref. [106], for a timing of 650 ns, corresponding to a current of 45 A. Thus, we plot in fig. 6.11 the longitudinal average of the
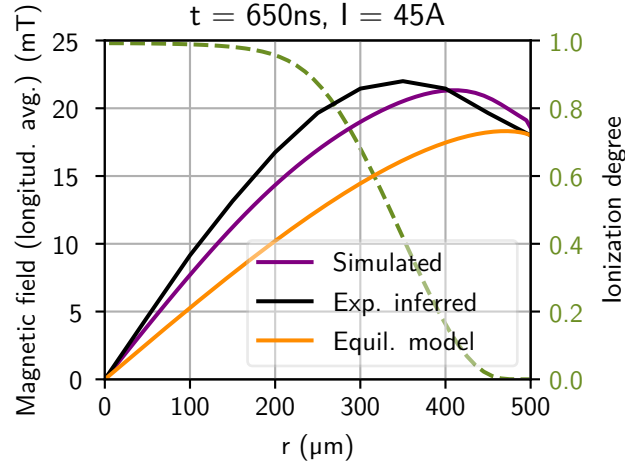
Figure 6.11. Radial profiles of magnetic field longitudinally averaged over the length of the capillary, computed with PLUTO (at 650 ns, corresponding to a current of 45 A) (purple), experimentally inferred in Ref. [106] (same timing) (black), and according to the 1-D, thermal equilibrium model [19](orange). The radial profile of the ionization degree (green, dashed line) is plotted at $z = 0$.

computed magnetic field, together with the field experimentally inferred in Ref. [106], and with the one obtained with the equilibrium model described in section 2.2.1. As longitudinal average of the magnetic field, we refer to the quantity

$$\langle B \rangle_z(r) \doteq \frac{\int_{-\infty}^{+\infty} B(r,z)\,\mathrm{d}z}{L}, \tag{6.3}$$

where L is the capillary length; this definition takes into account also the fringe magnetic field, that may extend outside of the capillary for a certain length. The inferred and computed profiles are in fair agreement (even though some discrepancies are evident). Instead, the field obtained from the equilibrium model highly differs from both the computed and measured ones. This is clearly related the fact that the equilibrium model relies on the hypothesis of full ionization of the plasma, which is not satisfied in this case.

6.3 Effect of diameter variation

According to what found by a number of authors [113, 106, 131] and in agreement with the thermal equilibrium solution (section 2.2.1) of capillary discharges, the dependence of the azimuthal magnetic field on the radial position is approximately linear in the vicinity of the capillary axis and bends approaching the capillary wall, due to the wall cooling effect. One may speculate that enlarging the capillary diameter would be useful for building a lens that has better magnetic field quality, i.e. a field that exhibits a satisfyingly linear transverse profile where the beam is supposed to pass.

A drawback of this strategy is that higher electrical currents are needed, indeed the current required to obtain a certain focusing strength grows quadratically with
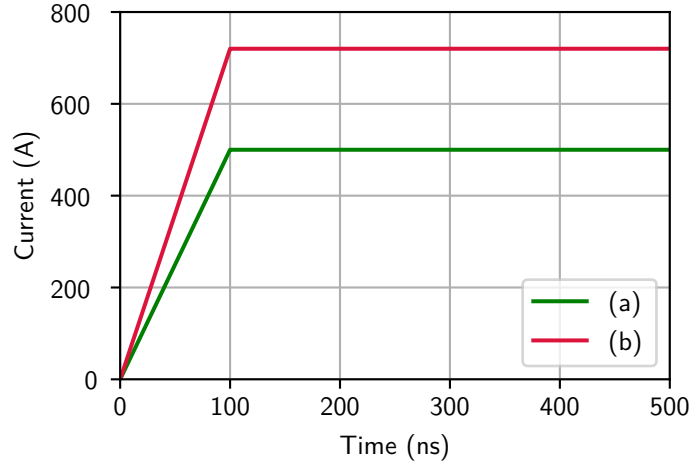
Figure 6.12. Time profiles of the electrical current imposed in capillary (a) (green) and (b) (red).

the capillary radius (assuming uniform current density distribution). In addition, also the amount of gas to be inflated in the capillary grows quadratically with the capillary radius, if the mass density inside the discharge region is kept fixed. In principle, the presence of more mass and a wider capillary section may translate in the ejection of more plasma from the capillary extremities, with consequent generation of longitudinally extended plasma regions where the beam may excite wakes capable of ruining its quality. Moreover, the amount of mass inflated in the capillary may spoil the vacuum quality, whose requirements are instead quite stringent in a particle accelerator.

6.3.1   Discharge in capillaries with different radii

We address the questions above by simulating two discharges that are performed in capillaries with different diameters and current intensities but are otherwise identical. We compare a case, (a), where the capillary radius, is $R_a = 500\,\mu m$ with another, (b), where the radius is 20 % greater, i.e. $R_b = 0.6\,\mu m$. The currents imposed have a flat-top profile, with a rise time of 100 ns. The current of case (a) has a top value of 500 A whereas for case (b) the top value is scaled according to the squared ratio of the diameters, i.e. 720 A. The two profiles are overlaid in fig. 6.12. The current form that has been chosen is realistic considering the technology available nowadays: an APL with a similar current profile was experimentally studied by Ref. [113][3].

Each one of the capillaries studied has a total length $L = 1.2\,cm$, which is composed by a 1 cm-long electrically insulating wall and two 1 mm-long electrodes. The geometry of the computational domain is consistent with what described in section 5.2.

The capillaries are filled with an initial mass density $\rho_0 = 2.5 \times 10^{-7}\,g\,cm^{-3}$. At room temperature, this amount of neutral gas would correspond to a uniform

---

[3]Currents of 188 A-740 A were reached after a 100 ns ramp, and sustained for 240 ns
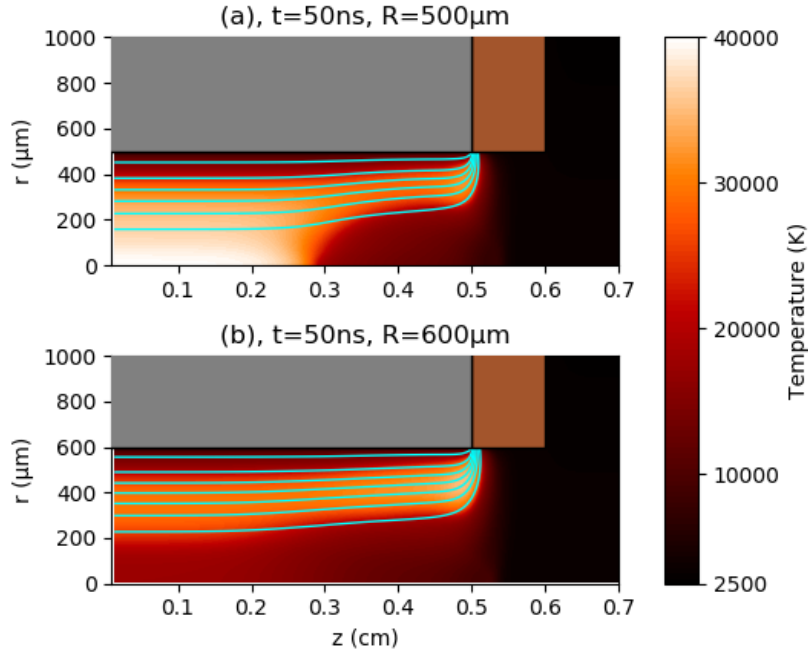
Figure 6.13. Temperature map in capillary (a) (top) and in capillary (b) (bottom) at 50 ns from the beginning of the discharge, with some current density streamlines.

filling pressure of 2 mbar, a value that is considered realistic. Note, however, that we initialize the gas at a temperature of 3400 K in order to be consistent with the choice of skipping the hydrogen dissociation process and to provide an initial fictitious ionization degree. The density outside the capillary drops smoothly until it reaches the value of $\rho_V = 2.5 \times 10^{-10}\,\text{g cm}^{-3}$, that models the vacuum region surrounding the plasma. The matching with the vacuum environment is done as described by eq. (6.1).

6.3.2 Results

At the beginning of the discharge the plasma resistivity is uniform and the current density lines follow the minimal path between the two electrodes passing nearby the capillary walls and not concentrating at the capillary axis. Therefore, the heat generated by the ohmic losses is deposited at first in an annular channel between the capillary wall and the axis. This is clearly visible in fig. 6.13, where few streamlines of the current density are plotted over the temperature map at 50 ns after the discharge began. The heating of this region of the plasma fosters the concentration of current at that location. However, after approximately 100 ns-150 ns this behavior comes to an end, since the heat necessarily diffuses towards the capillary axis. This evolution can be seen in fig. 6.14, where we plotted the radial and longitudinal temperature profiles in the two capillaries at certain time instants. Note that this initial transient lasts more (and is more evident), for the case (b). It seems reasonable that this is related to the fact that in this case the heat diffusion process has to cover a
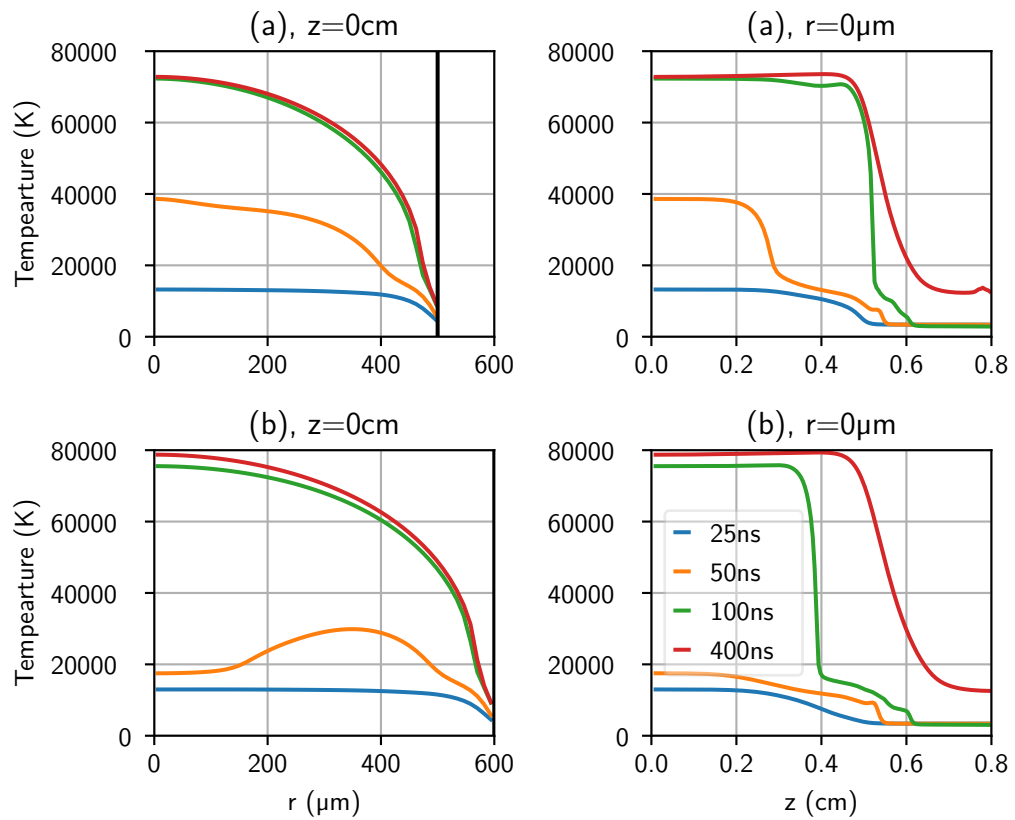
Figure 6.14. Radial (at $z = 0$) and longitudinal (on axis, $r = 0$) temperature profiles in capillary (a) (top) and (b) (bottom) for various timing from the beginning of the discharge.
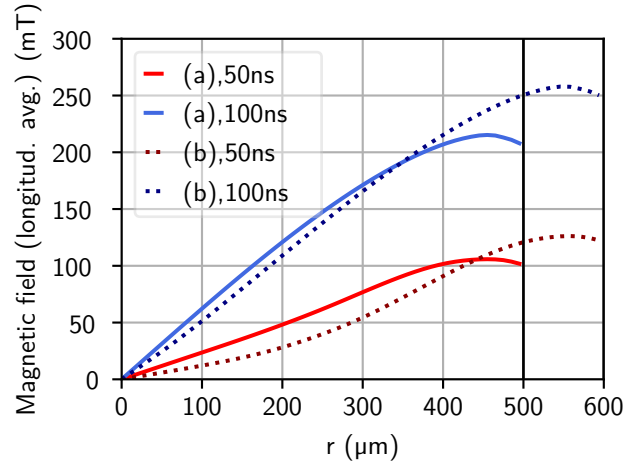
Figure 6.15. Longitudinal average of the magnetic fields in capillary (a) (continuous lines) and in capillary (b) (dotted lines), at 50 ns(red) and at 100 ns(blue) from the beginning of the discharge.

longer path to reach the capillary axis. [4] Once the on-axis plasma is hot enough with respect to the near wall region, the current density concentrates on the low resistivity channel at that location. At this point, all the heat generated by ohmic losses either flows towards the electrically insulating walls or exits from the capillary following the mass flow at the two extremities. Thus the temperature on the capillary axis approaches a constant value. Eventually, the equilibrium condition described in section 2.2.1 is established.

In fig. 6.15, the transverse profile of the longitudinal average of the magnetic field is plotted, for timings of 50 ns and 100 ns. During the thermal transient (line at 50 ns of fig. 6.15), the magnetic field has a convex profile in the vicinity of the capillary axis, due to the distribution of the current density explained above. Such a profile, more evident for case (b), is clearly not satisfying for active plasma lensing purposes. Furthermore, we plotted the profiles of the averaged magnetic fields for the two capillaries at 150 ns in fig. 6.16. Clearly, when the transverse thermal equilibrium condition is established, the profile of the longitudinally averaged magnetic field approaches the one foreseen by the equilibrium model described in section 2.2.1. The magnetic field profiles in the two cases have the similar and almost perfectly superimposed shapes, up to $r = 300 \, \mu m$. This superposition is an obvious direct consequence of the choice of scaling the two currents according to the ratio of the areas of the transverse capillary sections. As expected, capillary (b) has a field that is closer to a linear case than it is for capillary (a). One might wonder whether this provides significant improvement in the focusing capabilities of the APL. Hence, we tracked an electron beam through the fields obtained in the two cases and computed the emittance downstream the two capillaries. In order to explore a realistic situation, we employed an electron beam with the same specifications than the one we used

---

[4]In a diffusive process, the typical time it takes for energy to be transported over a certain distance grows quadratically with the distance itself.
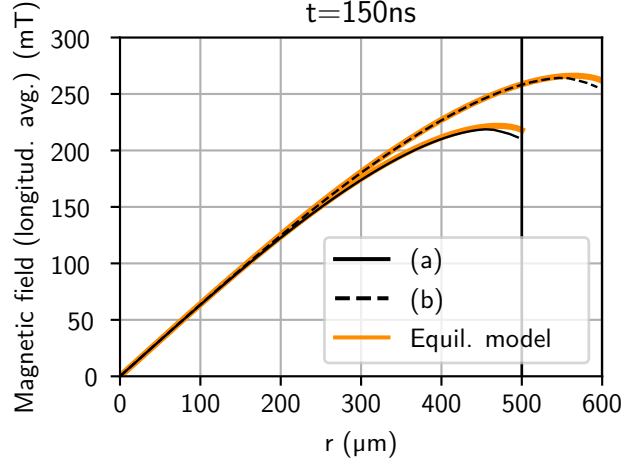
Figure 6.16. Longitudinal average of the magnetic fields in capillary (a) (continuous line) and in capillary (b) (dashed line), at 150 ns from the beginning of the discharge. In addition, the fields computed with the equilibrium model [19] (orange) have been uniformly scaled and overlaid to the two simulated profiles.

in section 6.2 (Gaussian transverse profile, $\epsilon_N = 1\,\text{mm mrad}$, $\sigma = 130\,\mu\text{m}$, $\gamma = 246$). The results of the tracking are plotted in fig. 6.17. For the first 100 ns from the beginning of the discharge, the emittance increase for case (b) is greater than for case (b). This can be explained by watching at fig. 6.15. At the initial timings the concentration of current density near the capillary walls is more intense in case (b) than it is in case (a), due to its wider transverse section. This leads to convex magnetic field profiles, and consequent stronger aberrations for case (b). Then, when the transverse thermal equilibrium is established (from 150 ns on), case (b) provides a magnetic field with a higher degree of linearity and thus performs better with respect to beam emittance growth. We see that when the beam passes through the APL (b) its emittance grows from 1 mm mrad to 2.2 mm mrad, instead in APL (a) it grows to twice as much, i.e. 3.4 mm mrad.

Another important aspect to evaluate is the electron density that develops inside the plasma. In fact, depending on the electron density that is present in the plasma, the wakes excited by the beam (passive plasma lensing) may have a significant detrimental effect on its quality [90]. In order to check for the differences, in terms of electron density between case (a) and (b), we plotted the axial profiles of electron density for different timing, for both cases, in fig. 6.18. Also, for the sake of completeness, we plot the full electron density distribution at 400 ns, i.e. when the two axial distributions exhibit more differences. The profiles in the two cases tend to differ more at later timings (400 ns), but no other notable differences can be found. This can be an indication that the slight enlargement of the capillary radius does not produce significant increase in the ejected electron density. Nevertheless, the amount of mass and electron density that exits the capillary highly depends on the mass that was initially contained inside. It is clear that in order to perform a more reliable comparison, realistic distributions of the neutral gas (i.e. coming from a
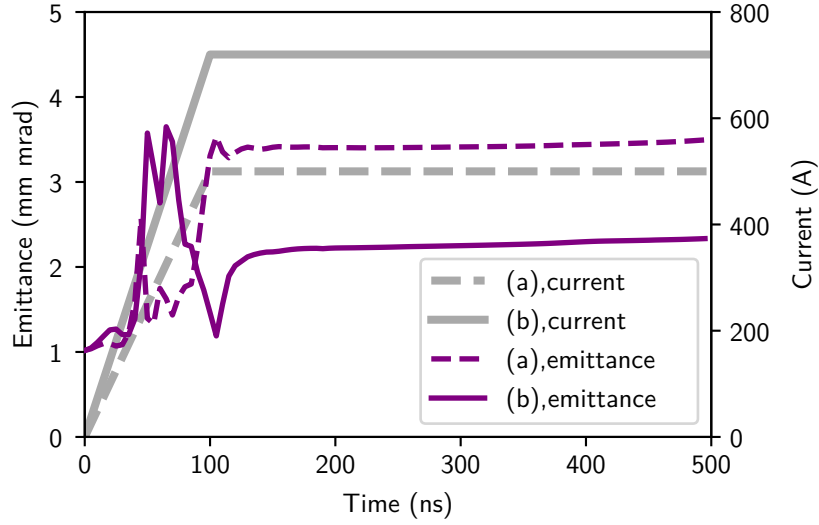
Figure 6.17. Computed normalized rms emittance for a beam passing through capillary (a) (dashed purple line) and capillary (b) (continuous purple line) for various delays with respect to the beginning of the electrical discharge. The current flowing in capillary (a) (capillary (b)) is plotted in gray, with a dashed (continuous) line.

measurement or from a simulation) are required. In addition, note that one expects the distributions to vary between capillaries with different aspect ratios (with no variation in the other settings); nevertheless, due to our lack of knowledge in regard, we employed the same initial distributions for the two cases. Lastly, in order to estimate the effect of the passive focusing on the beam quality, plasma wakefield simulations (with a particle-in-cell or hybrid kinetic-fluid approach) including the beam evolution consistently with the wakes generated are required. Such simulations should take into account the evolution of the beam consistently with the wakefield generated and including the radial and longitudinal modulation of the electron density distribution. Considering that we lack of a highly reliable initial condition for the mass density distribution for our capillary discharge simulations, also the reliability of the electron density map obtained is questionable. Thus, we do not perform any plasma wakefield simulation in the present work, but we plan to do them in the next future.

6.4 Discussion

In this chapter, we provided an initial validation of our numerical model and we performed some studies aimed at providing some additional understanding of the capillary discharge physics. We performed the validation by means of comparison with experimental results, that are related to measurements of the plasma electron density and to the beam focusing effects due to active plasma lensing. Then we studied two realistic discharges (not implemented in reality), in order to explore the effect of the capillary diameter variation.

We found that the measured and computed electron density distributions are
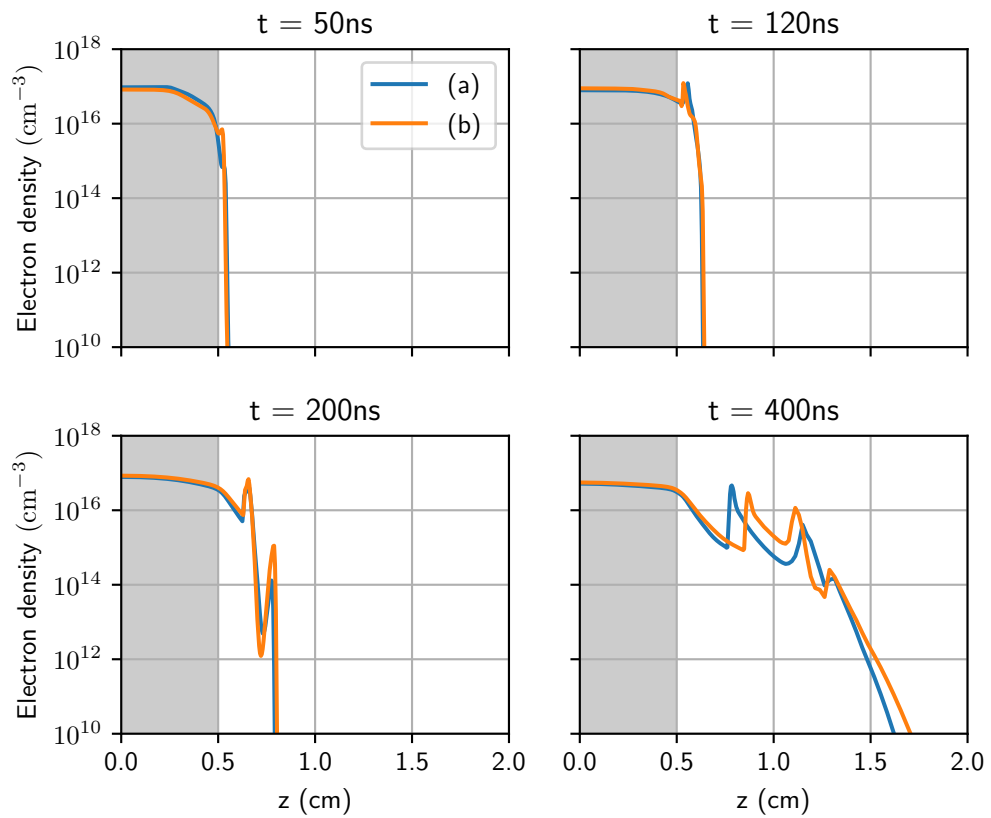
Figure 6.18. Axial electron density profiles at various timings from the beginning of the discharge, for case (a) (blue) and for case (b) (orange). Darkened regions correspond to locations inside the capillary.
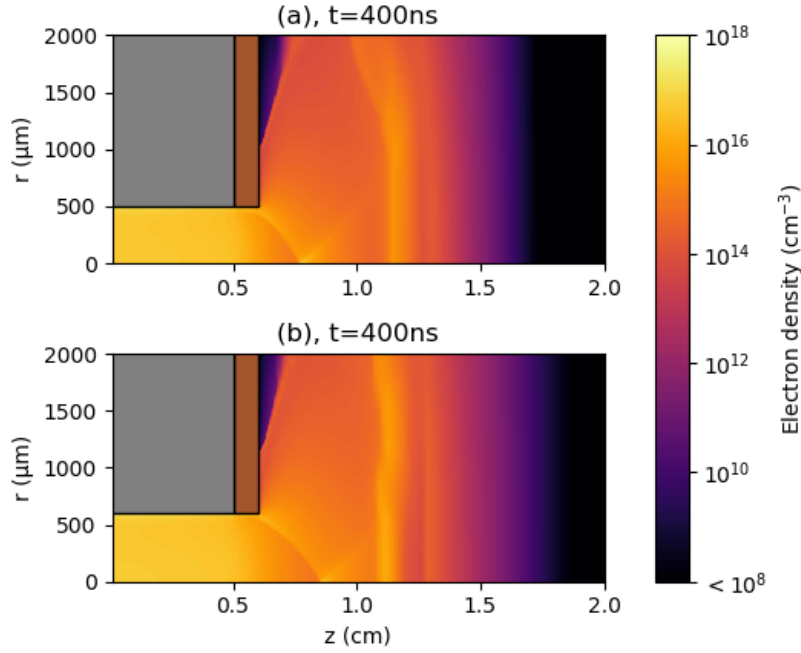
Figure 6.19. Electron density map at 400 ns from the beginning of the discharge, for case (a) (top), and case (b) (bottom).

substantially in agreement, even though some important differences are evident. For the case of a discharge with a 90 A peak current in a 3 cm-long capillary, the measured and computed electron density are in good agreement. For the case of a discharge with a 245 A peak current in a 1 cm-long capillary, the measured and computed electron density exhibit a time shift of approximately 100 ns. Our hypothesis is that this discrepancy is due to an unrealistic choice of initial neutral density distribution inside the capillary.

We also reproduced the experimental results of Ref. [106], where a 90 A-peak current discharge in a 3 cm-long capillary was used to focus a high brightness electron beam. We tracked the beam particles through the magnetic field obtained from our simulation and computed the transverse spot size and emittance downstream the capillary. Our results are in good agreement with the measurements. The main difference is that from our computations we would expect an important focusing effect at 200 ns, almost 100 ns earlier than what observed experimentally. Possible explanations are related to the choice of the initial mass density distribution, or to a not satisfying modeling of thermal conduction at low temperatures. We provided also a full picture of the focusing capabilities of such a discharge, by plotting the longitudinal average of the focusing gradient at each time step.

Lastly, we studied two APLs that differ by their diameter and have currents that are scaled accordingly, in order to provide the same focusing strength. The focusing capabilities of the two lenses have been tested by tracking a realistic high brightness electron beam through the computed magnetic fields. For this beam, we found that when the diameter is increased by 20 % the emittance growth is halved with respect

to the narrower diameter case. Furthermore, between the two cases we did not notice great differences in the electron density that is present on the plasma ejected at the capillary open extremities. However, realistic initial mass density distributions (not available at the time of writing) are necessary to perform accurate comparisons.

Chapter 7

Conclusion

In this work, we discussed the modeling and simulation of active plasma lenses, with special focus on the study of capillary discharges as focusing elements for high brightness electron beams. Indeed, high brightness electron beams are of critical importance for a number of technological as well as scientific applications, and also for the development of novel acceleration techniques involving, but not limited to, the excitation of wake fields inside plasmas.

In chapter 1 we discussed the part of the theory of charged particle beams that we used in this thesis; we also outlined the main aspects of the interaction of charged particle beams with plasmas.

In chapter 2, the working principle of APLs, i.e. the focusing of a charged particle beam by means of an azimuthal magnetic field generated by a current density propagating coaxially with the beam, has been explained in detail. The interest in APLs is mainly motivated by the high focusing gradients attainable $(\mathrm{kT\,m^{-1}})$, by their compactness (length in the cm range) as well as by the fact that their focusing strength is symmetric in the transverse planes but scales better (like $1/\gamma$) than the other commonly used symmetric devices (the solenoids, where it scales like $1/\gamma^2$). We also described the main issues that involve the APLs. They are the aberrations that are present when the magnetic field has a non linear dependence on the transverse position; when the electron beam passing inside the lens generates wake fields capable of spoiling its quality; and also when the scattering of the electron beam with the plasma ions and heavy particles becomes important. We also outlined the experimental progresses that have been obtained recently by different research groups.

In chapter 3, we briefly described the facility where this work was carried out, SPARC_LAB, where also experimental research related to the applications of capillary discharges for beam and laser physics studies is undergoing. At SPARC_LAB, experimental results have also been obtained, on the focusing of high brightness beams by means of hydrogen filled capillary discharges.

In chapter 4, we outlined the main points that lead to the derivation of the magneto-hydrodynamic model that we used in this work to simulate hydrogen discharges in capillaries: resistive MHD equations are used, including thermal conduction, with the assumption of local thermodynamic approximation has been taken.

In chapter 5, we described how we solved the MHD equations. The capillary that we studied are cylindrical, thus we modeled them inside an axially symmetric domain. We computed the plasma electrical resistivity and thermal conductivity with the Chapman-Enskog method, that takes into account the partial ionization of the plasma. We solved our system of equations with the open source code PLUTO. In order to overcome the severe time step limitations related to explicit (or super time-stepping) advancement of the parabolic terms related to thermal conduction and magnetic field diffusion, we implemented alternating direction implicit methods (Duglas-Rachford and Peaceman-Rachford schemes).

In chapter 6, we compared the results of our simulations with the electron density measurements performed by Ref. [53]. The results are substantially in agreement with each other. We speculate that the moderate differences that we found are related to the choice of the initial neutral gas filling the capillary. Due to unavailability of measurements of the initial neutral gas distribution, we assumed an initially uniformly filled capillary. We explained that this choice may generate inaccuracies in the description of the plasma dynamics. We also satisfyingly reproduced the results of Ref. [106], where an APL was used for focusing a high brightness electron beam. We did it by simulating the capillary discharge and then we tracked an electron beam trough the computed magnetic field. We refer the little discrepancies that have been found in the focused spot of the electron beam (the first minimum in the current scan) to an inaccurate choice of initial neutral mass distribution or to a poor modeling of thermal conduction at low temperatures.

Then, we studied the effect of diameter variation on the focusing properties of the APLs. We did this by comparing two discharges in capillaries that differ only by the capillary diameters and by the intensity of the imposed current (which was scaled accordingly, in order to provide the same focusing strength in the two discharges). We tracked a realistic high brightness beam trough the two APLs and we compared the emittance growth. We noted that for the case studied, a slight (20%) increase in the capillary radius allows to reduce the emittance growth (approximately, by a factor $1/2$). However, during the tracking we neglected the effect of the wake fields that the electron beam may generate inside the discharges. In order to take it into account accurately, one needs to track the electron beam through the plasma with a PIC code, or at least with a hybrid kinetic-fluid one. Since detailed measurements of the hydrogen distribution prior to discharging are not available, we did not perform such tracking.

Future developments concerning this thesis topic certainly include the simulation of discharges starting from more realistic initial neutral gas density distributions. Furthermore, we consider to study the effect of the amount of gas filling the capillary (related to the backing pressure) at the beginning of the discharge. In addition the use of other gases besides hydrogen is an interesting aspect to explore with simulations (especially, due to the findings of Ref. [82]). Studying a gas different from hydrogen may involve the modification of the model, from a one temperature fluid, to a two temperatures plasma (where local thermodynamic equilibrium is applied separately for electrons and ions, as done by Ref. [19]). This modification is certainly feasible, even though it is not straight forward. Last but not least, the exploration of different capillary geometries, such as tapered profiles, may open new possibilities for the optimization of the discharges for beam focusing purposes. The

same consideration clearly applies also to the shape of the electrodes.

Appendix A

Plasma parameters

When a perturbation is introduced in a globally neutral plasma, electric charges tend to organize themselves in order to collectively screen it. The Debye length λ_{D}, provides the order of magnitude of the screening distance. It can be estimated by studying the equilibrium potential of a point charge, placed in an initially neutral plasma.

The expression for the Debye length in a fully ionized plasma, composed by electrons and ions with charge $z_i e$ is:

$$\lambda_D = \left[\frac{e^2}{\epsilon_0 k_{\mathrm{B}}} \left(\frac{n_e}{T_e} + \frac{z_i^2 n_i}{T_i} \right) \right]^{-\frac{1}{2}}, \tag{A.1}$$

where T_e is the electron temperature, T_i is the ion temperature, n_e is the electron density and n_i is the ion density. In particular, if we only include the contribution of the electrons, the expression becomes:

$$\lambda_D = \sqrt{\frac{\epsilon_0 k_{\mathrm{B}} T_e}{e^2 n_e}}. \tag{A.2}$$

When the electrons of a plasma are displaced by a small distance, they will oscillate around the equilibrium position. These oscillations have a typical frequency, that is called electron plasma frequency:

$$\omega_p = \sqrt{\frac{e^2 n_0}{m_e \epsilon_0}}. \tag{A.3}$$

The plasma skin depth is a parameter that is related to the plasma frequency (also called electron inertial length). It represents the distance to which electromagnetic waves (with frequency lower than the plasma frequency) can penetrate in a plasma, and is defined by:

$$k_p = \frac{\omega_p}{c}. \tag{A.4}$$

Bibliography

[1] ALESINI, D., ET AL. The SPARC/X SASE-FEL Projects. *Laser and Particle Beams*, **22** (2004), 341.

[2] ALEXIADES, V., AMIEZ, G., AND GREMAUD, P.-A. Super-time-stepping acceleration of explicit schemes for parabolic problems. *Communications in numerical methods in engineering*, **12** (1996), 31.

[3] ANANIA, M., ET AL. Plasma production for electron acceleration by resonant plasma wave. *Nuclear Instruments and Methods in Physics Research Section A: Accelerators, Spectrometers, Detectors and Associated Equipment*, **829** (2016), 254. 2nd European Advanced Accelerator Concepts Workshop - EAAC 2015. Available from: `http://www.sciencedirect.com/science/article/pii/S0168900216001911`, `doi:10.1016/j.nima.2016.02.029`.

[4] AUNE, B., ET AL. Superconducting TESLA cavities. *Phys. Rev. ST Accel. Beams*, **3** (2000), 092001. Available from: `https://link.aps.org/doi/10.1103/PhysRevSTAB.3.092001`, `doi:10.1103/PhysRevSTAB.3.092001`.

[5] BAGDASAROV, G., ET AL. Plasma equilibrium inside various cross-section capillary discharges. *Physics of Plasmas*, **24** (2017), 053111. Available from: `https://doi.org/10.1063/1.4984253`, `arXiv:https://doi.org/10.1063/1.4984253`, `doi:10.1063/1.4984253`.

[6] BAGDASAROV, G. A., ET AL. Laser beam coupling with capillary discharge plasma for laser wakefield acceleration applications. *Physics of Plasmas*, **24** (2017), 083109. Available from: `https://doi.org/10.1063/1.4997606`, `arXiv:https://doi.org/10.1063/1.4997606`, `doi:10.1063/1.4997606`.

[7] BAGDASAROV, G. A., ET AL. On production and asymmetric focusing of flat electron beams using rectangular capillary discharge plasmas. *Physics of Plasmas*, **24** (2017), 123120. Available from: `https://doi.org/10.1063/1.5009118`, `arXiv:https://doi.org/10.1063/1.5009118`, `doi:10.1063/1.5009118`.

[8] BECKERS, J. M. Analytical Linear Numerical Stability Conditions for an Anisotropic Three-dimensional Advection-diffusion Equation. *SIAM J. Numer. Anal.*, **29** (1992), 701. Available from: `http://dx.doi.org/10.1137/0729044`, `doi:10.1137/0729044`.

[9] Benedetti, C., Sgattoni, A., Turchetti, G., and Londrillo, P. `ALaDyn`: A High-Accuracy PIC Code for the Maxwell–Vlasov Equations. *IEEE Transactions on Plasma Science*, **36** (2008), 1790. `doi:10.1109/TPS.2008.927143`.

[10] Bethe, H. A. Moliere's theory of multiple scattering. *Physical Review*, **89** (1953), 1256.

[11] Biagioni, A., et al. Temperature analysis in the shock waves regime for gas-filled plasma capillaries in plasma-based accelerators. *Journal of Instrumentation*, **14** (2019), C03002. Available from: `https://doi.org/10.1088%2F1748-0221%2F14%2F03%2Fc03002`, `doi:10.1088/1748-0221/14/03/c03002`.

[12] Birdsall, C. K. and Langdon, A. B. *Plasma physics via computer simulation.* CRC press (2004).

[13] Bisesto, F., et al. Laser–capillary interaction for the exin project. *Nuclear Instruments and Methods in Physics Research Section A: Accelerators, Spectrometers, Detectors and Associated Equipment*, **829** (2016), 309.

[14] Bisesto, F., et al. The FLAME laser at SPARC_LAB. *Nuclear Instruments and Methods in Physics Research Section A: Accelerators, Spectrometers, Detectors and Associated Equipment*, **909** (2018), 452. 3rd European Advanced Accelerator Concepts workshop (EAAC2017). Available from: `http://www.sciencedirect.com/science/article/pii/S0168900218301815`, `doi:10.1016/j.nima.2018.02.027`.

[15] Bittencourt, J. A. *Fundamentals of plasma Physics.* Pergamon (1986).

[16] Blachman, N. M. and Courant, E. D. Scattering of Particles by the Gas in a Synchrotron. *Physical Review*, **74** (1948), 140.

[17] Blumenfeld, I. *Scaling of the longitudinal electric fields and transformer ratio in a non-linear Plasma Wakefield Accelerator.* Ph.D. thesis, Stanford University (2009).

[18] Bobrova, N., Bulanov, S., Esaulov, A., and Sasorov, P. Capillary discharges for guiding of laser pulses. *Plasma Physics Reports*, **26** (2000), 10.

[19] Bobrova, N. A., Esaulov, A. A., Sakai, J.-I., Sasorov, P. V., Spence, D. J., Butler, A., Hooker, S. M., and Bulanov, S. V. Simulations of a hydrogen-filled capillary discharge waveguide. *Physical Review E*, **65** (2001), 016407.

[20] Boggasch, E., Tauschwitz, A., Wahl, H., Dietrich, K.-G., Hoffmann, D. H. H., Laux, W., Stetter, M., and Tkotz, R. Plasma lens fine focusing of heavy-ion beams. *Applied Physics Letters*, **60** (1992), 2475. Available from: `https://doi.org/10.1063/1.107443`, `arXiv:https://doi.org/10.1063/1.107443`, `doi:10.1063/1.107443`.

[21] BOGGASCH, E., ET AL. z-Pinch Plasma Lens Focusing of a Heavy-Ion Beam. *Physical Review Letters*, **66** (1991), 1705.

[22] BRAUN, H. H., DÖBERT, S., WILSON, I., AND WUENSCH, W. Frequency and temperature dependence of electrical breakdown at 21, 30, and 39 GHz. *Physical review letters*, **90** (2003), 224801.

[23] BRENTEGANI, E., ET AL. Numerical studies on capillary discharges as focusing elements for electron beams. *Nuclear Instruments and Methods in Physics Research Section A: Accelerators, Spectrometers, Detectors and Associated Equipment*, (2018).

[24] BROKAW, R. S. Thermal conductivity of gas mixtures in chemical equilibrium. II. *The Journal of Chemical Physics*, **32** (1960), 1005.

[25] BROKS, B., VAN DIJK, J., BASTIAENS, H. M., BOLLER, K. J., AND VAN DER MULLEN, J. Study of a pulsed capillary discharge waveguide with a modulated radius. *Journal of physics D: applied physics*, **39** (2006), 2384.

[26] BROKS, B. H. P., GARLOFF, K., AND VAN DER MULLEN, J. Nonlocal-thermal-equilibrium model of a pulsed capillary discharge waveguide. *Physical Review E*, **71** (2005), 016401.

[27] BRUNO, D., ET AL. Transport properties of high-temperature Jupiter atmosphere components. *Physics of Plasmas*, **17** (2010), 112315.

[28] BUSSMANN, M., ET AL. Radiative Signatures of the Relativistic Kelvin-Helmholtz Instability. In *Proceedings of the International Conference on High Performance Computing, Networking, Storage and Analysis*, SC '13, pp. 5:1–5:12. ACM, New York, NY, USA (2013). ISBN 978-1-4503-2378-9. Available from: `http://doi.acm.org/10.1145/2503210.2504564`, `doi:10.1145/2503210.2504564`.

[29] BUTLER, J. N. AND BROKAW, R. S. Thermal Conductivity of Gas Mixtures in Chemical Equilibrium. *Journal of Chemical Physics*, **26** (1957), 1636.

[30] CAPITELLI, M., BRUNO, D., AND LARICCHIUTA, A. *Fundamental aspects of plasma chemical physics: transport.* Springer Science & Business Media (2013).

[31] CAPITELLI, M., COLONNA, G., AND D'ANGOLA, A. *Fundamental aspects of plasma chemical physics: thermodynamics*, vol. 66. Springer Science & Business Media (2011).

[32] CHEN, P. Grand disruption: A possible final focusing mechanism for linear colliders. *Part. Accel.*, **20** (1986), 171.

[33] CHEN, P., DAWSON, J., HUFF, R. W., AND KATSOULEAS, T. Acceleration of electrons by the interaction of a bunched electron beam with a plasma. *Physical review letters*, **54** (1985), 693.

[34] CHIADRONI, E., ET AL. The SPARC linear accelerator based terahertz source. *Applied Physics Letters*, **102** (2013), 094101.

[35] CHIADRONI, E., ET AL. Beam manipulation for resonant plasma wakefield acceleration. *Nuclear Instruments and Methods in Physics Research Section A: Accelerators, Spectrometers, Detectors and Associated Equipment*, **865** (2017), 139. Physics and Applications of High Brightness Beams 2016. Available from: `http://www.sciencedirect.com/science/article/pii/S0168900217300165`, `doi:10.1016/j.nima.2017.01.017`.

[36] DE MAGISTRIS, M., FORMISANO, A., AND MARTONE, R. Electromechanical modelling of z-pinch plasma lenses with thermal and circuital coupling. *IEEE Transactions on Magnetics*, **34** (1998), 3082. `doi:10.1109/20.717721`.

[37] DE MAGISTRIS, M., MENNA, L. D., MIANO, G., AND SERPICO, C. An analytical approach to optical properties of plasma lenses with a nonlinear magnetic field profile. *Fusion Engineering and Design*, **32** (1996), 377. Available from: `http://www.sciencedirect.com/science/article/pii/S0920379696004929`, `doi:10.1016/S0920-3796(96)00492-9`.

[38] DEROUILLAT, J., ET AL. Smilei : A collaborative, open-source, multi-purpose particle-in-cell code for plasma simulation. *Computer Physics Communications*, **222** (2018), 351. Available from: `http://www.sciencedirect.com/science/article/pii/S0010465517303314`, `doi:10.1016/j.cpc.2017.09.024`.

[39] DEVOTO, R. Transport properties of ionized monatomic gases. *The Physics of Fluids*, **9** (1966), 1230.

[40] DEVOTO, R. Simplified expressions for the transport properties of ionized monatomic gases. *The Physics of Fluids*, **10** (1967), 2105.

[41] DEVOTO, R. Transport coefficients of partially ionized hydrogen. *Journal of Plasma Physics*, **2** (1968), 617.

[42] DOUGLAS, J. AND RACHFORD, H. H. On the numerical solution of heat conduction problems in two and three space variables. *Transactions of the American mathematical Society*, **82** (1956), 421.

[43] EHRLICH, Y., COHEN, C., ZIGLER, A., KRALL, J., SPRANGLE, P., AND ESAREY, E. Guiding of High Intensity Laser Pulses in Straight and Curved Plasma Channel Experiments. *Phys. Rev. Lett.*, **77** (1996), 4186. Available from: `https://link.aps.org/doi/10.1103/PhysRevLett.77.4186`, `doi:10.1103/PhysRevLett.77.4186`.

[44] EINFELDT, B., MUNZ, C.-D., ROE, P. L., AND SJÖGREEN, B. On Godunov-type methods near low densities. *Journal of computational physics*, **92** (1991), 273.

[45] ELLIOTT, J. A. *Plasma kinetic theory, in Plasma Physics, an Introductory Course.* Cambridge Univ. Press (1993).

[46] ESAREY, E., SCHROEDER, C., AND LEEMANS, W. Physics of laser-driven plasma-based electron accelerators. *Reviews of modern physics*, **81** (2009), 1229.

[47] ESAULOV, A., SASOROV, P., SOTO, L., ZAMBRA, M., AND SAKAI, J.-I. MHD simulation of a fast hollow cathode capillary discharge. *Plasma Physics and Controlled Fusion*, **43** (2001), 571. Available from: `http://stacks.iop.org/0741-3335/43/i=4/a=313`.

[48] FANTZ, U. Basics of plasma spectroscopy. *Plasma sources science and technology*, **15** (2006), S137.

[49] FAURE J., GLINEC Y., PUKHOV A., KISELEV S., GORDIENKO S., LEFEBVRE E., ROUSSEAU J.-P., BURGY F., AND MALKA V. A laser–plasma accelerator producing monoenergetic electron beams. *Nature*, **431** (2004), 541. `doi:10.1038/nature02963`.

[50] FERRARIO, M., ET AL. Direct measurement of the double emittance minimum in the beam dynamics of the sparc high-brightness photoinjector. *Physical review letters*, **99** (2007), 234801.

[51] FERRARIO, M., ET AL. Experimental demonstration of emittance compensation with velocity bunching. *Physical review letters*, **104** (2010), 054801.

[52] FERRARIO, M., ET AL. SPARC-LAB present and future. *Nuclear Instruments and Methods in Physics Research, Section B: Beam Interactions with Materials and Atoms*, **309** (2013), 183.

[53] FILIPPI, F. *Plasma source characterization for plasma-based acceleration experiments*. Ph.D. thesis, Universitad́i Roma la Sapienza (2017).

[54] FILIPPI, F., ANANIA, M. P., BIAGIONI, A., CHIADRONI, E., CIANCHI, A., FERBER, Y., FERRARIO, M., AND ZIGLER, A. 3D-printed capillary for hydrogen filled discharge for plasma based experiments in RF-based electron linac accelerator. *Review of Scientific Instruments*, **89** (2018), 083502. Available from: `https://doi.org/10.1063/1.5010264`, `arXiv:https://doi.org/10.1063/1.5010264`, `doi:10.1063/1.5010264`.

[55] FILIPPI, F., ET AL. Gas-filled capillaries for plasma-based accelerators. *Journal of Physics: Conference Series*, **874** (2017), 012036. Available from: `http://stacks.iop.org/1742-6596/874/i=1/a=012036`.

[56] FORSYTH, E. B., LEDERMAN, L. M., AND SUNDERLAND, J. The Brookhaven-Columbia Plasma Lens. *IEEE Transactions on Nuclear Science*, **12** (1965), 872. `doi:10.1109/TNS.1965.4323749`.

[57] FREEMAN, J., BAKER, L., AND COOK, D. Plasma channels for intense-light-ion-beam reactors. *Nuclear Fusion*, **22** (1982), 383.

[58] GEDDES C. G. R., TOTH Cs., J., V. T., ESAREY E., SCHROEDER C. B., BRUHWILER D., NIETER C., CARY J., AND LEEMANS W. P. High-quality

electron beams from a laser wakefield accelerator using plasma-channel guiding. *Nature*, **431** (2004), 538. `doi:10.1038/nature02900`.

[59] GIANNESSI, L., ET AL. Self-amplified spontaneous emission free-electron laser with an energy-chirped electron beam and undulator tapering. *Physical review letters*, **106** (2011), 144801.

[60] GIANNESSI, L., ET AL. High-order-harmonic generation and superradiance in a seeded free-electron laser. *Physical review letters*, **108** (2012), 164801.

[61] GILMORE, R. Saha's Equation and the Partition Function. Available from: `http://www.physics.drexel.edu/~bob/PHYS317_08/saha.pdf`.

[62] GIORGIANNI FLAVIO, ET AL. Strong nonlinear terahertz response induced by Dirac surface states in Bi2Se3 topological insulator. *Nature Communications*, **7** (2016), 11421. Available from: `https://www.nature.com/articles/ncomms11421#supplementary-information`, `doi:10.1038/ncomms11421;;;;;;;;;;;;;;;;;;;;;;;;;;;;;;;;;;;;;;;;;;;;;;;;;;;;;;;;;;;;;;10.1038/ncomms11421`.

[63] GLOWINSKI, R., PAN, T.-W., AND TAI, X.-C. *Some Facts About Operator-Splitting and Alternating Direction Methods*, pp. 19–94. Springer International Publishing, Cham (2016). ISBN 978-3-319-41589-5. Available from: `https://doi.org/10.1007/978-3-319-41589-5_2`, `doi:10.1007/978-3-319-41589-5_2`.

[64] HAHN, H.-S., MASON, E., AND SMITH, F. J. Quantum transport cross sections for ionized gases. *The Physics of Fluids*, **14** (1971), 278.

[65] HIDDING, B., PRETZLER, G., ROSENZWEIG, J., KÖNIGSTEIN, T., SCHILLER, D., AND BRUHWILER, D. Ultracold electron bunch generation via plasma photocathode emission and acceleration in a beam-driven plasma blowout. *Physical review letters*, **108** (2012), 035001.

[66] HIRATA, K. AND YOKOYA, K. Non-gaussian distribution of electron beams due to incoherent stochastic processes. *Particle Accelerators*, **39** (1992), l47.

[67] HIRSCHFELDER, J., CURTISS, C. F., AND BIRD, R. Molecular Theory of Gases and Liquids, New York (1965). *Google Scholar*, (1964).

[68] HOLZER, B. CAS-CERN Accelerator School: Plasma Wake Acceleration. *arXiv preprint arXiv:1708.01118*, (2017).

[69] HUBA, J. Nrl plasma formulary supported by the office of naval research. *Naval Research Laboratory, Washington, DC*, (2016).

[70] HUMPHRIES, S. *Principles of charged particle acceleration*. Courier Corporation (2013).

[71] JANSSEN, J. *Equilibrium and transport in molecular plasmas*. Ph.D. thesis, Eindhoven University of Technology (2016).

[72] JING, C. Dielectric wakefield accelerators. *Reviews of Accelerator Science and Technology*, **9** (2016), 127.

[73] KIRBY, N., BERRY, M., BLUMENFELD, I., HOGAN, M. J., ISCHEBECK, R., AND SIEMANN, R. Emittance growth from Multiple Coulomb Scattering in a plasma wakefield accelerator. In *2007 IEEE Particle Accelerator Conference (PAC)*, pp. 3097–3099 (2007). `doi:10.1109/PAC.2007.4440680`.

[74] KOWALEWICZ, R., ET AL. Performance of the CERN plasma lens in laboratory and beam tests at the antiproton source. In *Conference Record of the 1991 IEEE Particle Accelerator Conference*, pp. 2631–2633 vol.4 (1991). `doi:10.1109/PAC.1991.165053`.

[75] LABAT, M., ET AL. High-gain harmonic-generation free-electron laser seeded by harmonics generated in gas. *Physical review letters*, **107** (2011), 224801.

[76] LE DALLIC, G., LUBRANO DI SCAMPAMORTE, M., KOWALEWICZ, R., MILNER, S., RIEGE, H., CHRISTIANSEN, J., FRANK, K., STETTER, M., AND TKOTZ, R. First test results from the new CERN plasma lens. (1990), 4 p. Available from: `https://cds.cern.ch/record/209758`.

[77] LEEMANS, W. AND ESAREY, E. Laser-driven plasma-wave electron accelerators. *Phys. Today*, **62** (2009), 44.

[78] LEVEQUE, R. J. *Finite volume methods for hyperbolic problems*, vol. 31. Cambridge university press (2002).

[79] LIM, J. K., FRIGOLA, P., TRAVISH, G., ROSENZWEIG, J. B., ANDERSON, S. G., BROWN, W. J., JACOB, J. S., ROBBINS, C. L., AND TREMAINE, A. M. Adjustable, short focal length permanent-magnet quadrupole based electron beam final focus system. *Phys. Rev. ST Accel. Beams*, **8** (2005), 072401. Available from: `https://link.aps.org/doi/10.1103/PhysRevSTAB.8.072401`, `doi:10.1103/PhysRevSTAB.8.072401`.

[80] LINDSTRØM, C. A. Emittance growth and preservation in a plasma-based linear collider. (2019).

[81] LINDSTRØM, C. A. AND ADLI, E. Analytic plasma wakefield limits for active plasma lenses. *arXiv preprint arXiv:1802.02750*, (2018).

[82] LINDSTRØM, C. A., ET AL. Emittance preservation in an aberration-free active plasma lens. *Physical review letters*, **121** (2018), 194801.

[83] LINDSTRØM, C. A., ET AL. Erratum: Emittance Preservation in an Aberration-Free Active Plasma Lens [Phys. Rev. Lett. 121, 194801 (2018)]. *Phys. Rev. Lett.*, **122** (2019), 129901. Available from: `https://link.aps.org/doi/10.1103/PhysRevLett.122.129901`, `doi:10.1103/PhysRevLett.122.129901`.

[84] LU, W., HUANG, C., ZHOU, M., MORI, W., AND KATSOULEAS, T. Nonlinear theory for relativistic plasma wakefields in the blowout regime. *Physical review letters*, **96** (2006), 165002.

[85] Lu, W., Huang, C., Zhou, M., Tzoufras, M., Tsung, F., Mori, W., and Katsouleas, T. A nonlinear theory for multidimensional relativistic plasma wave wakefields. *Physics of Plasmas*, **13** (2006), 056709.

[86] Malka, V., Lifschitz, A., Faure, J., and Glinec, Y. GeV monoenergetic electron beam with laser plasma accelerator. *International Journal of Modern Physics B*, **21** (2007), 277.

[87] Mangles S. P. D., et al. Monoenergetic beams of relativistic electrons from intense laser–plasma interactions. *Nature*, **431** (2004), 535. `doi:10.1038/nature02939`.

[88] Marocchino, A., Massimo, F., Rossi, A., Chiadroni, E., and Ferrario, M. Efficient modeling of plasma wakefield acceleration in quasi-non-linear-regimes with the hybrid code Architect. *Nuclear Instruments and Methods in Physics Research Section A: Accelerators, Spectrometers, Detectors and Associated Equipment*, **829** (2016), 386.

[89] Marocchino, A., Massimo, F., Rossi, A., Chiadroni, E., and Ferrario, M. Efficient modeling of plasma wakefield acceleration in quasi-non-linear-regimes with the hybrid code Architect. *Nuclear Instruments and Methods in Physics Research Section A: Accelerators, Spectrometers, Detectors and Associated Equipment*, **829** (2016), 386.

[90] Marocchino, A., et al. Experimental characterization of the effects induced by passive plasma lens on high brightness electron bunches. *Applied Physics Letters*, **111** (2017), 184101.

[91] Meisel, M. *Emittance Measurement of Electron Beams from Laser Wakefield Acceleration using an Active Plasma Lens*. Masterarbeit, Universität Hamburg, Hamburg (2018). Masterarbeit, Universität Hamburg, 2018. Available from: `https://bib-pubdb1.desy.de/record/414292`, `doi:10.3204/PUBDB-2018-03854`.

[92] Meyer, C. D., Balsara, D. S., and Aslam, T. D. A second-order accurate Super TimeStepping formulation for anisotropic thermal conduction. *Monthly Notices of the Royal Astronomical Society*, **422** (2012), 2102.

[93] Mignone, A., Bodo, G., Massaglia, S., Matsakos, T., Tesileanu, O., Zanni, C., and Ferrari, A. PLUTO: A Numerical Code for Computational Astrophysics. *apjs*, **170** (2007), 228. `arXiv:astro-ph/0701854`, `doi:10.1086/513316`.

[94] Mira, F. *Self Injection of High Brightness electron beams via Wakefield Ionization in beam-driven Plasma Acceleration*. Ph.D. thesis, Universitá di Roma la Sapienza (2017).

[95] Montague, B. W. Emittance growth from multiple scattering in the plasma beat-wave accelerator. Tech. rep., CERN (1984).

[96] MOSTACCI, A., ET AL. Operational experience on the generation and control of high brightness electron bunch trains at SPARC-LAB. In *Advances in X-ray Free-Electron Lasers Instrumentation III*, vol. 9512, p. 95121Q. International Society for Optics and Photonics (2015).

[97] MURAYAMA, M., NEMOTO, M., MASUGATA, K., ITO, M., AND YATSUI, K. Final focusing of proton beam by z-discharged plasma channel. Tech. rep. (1986).

[98] NASSIRI, A., ET AL. History and Technology Developments of Radio Frequency (RF) Systems for Particle Accelerators. *IEEE Transactions on Nuclear Science*, **63** (2016), 707. `doi:10.1109/TNS.2015.2485164`.

[99] NERI, J., BOILER, J., COOPERSTEIN, G., MOSHER, D., AND OTTINGER, P. Transport and focusing of intense ion beams for ICF with z-discharge plasma channels. In *Proc. 7th Int. Conf. High-Power Particle Beams*, pp. 165–170 (1988).

[100] OTTINGER, P., MOSHER, D., AND GOLDSTEIN, S. A. Propagation of intense ion beams in straight and tapered z-discharge plasma channels. *The Physics of Fluids*, **23** (1980), 909.

[101] PANOFSKY, W. K. H. AND BAKER, W. A Focusing Device for the External 350-Mev Proton Beam of the 184-Inch Cyclotron at Berkeley. *Review of Scientific Instruments*, **21** (1950), 445.

[102] PEACEMAN, D. W. AND RACHFORD, J. H. H. The numerical solution of parabolic and elliptic differential equations. *Journal of the Society for industrial and Applied Mathematics*, **3** (1955), 28.

[103] PETRALIA, A., ET AL. Two-color radiation generated in a seeded free-electron laser with two electron beams. *Physical review letters*, **115** (2015), 014801.

[104] POMPILI, R., ET AL. Beam manipulation with velocity bunching for PWFA applications. *Nuclear Instruments and Methods in Physics Research Section A: Accelerators, Spectrometers, Detectors and Associated Equipment*, **829** (2016), 17. 2nd European Advanced Accelerator Concepts Workshop - EAAC 2015. Available from: `http://www.sciencedirect.com/science/article/pii/S0168900216000899`, `doi:10.1016/j.nima.2016.01.061`.

[105] POMPILI, R., ET AL. Femtosecond timing-jitter between photo-cathode laser and ultra-short electron bunches by means of hybrid compression. *New Journal of Physics*, **18** (2016), 083033.

[106] POMPILI, R., ET AL. Experimental characterization of active plasma lensing for electron beams. *Applied Physics Letters*, **110** (2017), 104101.

[107] POMPILI, R., ET AL. Compact and tunable focusing device for plasma wakefield acceleration. *Review of Scientific Instruments*, **89** (2018), 033302. Available from: `https://doi.org/10.1063/1.5006134`, `arXiv:https://doi.org/10.1063/1.5006134`, `doi:10.1063/1.5006134`.

[108] POMPILI, R., ET AL. Focusing of High-Brightness Electron Beams with Active-Plasma Lenses. *Phys. Rev. Lett.*, **121** (2018), 174801. Available from: `https://link.aps.org/doi/10.1103/PhysRevLett.121.174801`, `doi:10.1103/PhysRevLett.121.174801`.

[109] POMPILI, R., ET AL. Recent results at SPARC_LAB. *Nuclear Instruments and Methods in Physics Research Section A: Accelerators, Spectrometers, Detectors and Associated Equipment*, **909** (2018), 139.

[110] PUCELLA, G. AND SEGRE, S. *Fisica dei plasmi*. Zanichelli (2010).

[111] RAIMONDI, P. AND SERYI, A. Novel Final Focus Design for Future Linear Colliders. *Phys. Rev. Lett.*, **86** (2001), 3779. Available from: `https://link.aps.org/doi/10.1103/PhysRevLett.86.3779`, `doi:10.1103/PhysRevLett.86.3779`.

[112] RAUBENHEIMER, T. O. Emittance growth due to beam-gas scattering. Tech. rep., National Lab. for High Energy Physics (1992).

[113] RÖCKEMANN, J.-H., ET AL. Direct measurement of focusing fields in active plasma lenses. *Phys. Rev. Accel. Beams*, **21** (2018), 122801. Available from: `https://link.aps.org/doi/10.1103/PhysRevAccelBeams.21.122801`, `doi:10.1103/PhysRevAccelBeams.21.122801`.

[114] RONSIVALLE, C. AND FRASCATI, E. Simulations of the emittance compensation in photoinjectors and comparison with sparc measurements. *EPAC2008*, (2008).

[115] ROSENZWEIG, J., ET AL. Adiabatic plasma lens experiments at SPARC. *Nuclear Instruments and Methods in Physics Research Section A: Accelerators, Spectrometers, Detectors and Associated Equipment*, **909** (2018), 471. 3rd European Advanced Accelerator Concepts workshop (EAAC2017). Available from: `http://www.sciencedirect.com/science/article/pii/S0168900218301669`, `doi:10.1016/j.nima.2018.02.016`.

[116] ROSSI, A., ET AL. External-injection Experiment at SPARC_LAB. *Physics Procedia*, **52** (2014), 90. Proceedings of the workshop 'Physics and Applications of High Brightness Beams:Towards a Fifth Generation Light Source'. Available from: `http://www.sciencedirect.com/science/article/pii/S187538921400025X`, `doi:10.1016/j.phpro.2014.06.014`.

[117] SHPAKOV, V., ET AL. Longitudinal Phase-Space Manipulation with Beam-Driven Plasma Wakefields. *Phys. Rev. Lett.*, **122** (2019), 114801. Available from: `https://link.aps.org/doi/10.1103/PhysRevLett.122.114801`, `doi:10.1103/PhysRevLett.122.114801`.

[118] SPENCE, D. AND HOOKER, S. M. Investigation of a hydrogen plasma waveguide. *Physical Review E*, **63** (2000), 015401.

[119] SPITZER, L. Physics of fully ionized gases. (1962).

[120] STEINHAUER, L. AND KIMURA, W. Quasistatic capillary discharge plasma model. *Physical Review Special Topics-Accelerators and Beams*, **9** (2006), 081301.

[121] STEINKE, S., ET AL. Multistage coupling of independent laser-plasma accelerators. *Nature*, **530** (2016), 190. Available from: `file:///home/ema/Dottorato/literature/accelerazione_al_plasma/nature16525.html`.

[122] STETTER, M., ET AL. Development of a plasma lens as a fine focusing lens for heavy-ion beams. *Il Nuovo Cimento A (1965-1970)*, **106** (1993), 1725.

[123] STUPAKOV, G. Short-range wakefields generated in the blowout regime of plasma-wakefield acceleration. *Physical Review Accelerators and Beams*, **21** (2018), 041301.

[124] SU, J., KATSOULEAS, T., DAWSON, J., AND FEDELE, R. Plasma lenses for focusing particle beams. *Physical Review A*, **41** (1990), 3321.

[125] TAJIMA, T. AND DAWSON, J. M. Laser electron accelerator. *Physical Review Letters*, **43** (1979), 267.

[126] TERAUCHI, H., BOBROVA, N., SASOROV, P., KIKUCHI, T., SASAKI, T., HIGASHIGUCHI, T., YUGAMI, N., AND KODAMA, R. Observation and numerical analysis of plasma parameters in a capillary discharge-produced plasma channel waveguide. *Journal of Applied Physics*, **109** (2011), 053304.

[127] TORO, E. F. *Riemann solvers and numerical methods for fluid dynamics: a practical introduction.* Springer Science & Business Media (2013).

[128] VACCAREZZA, C., ET AL. The sparc_lab thomson source. *Nuclear Instruments and Methods in Physics Research Section A: Accelerators, Spectrometers, Detectors and Associated Equipment*, **829** (2016), 237.

[129] VAIDYA, B., PRASAD, D., MIGNONE, A., SHARMA, P., AND RICKLER, L. Scalable explicit implementation of anisotropic diffusion with Runge–Kutta–Legendre super-time stepping. *Monthly Notices of the Royal Astronomical Society*, **472** (2017), 3147.

[130] VAN TILBORG, J., ET AL. Active Plasma Lensing for Relativistic Laser-Plasma-Accelerated Electron Beams. *Physical Review Letters*, **115** (2015), 184802. Available from: `http://link.aps.org/doi/10.1103/PhysRevLett.115.184802`, `doi:10.1103/PhysRevLett.115.184802`.

[131] VAN TILBORG, J., ET AL. Nonuniform discharge currents in active plasma lenses. *Physical Review Accelerators and Beams*, **20** (2017), 032803.

[132] WATROUS, J. AND OTTINGER, P. Final focusing of intense ion beams with radially nonuniform current density z discharges. *Physics of Fluids B: Plasma Physics*, **1** (1989), 2470.